UiT The Arctic University of Norway

Faculty of Science and Technology
Department of Physics and Technology

Numerical simulations of coherent blob-like filaments in magnetized plasmas

Daniel Elisabethsønn Antonsen

FYS-3941 Master’s Thesis in Applied Physics and Mathematics SP 30 - December 2024

This thesis document was typeset using the *UiT Thesis LaTeX Template*.

"*I have no special talent. I am only passionately curious.*"

\- Albert Einstein

Abstract

In a world more and more dependent on new and effective energy sources, the introduction of fusion power could prove invaluable. Magnetic confinement of plasma has proved to be difficult, and the curvature of the magnetic field lines in tokamaks give rise to charge polarization at the boundary of the fusion devices leading to cross-field transport. Experiments has shown that the dominating transport is due to 3D filament structures which can be considered as isolated field-aligned 2D blob structures in the plane perpendicular to the magnetic field. The center of mass motion of such blob structures are the main focus of this thesis.

By deriving the reduced two-fluid model while relaxing and retaining the Boussinesq approximation, and by incorporating parallel closure with particle loss and sheath dissipation, a set of invariants has been obtained. Using center of mass diagnostics, we examine the behavior of blobs with varying initial amplitudes and particle loss parameter derived from the parallel closure. Additionally, the impact of the Boussinesq approximation is analyzed both with and without parallel closure.

Utilizing numerical simulations, we verify the scaling found with initial amplitude. Further we obtain results indicating blob stagnation in the limit of larger values of the particle loss parameter, accompanied with behavior equal to the dynamics shown for the sheath dissipation parameter in the case of larger values of the particle loss term. The limitations of the Boussinesq approximation have been verified, and by incorporating the particle loss and the sheath dissipation terms, a transition region has been identified. This region separates the dominance of the Boussinesq approximation in the larger amplitude regime from the scaling behavior determined by sheath dissipation. We also demonstrated an apparent dependence of the initial amplitude on the acceleration of the blobs in the intermediate initial amplitude regime.

Acknowledgements

First and foremost, I would like to thank my supervisor, Professor Odd Erik Garcia. Your boundless pool of ideas and profound knowledge has been an invaluable source of inspiration and guidance through both my project paper and my master thesis.

I would also like to thank my co-supervisors, Synne Brynjulfsen and Olga Paikina, for your invaluable help and guidance with the implementation and use of BOUT++. And with the help and guidance when the eventual problems did arise, leading me to be able to finish this thesis.

To my family and friends, whose support has made this thesis possible. Without you, there might not have been any thesis to hand in. Thank you for the support throughout the last five and a half years.

Contents

Abstract iii

Acknowledgements v

List of Figures ix

1 Introduction 1

2 Background 5
- 2.1 Two-Fluid Model 5
  - 2.1.1 Braginskii Equations 6
  - 2.1.2 Further Simplifications 8
  - 2.1.3 Vorticity Equation 11
  - 2.1.4 Sheath Dissipation 13
  - 2.1.5 Reduced Two-Fluid Model 15
  - 2.1.6 Reduced Two-Fluid Model; Non-Boussinesq 17
- 2.2 Center of mass 17
  - 2.2.1 Position and Velocity 18
  - 2.2.2 Energy Integrals 19

3 Energy Integrals 21
- 3.1 Derivation for Simplified Model 21

4 Numerical Simulations 29
- 4.1 Simulation Setup and Reference Values 29
- 4.2 Energy Integrals 33
  - 4.2.1 Simulations Results 34
  - 4.2.2 Discussion 41
- 4.3 Initial Amplitude Variations 42
  - 4.3.1 Simulations Results 43
  - 4.3.2 Discussion 52
- 4.4 Particle Loss 53
  - 4.4.1 Exponential decay in the background 55
  - 4.4.2 Simulations Results 60

4.4.3 Discussion 71
4.5 Non-Boussinesq 72
4.5.1 Simulation Results 74
4.5.2 Discussion 86

5 Summary and Outlook 89

A Numerical Schemes and Diagnotsical Tools 91
A.1 Finite Difference 91
A.2 Composite Trapezoid 92

Bibliography 95

List of Figures

1.1 Main concept of toroidally shaped magnetic confinement also known as Tokamak (Reprinted from [15]). 2
1.2 Magnetic confinement structure, red corresponds to the core plasma. Yellow region shows the scrape-off layer (SOL) (Reprinted from [8]). 3
1.3 3D blob filaments considered as 2D blobs in the perpendicular plane. (Reprinted from [17]) 3

4.1 Density profile for initial amplitude $\Delta n/N = 1$ showing the Burgers' solution effect on the profile as it evolves. The interaction between the background density and the blob produces sheared flows, which produces formation of the steep leading edge and a trailing wake observed in the figure [5]. . 31
4.2 Density shown as colored contour in all plots. The potential shown as blue curves on the top, and the vorticity as blue curves on the lower row. Dotted lines corresponds to negative values, and lines to positive values. The blob structure is observed to moves radially in the positive x-direction. 35
4.3 Left shows the center of mass radial position of the blob structure observed in figure 4.2. Right shows the computed center of mass radial velocity for the same structure. All axis are dimensionless, but time axis emphasized for readability. 36
4.4 Shows the time derivative of the kinetic energy integrals. The blue line corresponds to the numerical solution and the orange line corresponds to the analytical solution. 37
4.5 Shows the time derivative for the effective gravitational potential energy. Blue line corresponds to numerical solution and the orange line corresponds to the analytical solution. . 38
4.6 Time evolution of the computed energy integrals. 39
4.7 Left shows the time derivative of the kinetic energy integral. Right shows the time derivative of the effective gravitational potential energy integral. 40
4.8 Difference of the time derivatives of the kinetic- and the potential energy integrals. 41

4.9 Contour plots with initial density perturbation $\Delta n/N = 0.01$. The top row shows the density along with the potential, and the density along with the vorticity on the lower row. The blob structures moves radially in the positive x-direction. . . 44
4.10 Contour plots with initial density perturbation $\Delta n/N = 1$. The top row shows the density along with the potential, and the density along with the vorticity on the lower row. The blob structures moves radially in the positive x-direction. 45
4.11 Contour plots with initial density perturbation $\Delta n/N = 10$. The top row shows the density along with the potential, and the density along with the vorticity on the lower row. The blob structures moves radially in the positive x-direction. . . 46
4.12 This figure shows the scaled center of mass radial velocity for different initial perturbed amplitudes. 47
4.13 Shows the maximum radial velocity for each of the different structures with initial perturbed amplitude ranging from 10^{-2} to 10^{2}. The axis are in logarithmic from, and a least square estimate for scaling laws are shown as dotted lines. 48
4.14 Contour plots with initial density perturbation $\Delta n/N = 0.01$. The top row shows the density along with the potential, and the density along with the vorticity on the lower row. The density is shown as colored contours, and the potential and vorticity is shown as blue curves where dotted lines corresponds to negative values and lines correspond to positive values. The blob structures moves radially in the positive x-direction. Blob influenced by sheath dissipation. 49
4.15 Contour plots with initial density perturbation $\Delta n/N = 0.2$. The top row shows the density along with the potential, and the density along with the vorticity on the lower row. The blob structures moves radially in the positive x-direction. Blob influenced by sheath dissipation. 50
4.16 Scaled center of mass velocity for blobs subjected to sheath dissipation 51
4.17 Maximum radial velocity for initial perturbed amplitude ranging from 10^{-2} to 10^{2}. Blob structures subjected to sheath dissipation and the axis are given in logarithmic scale. Dotted lines are the least squares estimate for power scaling laws. . 52
4.18 Contour plots for the density on the left and the potential for the blob structure at right side. In order for the potential to be non-zero, one unit of time has elapsed. Both plots shows a isolated blob structure, and a small electrostatic potential. . 56

4.19 Contour plots for the density on the left and the potential for the blob structure at right side. The density and potential are shown for 200 elapsed time steps. The non-physicality are shown in both plots, and a wave-like behavior emerges in both the density and the potential. 57

4.20 Radial COM diagnostics for $\sigma_n = 0.01, 0.02, 0.05$ showing the nonphysical effects for the larger σ_n values. Initial amplitude is $\Delta n/N = 0.1$. 59

4.21 Maximum radial COM velocity as a function of σ_n for $\Delta n/N = 0.1$. Shows the nonphysical behavior for larger σ_n values. . . 59

4.22 Shows the center of mass radial diagnostics for blobs with $\Delta n/N = 0.1$ with varying σ_n parameter from 10^{-4} to 0.01. Position is shown to the left and velocity is shown on the right. 61

4.23 Shows the center of mass radial diagnostics for blobs with $\Delta n/N = 1$ with varying σ_n parameter from 10^{-4} to 0.01. Position is shown to the left and velocity is shown on the right. 61

4.24 Shows the center of mass radial diagnostics for blobs with $\Delta n/N = 2$ with varying σ_n parameter from 10^{-4} to 0.01. Position is shown to the left and velocity is shown on the right. 62

4.25 Shows the center of mass radial diagnostics for blobs with $\Delta n/N = 0.1$ with varying σ_n parameter from 0.01 to 0.05. Position is shown to the left and velocity is shown on the right. 63

4.26 Shows the center of mass radial diagnostics for blobs with $\Delta n/N = 1$ with varying σ_n parameter from 0.01 to 0.05. Position is shown to the left and velocity is shown on the right. . 63

4.27 Shows the center of mass radial diagnostics for blobs with $\Delta n/N = 2$ with varying σ_n parameter from 0.01 to 0.05. Position is shown to the left and velocity is shown on the right. . 64

4.28 Maximum center of mass radial velocity are shown as a function of σ_n for blobs with $\Delta n/N = 0.1$. The σ_n-axis are shown in logarithmic scale and the maximum V_x-axis are shown in linear scale. 65

4.29 Shows a maximum radial COM velocity as a function of the particle loss parameter σ_n for blobs with $\Delta n/N = 1$ shown as red crosses and $\Delta n/N = 2$ shown as black dots. σ_n-axis are shown in logarithmic scale and the maximum radial COM velocity are shown in linear scale. 66

4.30 Shows a maximum radial COM velocity as a function of the particle loss parameter σ_n for blobs with $\Delta n/N = 1$ shown as red crosses and $\Delta n/N = 2$ shown as black dots. Both axis are shown in logarithmic scale. 67

4.31 Maximum instantaneous density amplitude as a function of radial COM velocity for several σ_n-values. Both axis are shown in logarithmic scale. Initial density of blobs $\Delta n/N = 0.1$. . . 68

4.32 Maximum instantaneous density amplitude as a function of radial COM velocity for several σ_n-values. Both axis are shown in logarithmic scale. Initial density of blobs $\Delta n/N = 1$. . . . 68
4.33 Maximum instantaneous density amplitude as a function of radial COM velocity for several σ_n-values. Both axis are shown in logarithmic scale. Initial density of blobs $\Delta n/N = 2$. . . . 69
4.34 Contour plot showing the density, potential and vorticity curves for $\Delta n/N = 1$ blob structure with $\sigma_n = 1 \times 10^{-4}$. The blob are shown for three different time steps. 70
4.35 Contour plot showing the density, potential and vorticity curves for $\Delta n/N = 0.1$ blob structure with $\sigma_n = 0.05$. The blob are shown for three different time steps 71
4.36 Center of mass radial diagnostics comparing blob subjected to Boussinesq approximation and not subjected to Boussinesq approximation for initial amplitude $\Delta n/N = 0.1$. The blue full line corresponds to Boussinesq simulation and orange dotted line corresponds to non-Boussinesq simulation. Position is shown on the right and velocity are shown on the left. . . 74
4.37 Center of mass radial diagnostics comparing blob subjected to Boussinesq approximation and not subjected to Boussinesq approximation for initial amplitude $\Delta n/N = 0.5$. The blue full line corresponds to Boussinesq simulation and orange dotted line corresponds to non-Boussinesq simulation. Position is shown on the right and velocity are shown on the left. . . 74
4.38 Center of mass radial diagnostics comparing blob subjected to Boussinesq approximation and not subjected to Boussinesq approximation for initial amplitude $\Delta n/N = 2$. The blue full line corresponds to Boussinesq simulation and orange dotted line corresponds to non-Boussinesq simulation. Position is shown on the right and velocity are shown on the left. . . 75
4.39 Center of mass radial diagnostics comparing blob subjected to Boussinesq approximation and not subjected to Boussinesq approximation for initial amplitude $\Delta n/N = 5$. The blue full line corresponds to Boussinesq simulation and orange dotted line corresponds to non-Boussinesq simulation. Position is shown on the right and velocity are shown on the left. . . 75
4.40 Center of mass radial diagnostics comparing blob subjected to Boussinesq approximation and not subjected to Boussinesq approximation for initial amplitude $\Delta n/N = 10$. The blue full line corresponds to Boussinesq simulation and orange dotted line corresponds to non-Boussinesq simulation. Position is shown on the right and velocity are shown on the left. . . 76

4.41 The root-mean-squared error computed between the radial COM velocity curves for each initial perturbed amplitude $\Delta n/N$ from 0.1 to 10. Figure are given in logarithmical scale for the initial amplitude and linear scale for the error. 77
4.42 Maximum radial COM velocity as a function of initial amplitude for Boussinesq and non-Boussinesq simulations. The black dots shows the Boussinesq approximation and the red crosses shows the non-Boussinesq. The blue dotted line shows a least squares estiamte for a scaling law using non-Boussinesq points. 78
4.43 Maximum radial COM velocity as a function of initial amplitude for non-Boussinesq simulations with and without the effect of sheath dissipation. Black dots corresponds to simulations where sheath dissipation and particle loss has been neglected, and red crosses corresponds top simulations where sheath dissipation are retained. 79
4.44 Maximum instantaneous amplitude as a function of radial COM velocity, with initial perturbed amplitude $\Delta n/N = 0.1$. Blue line corresponds to Boussinesq approximation, orange and green dotted lines corresponds to non-Boussinesq with and without sheath dissipation terms respectively. 81
4.45 Maximum instantaneous amplitude as a function of radial COM velocity, with initial perturbed amplitude $\Delta n/N = 1$. Blue line corresponds to Boussinesq approximation, orange and green dotted lines corresponds to non-Boussinesq with and without sheath dissipation and particle loss terms respectively. 82
4.46 Maximum instantaneous amplitude as a function of radial COM velocity, with initial perturbed amplitude $\Delta n/N = 10$. Blue line corresponds to Boussinesq approximation, orange and green dotted lines corresponds to non-Boussinesq with and without sheath dissipation and particle loss terms respectively. 83
4.47 Shows the density, potential and vorticity curves for initial perturbed amplitude $\Delta n/N = 5$. Simulation made using non-Boussinesq model neglected sheath dissipation and particle loss, shown for three distinct time steps. 84
4.48 Shows the density, potential and vorticity curves for initial perturbed amplitude $\Delta n/N = 10$. Simulation made using non-Boussinesq model neglected sheath dissipation and particle loss, shown for three distinct time steps. 85

/1

Introduction

In the search for more sustainable and clean energy sources, nuclear fusion has emerged as a promising technology which is capable of handling the world's ever growing energy demands. In spite of popular opinions in media, the concept of nuclear energy production is not all the same. Fusion, which is the process that powers stars, involves the fusing of lighter atomic nuclei such as hydrogen or nitrogen, etc. into heavier atomic nuclei and in the process releasing enormous amounts of energy [10]. The fusion process occurs at very high temperatures, making it difficult to contain. In stars such as the sun, the fusion process occurs at the core which has a temperature of about 15×10^6 K. At these temperatures, the atomic nuclei becomes fully ionized and the gas becomes a plasma. Stars sustain fusion processes due to the immense gravitational forces generated by their vast mass. Unfortunately this method of confinement is not practical for containing fusion reactions in reactors on Earth. Of the many fusion processes, the most used is the process that combines the two hydrogen isotopes; Deuterium ${}_1^2D$ and Tritium ${}_1^3T$ and can be described by [1, 7]

$$ {}_1^2\mathrm{D} +_1^3 \mathrm{T} \longrightarrow_2^4 \mathrm{He} +_0^1 \mathrm{n}\ (14.1\mathrm{MeV}) \tag{1.1}$$

where Deuterium and Tritium fuses into helium and neutron carrying large amount of energy. Obtaining Deuterium and Tritium has proved to not be difficult, and Deuterium can be extracted from seawater. Tritium is slightly radioactive with a half-life of roughly 12 years, and must be artificially made. This can be achieved by bombarding the Lithium isotope ^{6}L with neutrons. Confinement of such a fusion reaction has proved difficult, due to the extremely

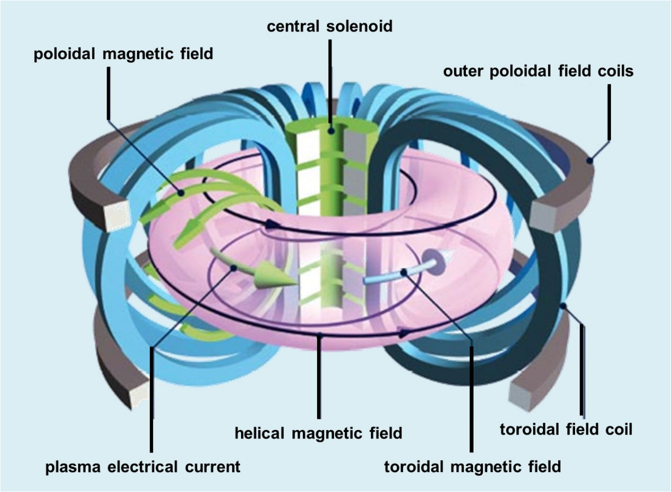

Figure 1.1: Main concept of toroidally shaped magnetic confinement also known as Tokamak (Reprinted from [15]).

high temperature requirement of 150×10^6 K to achieve Deuterium - Tritium fusion reaction. Thus making mechanical confinement practically impossible [10]. The high temperature plasma would almost instantaneous react with- and cause erosion of the walls, leading to production of impurities which would effect the fusion reaction and damaged [10].

Due to the large temperature leading to ionization of the atomic nuclei, a method of confinement proven to be sustainable is magnetic confinement. This method consists of utilizing the gyration motion of charged particles in magnetic fields [7]. By wrapping coils of electrically conducting wire around the cylinder, this creates a uniform magnetic field within the cylinder. This will confine the particles inside the cylinder, however the induced magnetic field lines would intersect vessel walls at both ends of the vessel. This effect can be mitigated by connecting the cylinder at the ends, creating a torus or ”donut” shape [7, 10]. Due to the curvature of magnetic field lines, the particles experiences induced drifts. These are the guiding center drifts, and cause negatively and positively charged particles to drift in opposite directions [7, 10, 11]. The resulting charge separation, leads to a combined drifts of the particles radially outwards [12]. This effect can be seen in figure 1.3, showing the effects of the charge separation leading to filaments transport as well as for the core plasma. In order to remove this radially outwards drift, we introduce a current moving through the cylindrical plasma which induces a current creating a poloidal magnetic field. The combination of the uniform magnetic field through the plasma column and the induced poloidal magnetic field leads to confinement through a combined helical magnetic field [7, 10]. The resulting device is the tokamak, shown in figure 1.1.

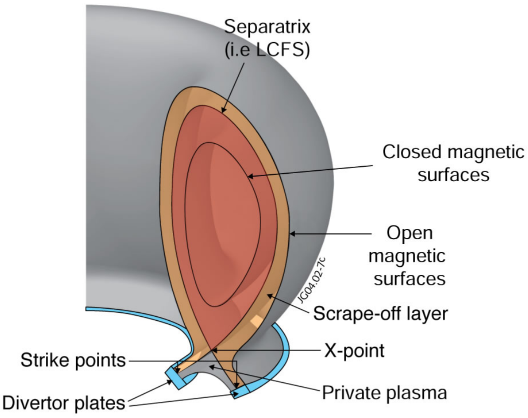

Figure 1.2: Magnetic confinement structure, red corresponds to the core plasma. Yellow region shows the scrape-off layer (SOL) (Reprinted from [8]).

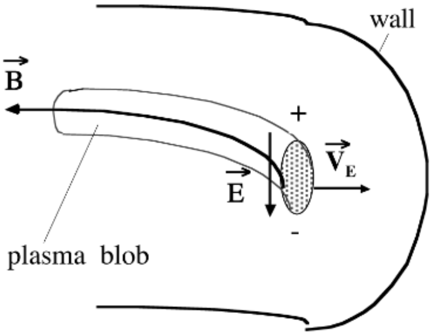

Figure 1.3: 3D blob filaments considered as 2D blobs in the perpendicular plane. (Reprinted from [17])

However, this magnetic confinement structure does not completely mitigate the plasma transport to the vessel walls. Experiments show a radial transport of excess plasma particles and heat through the region known as the scrape-off layer, out to the walls [2–7, 10–14, 17–27]. The scrape-off layer (SOL) is the region after the last closed flux surface (LCFS) in a tokamak, just outside the core plasma. Here the magnetic field lines does not close in on them self as is the case in the core, they instead intersect material surfaces which is called deviator plates [7, 16]. These plates are specifically made to withstand the excess plasma, and the structure is shown in figure 1.2. The transport through the SOL has been observed to be dominated by field aligned 3D plasma filaments, which can be considered 2D blobs in the plane perpendicular to the magnetic field lines [2–7, 11–14, 17–23, 25–27]. Figure 1.3 show these 3D filaments, and the resulting electric drifts due to the polarization caused by the magnetic field curvature [2–4, 6, 11, 12, 14].

These filament structures or blob structures are the main focus of this thesis. Through numerical simulations made using a set of derived model equations, we will consider the center of mass motion of the blob structures in the perpendicular plane to the magnetic field. We will restrict our analysis to field-align filaments, which allows us to use the concept of sheath dissipation as parallel closure [24]. Previous publications consider the effects of blob characteristic cross-field size, and how it effects the maximum radial velocity [2, 12, 19]. Through an order of magnitude approach, different sizes has been shown to impact the radial center of mass velocity of the blob structures [2, 5, 6, 11, 12, 18, 20]. This includes the initial perturbed amplitude of the density of blob structures, where the density are considered a Gaussian distribution.

In this thesis, we will consider the case of isolated blob structures initialized as Gaussian density perturbation above a constant background density. We consider single ion species, reducing the complexity of the derived model equations. In the parallel closure, we introduce two parameters; the particle loss parameter and the sheath dissipation parameter. The latter has been considered in previous works such as in ref. [19]. We will derive the reduced two-fluid model and invariants based on a simplified model containing parallel closure. We will study the center of mass diagnostics and the dependence of the initial amplitude along with the dependence on the particle loss parameter. We will relax the Oberbeck-Boussinesq approximation usually introduced in the model equations to reduce complexity. And consider the combined effect of the Oberbeck-Boussinesq approximation and the parallel closure terms in the model equations.

The rest of the thesis is structure as follows. In chapter 2 we will derive the model equations retaining and relaxing the Oberbeck-Boussinesq approximation, obtaining a set of model equations which will form the basis for the studies done in the thesis. We will further introduce the definitions of the center of mass diagnostics for isolated blob structures in order to quantify the behavior of the blobs. In chapter 3 we will derive a set of invariants based on a simplification of the reduced two-fluid model relaxing the Oberbeck-Boussinesq approximation. chapter 4 will present and discuss the results obtained through numerical simulations using various versions of the model equations describing the blob motion in the SOL. Chapter 5 will contain a summary of the results and discussion from the simulations, and possible ares of focus for further studies.

2

Background

In order to simulate isolated filaments as blob structures in the two-dimensional plane perpendicular to the magnetic field lines, a set of model equations must be derived. In this chapter, we will derive the reduced two-fluid model starting from the Braginskii equations for a particle species s. We will consider both the reduced two-fluid model retaining the Oberbeck-Boussinesq approximation or more commonly denoted Boussinesq approximation or thin-layer approximation for which we assume a small density gradient. In order for achive parallel closure we introduce sheath dissipation and particle loss terms, the latter is of great importance in the simulations discussed in chapter 4. For isolated blob structures, the center of mass velocity is proportional to the total radial convective flux making the center of mass diagnostics a highly relevant quantities to consider [12]. Thus the main characteristics considered in this thesis, are the center of mass diagnostics for isolated blobs. In this chapter, the center of mass position and velocity will be introduced and defined along with the kinetic and potential energy integrals.

2.1 Two-Fluid Model

The behavior of blob structures in the scrape-off-layer of tokamks, can be described using various models. One such model can be obtained from the two lowest velocity moments of the kinetic Boltzmann equation, which can be systematically simplified to reveal the two-fluid model [1, 7].

This section contains a brief derivation of the two-fluid model. And by further simplifications, the reduced two-fluid model where the Bohm normalization is utilized. Starting from the lowest order velocity moments, also known as the Braginskii fluid equations [1, 7], we can introduce the concept of *drift approximation* to simplify the momentum equations for each particle species in order to reveal algebraic expression for the drifts that determines the particles movement [1]. The motion parallel to the magnetic field lines, will be simplified using *sheath dissipation* [24]. Lastly, the model equations will be simplified using the Bohm normalization to yield the reduced two-fluid model; which contains the particle continuity equation and the vorticity equation.

2.1.1 Braginskii Equations

The two lowest order velocity moments of the kinetic Boltzmann equation for particle species s with collisional closure, are given by the continuity equation and the momentum equation. These can for any particle species s be expressed by

$$\frac{\partial n_s}{\partial t} + \nabla \cdot (n_s \mathbf{u}_s) = 0 \tag{2.1}$$

$$m_s n_s \left(\frac{\partial}{\partial t} + \mathbf{u}_s \cdot \nabla \right) \mathbf{u}_s = -\nabla p_s + q_s n_s \left(\mathbf{E} + \mathbf{u}_s \times \mathbf{B} \right) - m_s n_s \nu_{ss'} (\mathbf{u}_s - \mathbf{u}_{s'}) \tag{2.2}$$

where n_s is the particle density, m_s is the particle mass and q_s is the charge.

In order to reduce these equations, we can use the concept of *drift approximation*. This consists of reducing the momentum equation into an algebraic expression for the drifts that governs the particle motion [1, 7]. Through the introduction of a unit vector in the direction of the magnetic field $\mathbf{B}$, which is defined by

$$\mathbf{b} = \frac{\mathbf{B}}{B}$$

we can decompose the motion of the particles into drifts perpendicular to the magnetic field, so-called cross-field drifts, and motion parallel to the magnetic field.

We can first consider the cross-field drifts by taking the cross-product of the momentum equation, defined in equation 2.2, with the unit vector in the magnetic field direction. Using the assumption of electrostatic field with potential ϕ, so the electric field can be written as $\mathbf{E} = -\nabla\phi$, we obtain an expression for the cross-field drifts by

$$\mathbf{u}_{\perp s} = \frac{1}{B}\mathbf{b} \times \nabla\phi + \frac{1}{n_s q_s B}\mathbf{b} \times \nabla p_s + \frac{m_s}{q_s B}\mathbf{b} \times \left(\frac{\partial}{\partial t} + \mathbf{u}_s \cdot \nabla \right) \mathbf{u}_s - \frac{m_s \nu_{ss'}}{q_s B}\mathbf{b} \times (\mathbf{u}_s - \mathbf{u}_{s'})$$

where the property $\mathbf{u}_{\perp} = \mathbf{b} \times (\mathbf{u}_s \times \mathbf{b}) = \mathbf{u}_s - \mathbf{u}_{||}$ has been utilized to indicate a vector perpendicular to the magnetic field. However, this expression contains the entire velocity of particle species s on both sides making it an implicit expression for the perpendicular velocity. In order to make this expression explicit, we can apply the concept of drift ordering. We introducing a scale defined as $\delta \equiv \rho_s/L$ where ρ_s is the Larmor radius defined as mc_s/eB and L a typical length scale of the plasma parameters [7, 16]. Further we introduce the normalized parameters by $n' = n/N$, $\mathbf{u}' = \mathbf{u}/U$, $p' = p/mNc_s^2$, $\mathbf{x}' = \mathbf{x}/L$ and $t' = tL/U$. Here c_s is the acoustic velocity defined as $c_s = \sqrt{T_s/m_s}$, N background density, U the typical fluid velocity of the specific system. Inserting this normalization into equation 2.2, we obtain

$$n_s' \left(\frac{\partial}{\partial t'} + \mathbf{u}_s' \cdot \nabla' \right) \mathbf{u}_s' = -\frac{c_s^2}{U^2} \nabla' p' + n' \frac{L}{\rho_s} \frac{c_s}{U} \left(\frac{\mathbf{E}}{UB} + \mathbf{u}_s' \times \mathbf{b} \right) \tag{2.3}$$

where the normalized parameters have been introduced and the collisional term has been removed and will be reintroduced [16]. We now make the assumption that the fluid velocity is much smaller than the acoustic velocity and that $\rho_s \ll L$ [7, 16]. So

$$\frac{U}{c_s} \sim \frac{\rho_s}{L} \ll 1 \tag{2.4}$$

which can be further imposed on the momentum equation. Thus we observe that the most dominant terms, and are the lowest order terms, are given by

$$0 = -\nabla p_s + q_s n_s (\mathbf{E} + \mathbf{u}_s \times \mathbf{B}) \tag{2.5}$$

leaving the electric drift and the diamagnetic drifts to the lowest order. Inserting this into the right hand side of the implicit equations and denoting the drifts respectively by

$$\begin{aligned}
\mathbf{u}_E &= \frac{1}{B} \mathbf{b} \times \nabla \phi \\
\mathbf{u}_{ds} &= \frac{1}{n_s q_s B} \mathbf{b} \times \nabla p_s \\
\mathbf{u}_{ps} &= \frac{m_s}{q_s B} \mathbf{b} \times \left(\frac{\partial}{\partial t} + (\mathbf{u}_E + \mathbf{u}_{ds}) \cdot \nabla \right) (\mathbf{u}_E + \mathbf{u}_{ps}) \\
\mathbf{u}_{\nu s} &= -\frac{m_s \nu_{ss'}}{q_s B} \mathbf{b} \times ((\mathbf{u}_E + \mathbf{u}_{ds}) - (\mathbf{u}_E + \mathbf{u}_{ds'})) = -\frac{m_s \nu_{ss'}}{q_s B} \mathbf{b} \times (\mathbf{u}_{ds} - \mathbf{u}_{ds'})
\end{aligned}$$

where $\mathbf{u}_E$ is the electric drift or $\mathbf{E} \times \mathbf{B}$-drift, $\mathbf{u}_{ds}$ is the diamagnetic drift, $\mathbf{u}_{ps}$ is the polarization drift and $\mathbf{u}_{\nu s}$ is the frictional drift.

And so the cross-field drift can be written as

$$\mathbf{u}_{\perp s} = \mathbf{u}_E + \mathbf{u}_{ds} + \mathbf{u}_{ps} + \mathbf{u}_{\nu s}$$

Using this expression for the cross-field drift, we can express the total drift of particle species s as

$$\mathbf{u}_s = \mathbf{u}_E + \mathbf{u}_{ds} + \mathbf{u}_{ps} + \mathbf{u}_{vs} + \mathbf{u}_{\|s} \tag{2.6}$$

where the last term corresponds to the drift parallel to the magnetic field lines. We will not simplify this term as of now, but rather consider it later in the derivation when we introduce the concept of *sheath dissipation*.

Since we now have an expression for the total drifts, this can be further inserted into the continuity equation, which is defined in equation 2.1. By the linearity of the divergence operator, we obtain the expression

$$\frac{\partial n_s}{\partial t} + \nabla \cdot (n_s \mathbf{u}_E) + \nabla \cdot (n_s \mathbf{u}_{ds}) + \nabla \cdot (n_s \mathbf{u}_{ps}) + \nabla \cdot (n_s \mathbf{u}_{vs}) + \nabla \cdot (n_s \mathbf{u}_{\|s}) = 0 \tag{2.7}$$

Now we can make further simplification by considering each term individually. But before we continues with the simplifications of the equations, it can be useful to clarify the coordinate system we consider.

2.1.2 Further Simplifications

In the derivation of the two-fluid model, we will consider two coordinate systems; first a cylindrical coordinate system due to toroidally shaped plasma, and lastly a local Cartesian coordinate system when considering the scrape-off layer (SOL).

The cylindrical coordinate system is defined by (R, Θ, Z), where R-direction is radially outwards from the center of the reactor, Θ-direction is in the opposite direction of the magnetic field lines through the plasma and Z-direction is vertically upward. The local Cartesian coordinate system will be introduced when we change coordinate system later in the derivation [1].

The simplest expression for the magnetic field $\mathbf{B}$, is given by

$$\mathbf{B}_{\text{tor}} = \frac{B_0 R_0}{R} \mathbf{b} \tag{2.8}$$

where R_0 is the major radius of the device, and B_0 is the magnetic field strength at this radius. In the cylindrical coordinate system, the expression for the magnetic field takes the form

$$\mathbf{B}_{\text{tor}} = -\frac{B_0 R_0}{R} \hat{\Theta} \tag{2.9}$$

since $\hat{\Theta} = -\mathbf{b}$.

Now that the coordinate system is introduced, we can proceed with the simplifications of the terms in the continuity equation. Using simple vector relation, the first term in equation 2.7 can be expressed as

$$\nabla \cdot (n_s \mathbf{u}_E) = \mathbf{u}_E \cdot \nabla n_s + n_s \nabla \cdot \mathbf{u}_E$$

So we need the divergence of the electric drift, i.e. $\nabla \cdot \mathbf{u}_E$, to be able to simplify the expression more. By using vector relations for the gradient, divergence and curl operator along with the dot product and cross-product in cylindrical coordinates, we can simplify the divergence of the electric drift by

$$\nabla \cdot \mathbf{u}_E = \nabla \left(\frac{1}{B} \right) \cdot \mathbf{b} \times \nabla \phi + \frac{1}{B} \nabla \times \mathbf{b} \cdot \nabla \phi = -\frac{2}{BR} \frac{\partial \phi}{\partial Z} \tag{2.10}$$

where the relations

$$\nabla \left(\frac{1}{B} \right) = \frac{1}{BR} \hat{R}$$
$$\nabla \times \mathbf{b} = -\frac{1}{R} \hat{Z}$$

have been used. It can now be useful to introduce a local Cartesian coordinate system, or a slab approximation. Under the assumption that we consider a small region in the outboard mid-plane, we can use a linearization of the toroidal angle. Then we introduce the approximations $\hat{R} \approx \hat{x}$, $\hat{\Theta} \approx \hat{z}$ and the binormal direction becomes $\hat{Z} = \hat{y}$ [1, 7]. Further under the assumption that the ratio of the minor radius a_0 and the major radius R_0 is very small, i.e. $a_0/R_0 \ll 1$, then we can apply the approximation $1/B \approx 1/B_0$ [1, 20]. And utilizing that for a toroidal magnetic field $BR = B_0 R_0$, the divergence of the electric drift can be expressed by

$$\nabla \cdot \mathbf{u}_E = -\frac{2}{B_0 R_0} \frac{\partial \phi}{\partial y} \tag{2.11}$$

Further considering the second term in equation 2.7, we can rewrite this as

$$n_s \nabla \cdot \mathbf{u}_{ds} + \mathbf{u}_{ds} \cdot \nabla n_s \tag{2.12}$$

Firstly the second term, which contains the dot-product of the diamagnetic drift and the gradient of the density for particle species s, can be simplified under the assumption of isothermal plasma. That is, we have $p_s = T_s n_s$, and combining this with vector relations in cylindrical coordinates, we are left with

$$\mathbf{u}_{ds} \cdot \nabla n_s = 0$$

This results tell us that the diamagnetic drift does not contribute to the advection of the plasma density, which is sometimes called *diamagnetic cancellation* [1, 14].

To simplify equation 2.12 further, we must find an expression for the divergence of the diamagnetic drift. Using simple vector relations, we can express the divergence as

$$\nabla \cdot \mathbf{u}_{ds} = \frac{T_s}{q_s n_s}\left(\nabla\left(\frac{1}{B}\right) \cdot \mathbf{b} \times \nabla n_s + \frac{1}{B}\nabla \times \mathbf{b} \cdot \nabla n_s\right) = -\frac{2T_e}{q_e n_e B_0 R_0}\frac{\partial n}{\partial y} \tag{2.13}$$

where we have recognized the term in the middle part of the equation above, as the same found in equation 2.10. And since we also want the electron continuity equation, then we will for the remainder of the derivation of the first equation given in this thesis, use electrons as particle species. Further, we will also introduced the assumption of quasi-neutrality, which implies $n_e \approx n_i = n$ for singly charged ions.

In order to simplify the electron continuity equation further, we can continue considering the polarization term. To derive an expression for the divergence of the polarization drift, we consider the mass ratio of the electrons and the ions, which gives $m_e/m_i << 1$. This indicates that the electron mass is significantly smaller than the ion mass. Consequently, the contribution of electron inertia is negligible and can be disregarded in the further derivation of the model equations and we simply set $\mathbf{u}_{pe} \approx 0$, which leads to zero contribution from the divergence term [1].

At this point, we adopt the common assumption of cold ions ($T_i \approx 0$), which is frequently employed in established literature. Although experimental data often suggest that the ion temperature exceed electron temperature, i.e. $T_i > T_e$, this simplification is added for mathematical convenience. The cold ion approximation successfully represent the core dynamics of the system, allowing for a reduction of the complexity of the the model equations [1, 7]. The frictional drift can be simplified due the cold ion approximation, thus the using the lowest order drifts we obtain that the frictional drift for an isothermal, quasi-neutral plasma can be given by [1, 7]

$$\mathbf{u}_{\nu e} = -D_n \nabla_\perp n$$

where $D_n = \frac{m_e \nu_{ei} T_e}{e^2 B_0^2}$ is the cross-field diffusion coefficient [16]. ν_{ei} is the collisional frequency for electron-ion collisions [16]. Thus the divergence of the collisional friction drift for the electrons, can be written as [7]

$$\nabla \cdot (n\mathbf{u}_{\nu e}) \approx -\nabla \cdot (D_n \nabla_\perp n) \approx -D_n \nabla_\perp^2 n \tag{2.14}$$

Combining the terms for the divergence, the electron continuity equation under the assumption made, can be expressed by [1]

$$\frac{\partial n}{\partial t} + \mathbf{u}_E \cdot \nabla n - \frac{2n}{B_0 R_0}\frac{\partial \phi}{\partial y} + \frac{2T_e}{eB_0 R_0}\frac{\partial n}{\partial y} = D_n \nabla_\perp^2 n - \nabla \cdot (n\mathbf{u}_{e\parallel}) \tag{2.15}$$

This makes up the first of the two equations contained in the two-fluid model.

2.1.3 Vorticity Equation

The second equation of the two-fluid model can be derived by subtracting the electron- and ion continuity equations. For ions, we follow a similar procedure as is applied to the electrons, and utilizing the drift approximations approach to analyze the ion drifts [1].

After applying the procedure, we are left with the following drifts for the ion movement

$$\mathbf{u}_i = \mathbf{u}_E + \mathbf{u}_{pi} + \mathbf{u}_{\nu i} + \mathbf{u}_{i,\ vis} + \mathbf{u}_{i\|} \tag{2.16}$$

Due to the already established approximation of cold ions, the diamagnetic drift for the ions are neglected. And an additional drift due to ion-ion collisions are added, which for the case of electron-electron collisions was neglected due to the low electron mass compared to the ion mass [1]. This is added as a viscosity drift.

Further inserting the drifts in equation 2.16, into the continuity equation gives

$$\frac{\partial n}{\partial t} + \nabla \cdot (n\mathbf{u}_E) + \nabla \cdot (n\mathbf{u}_{pi}) + \nabla \cdot (n\mathbf{u}_{\nu i}) + \nabla \cdot (n\mathbf{u}_{i,\ vis}) + \nabla \cdot (n\mathbf{u}_{i\|}) = 0 \tag{2.17}$$

Utilizing the same approach in simplifying the ions continuity equation as was done for the electron continuity equation, each term can be isolated and simplified.

The second term in equation 2.17 is the electric drift, which are the same independent of particle species. And so it is the same for electrons and ions, which implies that the divergence takes the same form for the ions as it did for the electrons. From earlier in the derivation, we have

$$\nabla \cdot (n\mathbf{u}_E) = \mathbf{u}_E \cdot \nabla n - \frac{2n}{B_0 R_0}\frac{\partial \phi}{\partial y} \tag{2.18}$$

The third term represent the polarization drift, which, to the lowest order for ions neglecting the diamagnetic drift, can be expressed as

$$\mathbf{u}_{pi} = \frac{m_i}{eB}\mathbf{b} \times \left(\frac{\partial}{\partial t} + \mathbf{u}_E \cdot \nabla\right)\mathbf{u}_E \tag{2.19}$$

Inserting this into the divergence and neglecting the non-uniformity of the magnetic field. So we obtain no contributions from the gradient of the magnetic field and the curl of the unit vector in the magnetic field, and thus we get the approximation

$$\nabla \cdot (n\mathbf{u}_{pi}) \approx \frac{m_i}{eB_0^2}\nabla \cdot \left(n\frac{d\nabla_\perp \phi}{dt}\right) \tag{2.20}$$

where the expression

$$\frac{d}{dt} = \frac{\partial}{\partial t} + \mathbf{u}_E \cdot \nabla$$

are introduced, which can be recognized as the well-known material derivative. The divergence of the polarization drift can be approximated further by implementing the *Boussinesq approximation*, also known as the thin-layer approximation. Imposing this leads to neglection of the gradient of the particle density in the compression of the polarization drift flux term, and consequently [1]

$$\nabla \cdot \left(n \frac{d\nabla_\perp \phi}{dt} \right) = \nabla n \cdot \frac{d\nabla_\perp \phi}{dt} + n\nabla \cdot \frac{d\nabla_\perp \phi}{dt} \approx n \frac{d\nabla_\perp^2 \phi}{dt} \tag{2.21}$$

This approximation will be introduced at this stage; however, it will be revisited and relaxed later in this thesis.

The frictional drift, that is the drift due to electron-ion collisions, have already been found and takes the same form in the ion continuity equation as expressed in the electron continuity equation. This is expressed in equation 2.14.

The viscosity drift is quite difficult to get an expression for, but for the perpendicular viscosity term we can apply an approximation for the divergence of the viscosity tensor π by [16]

$$\nabla \cdot \pi \approx D_\Omega \nabla_\perp^2 \mathbf{u}_E \tag{2.22}$$

leading to the divergence of the ion viscosity term approximated to [7,16]

$$\nabla \cdot (n\mathbf{u}_{vis,\ i}) \approx -n \frac{m_i D_\Omega}{eB_0} \nabla_\perp^2 \Omega \tag{2.23}$$

where the lowest order drift vorticity given by

$$\Omega = \mathbf{b} \cdot \nabla \times \mathbf{u}_E = \frac{\nabla_\perp^2 \phi}{B_0}$$

has been introduced. Inserting the found terms for the different divergence terms, leads to the ion continuity equation of the form

$$\frac{\partial n}{\partial t} + \mathbf{u}_E \cdot \nabla n - \frac{2n}{B_0 R_0} \frac{\partial \phi}{\partial y} + \frac{nm_i}{eB_0} \frac{d\Omega}{dt} - D_n \nabla_\perp^2 n - n \frac{m_i D_\Omega}{eB_0} \nabla_\perp^2 \Omega + \nabla \cdot (n\mathbf{u}_{i\|}) = 0 \tag{2.24}$$

Subtracting equation 2.24 and equation 2.15 leads to the vorticity equation [1].

$$\frac{m_i n}{B_0} \frac{d\Omega}{dt} + \frac{2T_e}{B_0 R_0} \frac{\partial n}{\partial y} = \frac{m_i D_\Omega}{eB_0} \nabla_\perp^2 \Omega - \nabla \cdot \mathbf{J}_\| \tag{2.25}$$

where the parallel current $\mathbf{J}_\| = en(\mathbf{u}_{i\|} - \mathbf{u}_{e\|})$ is introduced.

2.1.4 Sheath Dissipation

To simplify the model equations further, we restrict our analysis to strictly two dimensions. Specifically the plane perpendicular to the magnetic field **B**. However, in the scrape-off layer (SOL), capturing the dynamics in the **B**-parallel direction is crucial. To account for these effects, we introduce an integration along the parallel direction to the magnetic field lines, defined through the operator expressed as [7]

$$\langle \cdot \rangle = \frac{1}{L_{\|}} \int_{-L_{\|}/2}^{L_{\|}/2} ds \tag{2.26}$$

Here, s represents the coordinate along the magnetic field lines, and $L_{\|}$ is the magnetic connection length. The magnetic connection length is a measure of the path length along a magnetic field line from a given point in the plasma to the nearest material surface. In this context, the sheath boundary conditions can be applied. When a reactor is first started, there is a transient phase where the plasma interacts with initially cold and electrically neutral walls. Due to the higher mobility and velocity of electrons compared with the ions, electrons strike the surface walls at a greater rate, resulting in the walls becoming negatively charged, This charge of the surface walls, leads to the formation of a thin sheath near the walls, typically with a size of a few Debye lengths into the plasma [7, 24]. Within this region, quasi-neutrality is no longer maintained, and the electron density (n_e) typically becomes less than the ion density (n_i) due to the accumulation of negative charges on the vessel walls [24].

Proceeding by integrating equation 2.15 and equation 2.25 using the operator defined in equation 2.26 and assuming that most of the quantities are constant over the **B**-parallel direction, the analysis can be simplified into determining the term

$$\langle \nabla \cdot (n\mathbf{u}_{e\|}) \rangle \tag{2.27}$$

in the electron continuity equation. And the term

$$\langle \nabla \cdot \mathbf{J}_{\|} \rangle \tag{2.28}$$

in the vorticity equation.

In the SOL, using a local Cartesian coordinate system where the magnetic field is given by $\mathbf{B} = B\hat{z}$, the parallel drift reduces to only having one component along the z-direction. Thus, to proceed with the analysis, we only need to evaluate a single component. Consequently we obtain

$$\langle \nabla \cdot (n\mathbf{u}_{e\|}) \rangle = \int_{-\frac{L_{\|}}{2}}^{\frac{L_{\|}}{2}} dz \frac{\partial}{\partial z} (n\mathbf{u}_{e\|}) = \hat{n} \cdot n\mathbf{u}_{e\|} \Big|_{-\frac{L_{\|}}{2}}^{\frac{L_{\|}}{2}} \tag{2.29}$$

and

$$\langle \nabla \cdot \mathbf{J}_{\|} \rangle = \int_{-\frac{L_{\|}}{2}}^{\frac{L_{\|}}{2}} dz \frac{\partial}{\partial z} \mathbf{J}_{\|} = \hat{n} \cdot \mathbf{J}_{\|} \Big|_{-\frac{L_{\|}}{2}}^{\frac{L_{\|}}{2}} \tag{2.30}$$

where $\hat{n}$ is the surface normal unit vector. As a result, the terms only need to be evaluated at the boundaries, where the sheath boundary conditions are applied.

In the sheath region, the electron density is typically given by [24]

$$n_e = n_{se} \exp\left(\Lambda - \frac{e\phi}{T_e}\right) \tag{2.31}$$

where the sheath edge density for a simple SOL, is given by $n_{se} = \frac{1}{2}n$ and $\Lambda = \ln\sqrt{m_i/2\pi m_e}$ are known as the sheath potential [24]. And in the same region, the electron velocity are given by [24]

$$\mathbf{u}_{\mathbf{e}\|} = c_s \hat{n} \tag{2.32}$$

the acoustic speed c_s. The parallel currents to sheath wall in a simple SOL can be described considering the ion and electron flux by [24]

$$\mathbf{J}_{\|} = e n_{se} c_s \left[1 - \exp\left(\Lambda - \frac{e\phi}{T_e}\right)\right] \hat{n} \tag{2.33}$$

and under the assumption of a steady-state plasma, the total current must be conserved. This implies that the current along a magnetic field line must be constant, and current leaving the sheath must be equal to the negative of the same current entering in order to avoid the accumulation of net charge within the region. Thus the currents also obey the the relation $\mathbf{J}_{s,\ edge} = -\mathbf{J}_{s,\ exit}$ [24].

With these results, the parallel expressions can evaluated to incorporate the sheath region in established equations.

$$\langle \nabla \cdot (n\mathbf{u}_{e\|}) \rangle = \frac{n c_s}{L_{\|}} \exp\left(\Lambda - \frac{e\phi}{T_e}\right) \tag{2.34}$$

$$\langle \nabla \cdot \mathbf{J}_{\|} \rangle = -\frac{e n c_s}{L_{\|}} \left[1 - \exp\left(\Lambda - \frac{e\phi}{T_e}\right)\right] \tag{2.35}$$

Inserted back into the equations, theses results yield the two-fluid model

$$\frac{\partial n}{\partial t} + \mathbf{u}_E \cdot \nabla n - \frac{2n}{B_0 R_0}\frac{\partial \phi}{\partial y} + \frac{2T_e}{eB_0R_0}\frac{\partial n}{\partial y} = D_n \nabla_\perp^2 n - \frac{n c_s}{L_{\|}} \exp\left(\Lambda - \frac{e\phi}{T_e}\right) \tag{2.36}$$

$$\frac{m_i n}{B_0}\frac{d\Omega}{dt} + \frac{2T_e}{B_0R_0}\frac{\partial n}{\partial y} = \frac{m_i D_\Omega}{eB_0}\nabla_\perp^2 \Omega + \frac{e n c_s}{L_{\|}}\left[1 - \exp\left(\Lambda - \frac{e\phi}{T_e}\right)\right] \tag{2.37}$$

2.1.5 Reduced Two-Fluid Model

The equations derived in the previous subsection contains numerous parameters. In order to develop a reduced set of two-fluid model equations that can be analyzed numerically in a computationally feasible manner, then further simplifications is required. While various ways to normalize the two-fluid model exists, this thesis adopts the *Bohm normalization*. In this framework, the spatial coordinates are normalized by the ion Larmor radius and time are normalized by the ion cyclotron frequency. The ion Larmor radius and the ion cyclotron frequency are defined through

$$\rho_s = \frac{\sqrt{T_e m_i}}{eB_0}, \quad \omega_{ci} = \frac{eB_0}{m_i} \tag{2.38}$$

The normalization are defined by

$$t \longrightarrow t' = \omega_{ci} t \tag{2.39}$$

$$x \longrightarrow \frac{x}{\rho_s} = x' \tag{2.40}$$

$$y \longrightarrow \frac{y}{\rho_s} = y' \tag{2.41}$$

which also indicates that the velocity $V' = V/c_s$, where c_s is the ion acoustic speed.

Further, the remaining variables are normalized by the introduction of the following dimensionless quantities

$$n' = \frac{n}{N_0}, \; \phi' = \frac{e\phi}{T_0}, \; T' = \frac{T_e}{T_0} \tag{2.42}$$

And the characteristic sizes for the diffusion coefficients

$$D'_n = \frac{D_n}{\rho_s^2 \omega_{ci}}, \quad D'_\Omega = \frac{D_\Omega}{\rho_s^2 \omega_{ci}} \tag{2.43}$$

To simplify the exponential function in the sheath dissipation term, a change of variables can be introduced. Let

$$-\phi' = \Lambda - \phi \tag{2.44}$$

which essentially sets the sheath potential, $\Lambda = 0$, which will simplify when the terms are considered further both analytically and numerically.

What can be noticed, is that the nonlinear term of the form

$$\mathbf{u}_E \cdot \nabla \tag{2.45}$$

can be further rewritten using the normalized expression for the electric drift leading to

$$\hat{z} \times \nabla_\perp \phi' \cdot \nabla \tag{2.46}$$

The unit vector in the z-direction appears due to the fact that the magnetic field are purely in the z-direction and as a consequence the magnetic field unit vector simplifies to the unit vector in z-direction.

Utilizing these simplifications and dropping the mark on the normalized variables and parameters, equation 2.36 and equation 2.37 can be simplified to give

$$\frac{\partial n}{\partial t} + \{\phi, n\} - gn\frac{\partial \phi}{\partial y} + g\frac{\partial n}{\partial y} = D_n \nabla_\perp^2 n - \sigma_n n \exp\left(-\phi\right) \tag{2.47}$$

$$\frac{\partial \Omega}{\partial t} + \{\phi, \Omega\} + g\frac{\partial \ln n}{\partial y} = D_\Omega \nabla_\perp^2 \Omega + \sigma_\Omega \left[1 - \exp\left(-\phi\right)\right] \tag{2.48}$$

where the Poisson bracket notation has been introduced in the particle density equation through

$$\{\phi, n\} = \hat{z} \times \nabla_\perp \phi \cdot \nabla n$$

and similarly for Ω in the vorticity equation. The observant reader will note that three new parameter have been introduced defined by

$$g = \frac{2\rho_s}{R_0}, \quad \sigma_n = \sigma_\Omega = \frac{\rho_s}{L_\parallel} \tag{2.49}$$

where g is the normalized effective gravity, σ_n and σ_Ω are the particle loss parameter and sheath dissipation parameter respectively.

Another simplification usually introduced along with the Boussinesq approximation, is that the partial derivative of the density in the vorticity equation can be written as

$$\frac{1}{n}\frac{\partial n}{\partial y} = \frac{\partial \ln n}{\partial y} \tag{2.50}$$

The model equation can also be expressed in a semi-Boussinesq way, where the $\frac{1}{n}\frac{\partial n}{\partial y}$ are retained, but the gradient of the particle density are neglected. This form is the one applied in the simulations, which will be discussed more later in the thesis.

The model comprising equations 2.47 and 2.48 constitutes the primary focus of this thesis. These equations are employed in order to simulate isolated plasma blob structures within the scrape-off layer (SOL) of fusion devices.

2.1.6 Reduced Two-Fluid Model; Non-Boussinesq

In the derivation of the reduced two-fluid model equations presented earlier in this section, the Boussinesq approximation or the thin-layer approximation was employed. However, since the scope of this thesis also contains scenarios where the Boussinesq approximation is not applicable, it will be appropriate to provide the two-fluid model formulated without invoking the Boussinesq approximation.

The introduction of the approximation was done when considering the ion polarization drift in the vorticity equation, specifically equation 2.21, where the term containing the gradient of the particle density is neglected. However, when we relax the thin-layer approximation, this term cannot be neglected and has to be retained in the vorticity equation. The rest of the terms remains unchanged, and so in the case when the Boussinesq approximation is relaxed, the model equations takes the form

$$\frac{\partial n}{\partial t} + \{\phi, n\} - gn\frac{\partial \phi}{\partial y} + g\frac{\partial n}{\partial y} = D_n \nabla_\perp^2 n - \sigma_n n \exp\left(-\phi\right) \tag{2.51}$$

$$\frac{\nabla_\perp n}{n} \cdot \frac{d\Omega}{dt} + \frac{\partial \Omega}{\partial t} + \{\phi, \Omega\} + \frac{g}{n}\frac{\partial n}{\partial y} = D_\Omega \nabla_\perp^2 \Omega + \sigma_\Omega \left[1 - \exp\left(-\phi\right)\right] \tag{2.52}$$

Or written in a more compact form as

$$\frac{\partial n}{\partial t} + \{\phi, n\} - gn\frac{\partial \phi}{\partial y} + g\frac{\partial n}{\partial y} = D_n \nabla_\perp^2 n - \sigma_n n \exp\left(-\phi\right) \tag{2.53}$$

$$\nabla \cdot \left(n\frac{d\Omega}{dt}\right) + g\frac{\partial n}{\partial y} = D_\Omega n \nabla_\perp^2 \Omega + \sigma_\Omega n \left[1 - \exp\left(-\phi\right)\right] \tag{2.54}$$

The compact written form of the non-Boussinesq model equations will be taken advantage of in the derivation of energy integrals which will be presented at a later stage in the thesis.

2.2 Center of mass

When analyzing isolated coherent blob structures in the SOL region, it can be advantageous to utilize the center of mass diagnostics to characterize the movement throughout the region. The position and velocity of the center of mass for a system of particles provides a concise description of the overall motion. The center of mass position describes the weighted average location of all particles in the system, while the center of mass velocity represented the weighted average of the velocity where the weights are the masses of the individual particles present.

This section contains a short description of some useful center of mass diagnostics which are useful to apply when studying the time-evolution of isolated blob-like filaments. The concepts are introduced for a continuous structure, when all involved quantities are normalized which makes them applicable to use with the reduced two-fluid model equations derived in the last section. The introduced concepts are position, velocity and energy. These will involve integrals and derivatives which will not be solved analytically, but solved by using numerical schemes for derivative and integrations. The two methods used are the composite trapezoid method for integration and the finite difference scheme for derivatives. These are introduced in section A.1 and section A.2 respectively, in the appendix.

2.2.1 Position and Velocity

The center of mass position of a particle system is the point where the weighted sum of each position vector of the individual particles present in the system adds to zero, which in the scene of statistics is comparable to the location of the mean for a given distribution. In the case of a continuous normalized distribution with density $n(\mathbf{x}, t)$ within a volume $\mathbf{V}$, then the center of mass position are given by

$$\mathbf{X}_{\text{com}}(t) = \frac{1}{M} \int_D dV\ \mathbf{x} n(\mathbf{x}, t) \tag{2.55}$$

where the integral is over the domain D, in this case a two-dimensional plane, $\mathbf{x} = (x, y)$ and M is the conserved particle normalized mass. Since the main focus of this thesis are on the radial center of mass diagnostics, then the most interesting position is the radial component given by

$$X(t) = \frac{1}{M} \int_D dV\ x n(\mathbf{x}, t) \tag{2.56}$$

It is well-established from classical mechanics that velocity is the time derivative of the position vector. This relationship forms a basis for the description of motion, as velocity describes the rate of change of position due to time. Following this, the center of mass velocity is defined by

$$\mathbf{V}_{com}(t) = \frac{d\mathbf{X}_{com}(t)}{dt} \tag{2.57}$$

Since the radial motion is the focus, then the more interesting quantity are the radial velocity component given by

$$V_x(t) = \frac{dX(t)}{dt} \tag{2.58}$$

which are normalized by the ion acoustic velocity c_s.

2.2.2 Energy Integrals

When analyzing the center of mass movement of blob structures, it can be useful to compute the kinetic and potential energy of the isolated blob. These calculations can, among other purposes, serve as a diagnostic tool to access if the simulations are reliable or not.

Due to the small electron mass compared to the ion mass, the electron contributions can be neglected and the kinetic energy are determined by the ions. The lowest order drifts for a general particle species s are the electric drift and diamagnetic drift. However under the assumption of cold ions presented earlier in the thesis, the diamagnetic drift vanish and the lowest order drift retained is the electric drift. Utilizing this, the kinetic energy for a system of particles spanning the volume **V** can be expressed by

$$K(t) = \frac{1}{2}\int_D dV \; n(\mathbf{x}, t)\mathbf{u}_E^2 \tag{2.59}$$

or alternatively by

$$K(t) = \frac{1}{2}\int_D dV \; (\nabla_\perp \phi)^2 \; n(\mathbf{x}, t) \tag{2.60}$$

where the approximated expression for the electric drift in the local Cartesian coordinate system is applied.

The potential energy which for a general magnetic field, are composed by two components; one due to the magnetic field and one due to gravitational potential, will in the case of a curved magnetic field be simplified to an effective gravitational potential energy [27]. The effective gravitational potential energy is expressed by

$$G(t) = g\int_D d\mathbf{x} \; xn(\mathbf{x}, t) \tag{2.61}$$

Using the definition of the center of mass position stated in equation 2.56, the expression for the effective potential gravitational energy can be rewritten

$$G(t) = MgX(t) \tag{2.62}$$

which is recognizable from the familiar equation for the gravitational potential energy mgh from classical mechanics. Where m mass of the object, g gravitational constant and h height above a certain reference level.

These expression will be used later in the thesis when an analytical expression for the energy integrals, are obtained.

/3

Energy Integrals

This chapter contains the derivation of energy invariants using a simplified model relaxing the Boussinesq approximation, and retaining the particle loss parameter and the sheath dissipation parameter. The validity of the derived invariants are test utilizing numerical simulations of blob structures, and further compared to numerical computations of the same quantities. This in done in chapter 4, which contains the numerical simulations and results.

3.1 Derivation for Simplified Model

To derive analytical expressions for the derivative of the energy integrals, it is convenient to introduce simplifications to the reduced model derived in section 2.1 due to the complexity of the equations. Neglecting the diamagnetic drift compression, diffusion in the density equation and the density factor in the diamagnetic drift compression term in the vorticity equation. Along with neglecting the diffusion term in the vorticity equation, and linearizing both the particle loss term and the sheath dissipation term using a Taylor expansion for the exponential function. This yields simplified equations of the form

$$\frac{\partial n}{\partial t} + \{\phi, n\} - g\frac{\partial \phi}{\partial y} = -\sigma_n n \tag{3.1}$$

$$\nabla \cdot \left(n\frac{d\nabla_\perp \phi}{dt} \right) + g\frac{\partial n}{\partial y} = \sigma_\Omega n\phi \tag{3.2}$$

where the Boussinesq approximation are relaxed. Prior to analyzing the simplified model equations, it is beneficial to explore a relation that will prove to be very useful. Further analyzing the time derivative of the square of gradient of ϕ gives

$$\frac{d}{dt}(\nabla_\perp\phi)^2 = \frac{d}{dt}(\nabla_\perp\phi \cdot \nabla_\perp\phi) = \frac{d\nabla_\perp\phi}{dt} \cdot \nabla_\perp\phi + \nabla_\perp\phi \cdot \frac{d\nabla_\perp\phi}{dt} = 2\nabla_\perp\phi \cdot \frac{d\nabla_\perp\phi}{dt}$$

Rewritten gives

$$\Rightarrow \frac{1}{2}\frac{d}{dt}(\nabla_\perp\phi)^2 = \nabla_\perp\phi \cdot \frac{d\nabla_\perp\phi}{dt} \tag{3.3}$$

Which is a quite useful result and will be utilized later in the derivation of the energy integrals.

To simplify the integrations required to derive analytical expressions for the energy integrals, some specific boundary conditions must be imposed in both the x- and y-directions. *Neumann* boundary conditions will be used in the x-direction, defined through

$$\frac{\partial n(0,y,t)}{\partial x} = \frac{\partial n(L_x,y,t)}{\partial x} = \frac{\partial \phi(0,y,t)}{\partial x} = \frac{\partial \phi(L_x,y,t)}{\partial x} = 0 \tag{3.4}$$

where L_x are the x-size of the domain and additionally, the derivative of the vorticity are also vanishing at the x-boundaries. In the y-direction, *periodic* boundary conditions will be utilized. This are defined through

$$n(x,0,t) = n(x,L_y,t), \quad \frac{\partial n(x,0,t)}{\partial y} = \frac{\partial n(x,L_y,t)}{\partial y} \tag{3.5}$$

$$\phi(x,0,t) = \phi(x,L_y,t), \quad \frac{\partial \phi(x,0,t)}{\partial y} = \frac{\partial \phi(x,L_y,t)}{\partial y} \tag{3.6}$$

where L_y are the y-size of the domain. Additionally the vorticity are subjected to the same boundary conditions in y.

Proceeding to the derivation of the energy integrals, we begin with the kinetic energy integral. This is achieved by multiplying equation 3.2 by ϕ and integrating over the domain denoted D.

$$\int_D d\mathbf{x}\,\phi\nabla\cdot\left(n\frac{d\nabla_\perp\phi}{dt}\right) + g\int_D d\mathbf{x}\,\phi\frac{\partial n}{\partial y} = \sigma_\Omega\int_D d\mathbf{x}\,n\phi^2 \tag{3.7}$$

Utilizing a term-by-term approach on equation 3.7, and considering the first term on the left hand side and rewriting using well known vector relations. Combined with the divergence theorem and utilizing the boundary conditions specified earlier, one can rewrite

$$\int_D d\mathbf{x}\,\phi\nabla\cdot\left(n\frac{d\nabla_\perp\phi}{dt}\right) = -\int_D d\mathbf{x}\,\nabla_\perp\phi\cdot\left(n\frac{d\nabla_\perp\phi}{dt}\right) = -\int_D d\mathbf{x}\,n\nabla_\perp\phi\cdot\frac{d\nabla_\perp\phi}{dt}$$

Applying the useful relation obtained in equation 3.3, the following are obtained

$$\Rightarrow \int_D d\mathbf{x}\, \phi \nabla \cdot \left(n \frac{d\nabla_\perp \phi}{dt} \right) = \int_D d\mathbf{x}\, \frac{1}{2} n \frac{\partial}{\partial t} (\nabla_\perp \phi)^2 \tag{3.8}$$

Moving on to the second term on the left hand side of equation 3.7

$$g \int_D d\mathbf{x}\, \phi \frac{\partial n}{\partial y} \tag{3.9}$$

Using the product rule for derivation over the variable y, this integral can be rewritten

$$g \int_D d\mathbf{x}\, \phi \partial_y (n) = g \int_D d\mathbf{x}\, \partial_y (n\phi) - g \int_D d\mathbf{x}\, n \partial_y (\phi) = -g \int_D d\mathbf{x}\, n \partial_y (\phi) \tag{3.10}$$

The first term is evaluated to zero due to the imposed boundary conditions and the remaining term can be recognized as the radial density flux [12]. And equation 3.7 reduces to

$$\Rightarrow \int_D d\mathbf{x}\, \frac{1}{2} n \frac{\partial}{\partial t} (\nabla_\perp \phi)^2 = -g \int_D d\mathbf{x}\, n \frac{\partial \phi}{\partial y} - \sigma_\Omega \int_D d\mathbf{x}\, n \phi^2 \tag{3.11}$$

From section 2.2.2, the definition of the kinetic energy integral are

$$K = \frac{1}{2} \int_D d\mathbf{x}\, n (\nabla_\perp \phi)^2 \tag{3.12}$$

Taking the time derivative of the kinetic energy integral and since the boundary conditions does not depend on time, the derivative can be moved inside the integration. Using the product rule, the time derivative of the kinetic energy integral can be written by

$$\frac{dK}{dt} = \frac{1}{2} \int_D d\mathbf{x}\, \frac{\partial n}{\partial t} (\nabla_\perp \phi)^2 + \frac{1}{2} \int_D d\mathbf{x}\, n \frac{\partial}{\partial t} (\nabla_\perp \phi)^2 \tag{3.13}$$

Proceeding with the second term in equation 3.13.

$$\int_D d\mathbf{x}\, \frac{\partial n}{\partial t} (\nabla_\perp \phi)^2 \tag{3.14}$$

This integral can rewritten using the particle density equation, defined in equation 3.1. Thus

$$\begin{aligned} \frac{1}{2} \int_D d\mathbf{x}\, \frac{\partial n}{\partial t} (\nabla_\perp \phi)^2 = -\frac{1}{2} \int_D d\mathbf{x}\, \{\phi, n\} (\nabla_\perp \phi)^2 + \frac{g}{2} \int_D d\mathbf{x}\, \frac{\partial \phi}{\partial y} (\nabla_\perp \phi)^2 \\ - \frac{\sigma_n}{2} \int_D d\mathbf{x}\, n (\nabla_\perp \phi)^2 \end{aligned}$$

Using a term-by-term approach in order to rewrite the integral, and starting by considering the integral

$$-\frac{1}{2}\int_D d\mathbf{x}\ \{\phi, n\}(\nabla_\perp\phi)^2 \tag{3.15}$$

In order to solve the given integral, the integrand can be rewritten in terms of vector operations. Thus

$$\Rightarrow -\int_D d\mathbf{x}\ \hat{\mathbf{z}} \times \nabla\phi \cdot \nabla n\ \nabla_\perp\phi \cdot \nabla_\perp\phi \tag{3.16}$$

where the definition of the Poisson bracket are utilized and $(\nabla_\perp\phi)^2 = \nabla_\perp\phi \cdot \nabla_\perp\phi$. Utilizing vector relations and a constant unit vector $\hat{z}$ combined with integration-by-parts and divergence theorem using the boundary conditions, the expression above can be further simplified

$$-\int_D d\mathbf{x}\ \hat{\mathbf{z}} \times \nabla\phi \cdot \nabla n\ \nabla_\perp\phi \cdot \nabla_\perp\phi = \int_D d\mathbf{x}\ \nabla_\perp\phi \cdot \nabla_\perp\phi\ \nabla n\ \nabla \cdot (\hat{\mathbf{z}} \times \nabla\phi) \tag{3.17}$$

where the divergence in the last term can be expanded trough

$$\nabla \cdot (\hat{\mathbf{z}} \times \nabla\phi) = (\nabla \times \hat{\mathbf{z}}) \cdot \nabla\phi - \hat{\mathbf{z}} \cdot (\nabla \times (\nabla\phi)) = 0 \tag{3.18}$$

for which both terms evaluates to zero. The first due to no change in the unit vector leading to a zero curl, and the second due to the curl of a gradient is identically zero. Combining the terms yields

$$-\frac{1}{2}\int_D d\mathbf{x}\ \{\phi, n\}(\nabla_\perp\phi)^2 = 0 \tag{3.19}$$

Further considering the electric drift compression term, given by

$$\frac{g}{2}\int_D d\mathbf{x}\ (\nabla_\perp\phi)^2\frac{\partial\phi}{\partial y} \tag{3.20}$$

Again applying the vector form of the integrand, and rewriting gives

$$\int_D d\mathbf{x}\nabla_\perp\phi \cdot \nabla_\perp\phi\ \nabla \cdot (\hat{\mathbf{z}} \times \nabla\phi) \tag{3.21}$$

The divergence terms can be immediately recognized as the term shown in equation 3.18, and using the results we obtain

$$\frac{g}{2}\int_D d\mathbf{x}\ (\nabla_\perp\phi)^2\frac{\partial\phi}{\partial y} = 0 \tag{3.22}$$

and thus the expression vanishes. By combining the results of the various computed terms, the time derivative of the kinetic energy integral is expressed by

$$\frac{dK}{dt} = -g\int_D d\mathbf{x}\ n\frac{\partial\phi}{\partial y} - \sigma_\Omega\int_D d\mathbf{x}\ n\phi^2 - \frac{\sigma_n}{2}\int_D d\mathbf{x}\ n(\nabla_\perp\phi)^2 \tag{3.23}$$

The second term in this equation, given by

$$-\frac{\sigma_n}{2}\int_D d\mathbf{x}\, n(\nabla_\perp \phi)^2$$

can be rewritten using the definition of K into

$$-\sigma_n K \tag{3.24}$$

indicating that the particle loss term in the density equation, has to the lowest order an exponential decaying effect on the kinetic energy integral.

Having determined the time derivative of the kinetic energy integral, attention can now be shifted to determining the time derivative of the effective gravitational potential energy integral. From section 2.2.2 the expression for this energy integral is known to be

$$G = g\int_D d\mathbf{x}\, xn \tag{3.25}$$

Taking the time derivative of G and moving the derivative inside the integral, which is allowed due to the boundary conditions being constant in time. This leads to

$$\frac{dG}{dt} = g\int_D d\mathbf{x}\, x\frac{\partial n}{\partial t} \tag{3.26}$$

In order to derive the desired expression, we multiply equation 3.1 by gx and integrate over the domain.

$$g\int_D d\mathbf{x}\, x\frac{\partial n}{\partial t} + g\int_D d\mathbf{x}\, x\{\phi, n\} - g^2\int_D d\mathbf{x}\, x\frac{\partial \phi}{\partial y} = -\sigma_n g\int_D d\mathbf{x}\, xn \tag{3.27}$$

The first term in equation 3.27 can immediately be recognized as the time derivative of the effective gravitational potential energy integral. Proceeding with the second term, given by

$$g\int_D d\mathbf{x}\, x\{\phi, n\} \tag{3.28}$$

which can be simplified by first rewriting the Poission bracket utilizing the expanded form $\{\phi, n\} = \frac{\partial \phi}{\partial x}\frac{\partial n}{\partial y} - \frac{\partial \phi}{\partial y}\frac{\partial n}{\partial x}$. Thus the integral can be rewritten as

$$\int_D d\mathbf{x}\, x\frac{\partial \phi}{\partial x}\frac{\partial n}{\partial y} - \int_D d\mathbf{x}\, x\frac{\partial \phi}{\partial y}\frac{\partial n}{\partial x} \tag{3.29}$$

where the combined expression has been separated. Using integration-by-parts in x on the first term and in y on the second term gives

$$\int_D d\mathbf{x}\, n\frac{\partial \phi}{\partial y} + \int_D d\mathbf{x}\, n\frac{\partial^2 \phi}{\partial x \partial y} - \int_D d\mathbf{x}\, n\frac{\partial^2 \phi}{\partial x \partial y} = \int_D d\mathbf{x}\, n\frac{\partial \phi}{\partial y} \tag{3.30}$$

where the two last expressions cancels out. Thus the integral of the Poisson bracket can be written as

$$g \int_D d\mathbf{x}\, x\{\phi, n\} = g \int_D d\mathbf{x}\, n \frac{\partial \phi}{\partial y} \tag{3.31}$$

which can be recognized as the density flux in the radial direction [12]. Continuing on with this approach leads to considering the term

$$g^2 \int_D d\mathbf{x}\, x \frac{\partial \phi}{\partial y} \tag{3.32}$$

Rewriting using product rule in y gives

$$\int_D d\mathbf{x}\, x \partial_y \phi = \int_D d\mathbf{x}\, \partial_y (x\phi) - \int_D d\mathbf{x}\, \partial_y (x) \phi = 0$$

where $\partial_y = \frac{\partial}{\partial y}$. Due to the periodic boundary conditions in y-direction, the contribution from the first term vanishes. And since x and y are independent variables the second term evaluates to zero, giving

$$g^2 \int_D d\mathbf{x}\, x \frac{\partial \phi}{\partial y} = 0 \tag{3.33}$$

Combining the results obtained into equation 3.27, it follows that the time derivative of the effective gravitational potential energy integral is given by

$$\frac{dG}{dt} = -g \int_D d\mathbf{x}\, n \frac{\partial \phi}{\partial y} - \sigma_n G \tag{3.34}$$

where

$$G = g \int_D d\mathbf{x}\, xn$$

Showing that to the lowest order, the effect of the particle loss term in in the density equation has a exponential decaying effect on the potential energy integral. This is the same effect observed for the same term in the derivative of the kinetic energy integral.

With the expressions for the time derivative of the kinetic energy integral and the effective gravitational potential energy integral now established, they can be combined into an expression for the time derivative of the total energy in the system.

$$\frac{dK}{dt} + \frac{dG}{dt} = -2g \int_D d\mathbf{x}\, n \frac{\partial \phi}{\partial y} - \sigma_\Omega \int_D d\mathbf{x}\, n\phi^2 - \sigma_n K - \sigma_n G \tag{3.35}$$

with

$$K = \frac{1}{2} \int_D d\mathbf{x}\, n(\nabla_\perp \phi)^2, \quad G = g \int_D d\mathbf{x}\, xn$$

Neglecting the sheath dissipation and particle loss effect in both the density and the vorticity equation results in a simplified expression for the difference in the time evolution of the kinetic energy integral and the effective potential energy integral expressed as

$$\frac{dK}{dt} - \frac{dG}{dt} = 0 \tag{3.36}$$

So in the case of no sheath dissipation and no particle loss, the result given in equation 3.36 is consistent with the results obtained in ref [27], when they consider a simple expression for a curved magnetic field.

The validity of the resulting energy relations derived from the heavy simplified model defined at the beginning of this section, will be further analyzed and discussed in the next chapter, when simulations of the reduced two-fluid model equations are the main focus.

4

Numerical Simulations

This chapter contains the numerical simulations, results and discussion on the simulations and results. At the start of each section, there is stated a short description of the model equations used to simulate isolated blob structures, along with previous results from publications which has investigated the given topic. The results from the simulations are given in a separate subsection, where we also comment and describe the results. The discussion on the results and comparing to previous results if they exists, is done at the end of each section in a separate subsection. In the first subsection, the setup of the code, initial conditions and parameter values will be discussed. The parameter values will also be specified at the beginning of each section, in order to prevent misinformation of the used parameter value and ensuring reproducibility of the simulations.

4.1 Simulation Setup and Reference Values

This section outlines the simulation configuration and constant values for parameters not varied in the parameter scan for simulations. The configuration contains the programs used for numerical solutions to the model equations, the domain specifications and boundary conditions applied to the respective quantities. The model equations and parameters used in the various simulations will also be stated at the start of each parameter scan, in order to make the simulations easier to follow and also recreate.

The numerical framework utilized to simulation of the isolated blob-like structures at the scrape-off layer of fusion devices, is the BOUT++ framework [9]. Boundary Turbulence in C++ or BOUT++ as it is known as, is a framework that solves and simulates non-linear equations in 2D and 3D curvilinear coordinates. Its main use is plasma fluid equations, but it can also handle general time-dependent equations [9]. Once the framework has been successfully compiled, it is quite easy to utilize. By specifying parameter values and initial conditions for the respective quantities in a BOUT.inp file, the simulation parameter can be defined which allows the user to easily modify simulations environment to fit specified situations. The output are dumped into .dmp.nc files, which can be further handled with the ”xBOUT” Python package for data handling. More information on the package can be obtained from: https://github.com/boutproject/xBOUT. The packges utilized ”xArray”, which is sort of a combination of ”Pandas” and ”NumPy” for multidimensional array handling. For more information on the ”xArray” package see: https://docs.xarray.dev/en/stable/.

This BOUT++ framework is open source and can be obtained from the GitHub page; https://github.com/boutproject/BOUT-dev. The GitHub page comes with a manual and examples of how to use the given framework. All simulations run in the thesis make use of the BOUT++ framework combined with different numerical solvers. The use of a already established framework for numerical simulations, removes the added workload of creating a potentially unstable numerical solver, since the framework already has been numerically tested for stability.

In order to solve the model equations specified in chapter 2; the reduced two-fluid model equations, two types of solvers are needed. One which solves the equations when the Boussinesq approximation has been imposed and one which can handle solving without the Boussinesq approximation. In the case of implementation using Boussinesq, the BOUT++ framework in two dimensions utilizes a built-in cyclic solver. For the case when the Boussinesq approximation is relaxed, the BOUT++ framework needs to utilized a non-linear solver, and in the case for the simulations used here, it utilizes ”PETSc”. This is an open source non-linear solver obtained from: https://github.com/petsc/petsc/tree/release-3.19. Note that version 3.19 of the PETSc solver has been utilized, since it is the version which is most compatible with the BOUT++ framework at the writing of this thesis.

The domain specifications are consistent across all simulations, with variations applied only to the parameters and the initial condition to the density perturbation. The domain lengths are defined as $L_x = 200\rho_s$ and $L_y = 100\rho_s$, with a grid resolution of 512×256. The simulation time step is set to correspond to one ion cyclotron frequency (ω_{ci}) and further the output datasets are maintained at 200 steps. Consequently, each dataset contains $200\omega_{ci}$ outputted time steps containing values of density, vorticity and potential of a two dimensional grid. However, for some of the more computationally heavy simulations the dataset may contain fewer outputted time steps than $200\omega_{ci}$, but not shorter than $100\omega_{ci}$. From this point and throughout the rest of this thesis, all parameters and plots will be given in dimensionless units, unless explicitly denoted.

When it comes to the spatial size of the blob structures, it has been observed in experiments that the typical blob structure size is around $0.5-2$cm. And the ion Larmor radius is typically $\rho_s \approx 10^{-3}$m, combined with a typical major radius of $R_0 \approx 1$m [2, 12, 17, 18, 22]. To ensure that the blob remains relatively localized so that the evolution of the density and the potential are unaffected by the boundaries, the normalized size of of the blob structures is set to $l = 0.03L_x = 0.03 \cdot 200\rho_s$ which gives $l = 6$ in dimensionless size. And since a blob size of 0.5cm is 5 in normalized units, the chosen value is comparable to measurements made in experiments. By the typical SOL values, the dimensionless parameter for the effective gravity are approximately $g \approx 10^{-2}$ and the dimensionless particle loss parameter and sheath dissipation parameter σ_n and σ_Ω is set to $\sim \frac{\rho_s}{L_\parallel} = 10^{-4}$ when the parameter are not varied. Here we have used that the typical value of the magnetic connection length is $L_\parallel \approx 10$m [12]. The diffusion coefficient is set to 10^{-4} to add a small diffusivity in every simulation [2, 5, 12, 17, 18, 22].

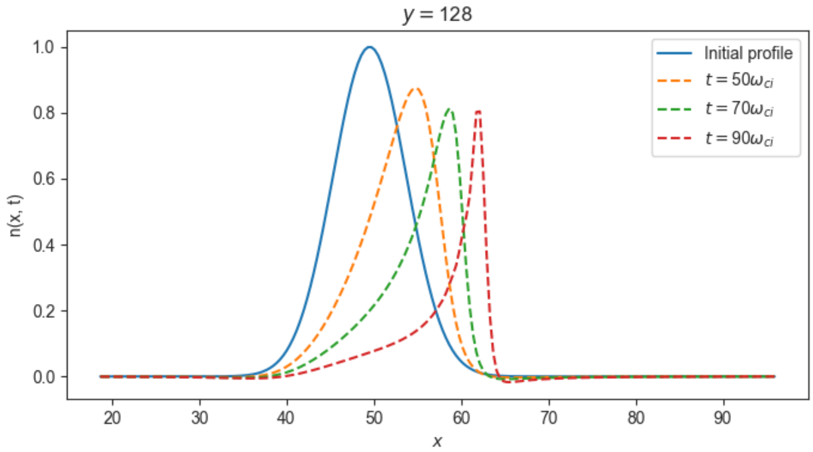

Figure 4.1: Density profile for initial amplitude $\Delta n/N = 1$ showing the Burgers' solution effect on the profile as it evolves. The interaction between the background density and the blob produces sheared flows, which produces formation of the steep leading edge and a trailing wake observed in the figure [5].

Figure 4.1 shows the an initially symmetric blob with $\Delta n/N = 1$, retained Boussinesq approximation combined with no sheath dissipation and no particle loss. The blob is simulated using the model introduced in section 2.1.5. It shows the density profile of the blob taken at $y = 50\rho_s$ and shown for four time steps. The blue line is the initial density profile as the shape of a Gaussian blob, and the dotted lines show the evolution of the profile for three time steps of $50\omega_{ci}$, $70\omega_{ci}$ and $90\omega_{ci}$. From the figure it is clear that as the density profile evolves over time, the profile becomes more localized as a consequence of the fact that velocity scales as a power law of density in the initial phase of blob evolution when dissipation is neglected are [3, 11, 12, 18, 20–22]

$$V_x \sim n(t)^\alpha \tag{4.1}$$

and the density evolution for a single density peak are determined by

$$\frac{\partial n}{\partial t} + n(t)^\alpha \frac{\partial n}{\partial x} = -\sigma n \tag{4.2}$$

to lowest order, where the particle loss term is linearized. This can be recognized as Burgers' equation for a one-dimensional problem, which quickly breaks down. Thus in order for the code to be numerically stable, the diffusion term must be present for all simulations, and the value will remain unchanged throughout all parameter scans and simulations. They are set to a values of the same order as the particle loss and sheath dissipation terms value of 10^{-4}.

The potential, density and vorticity have Neumann boundary conditions at both the x-boundaries and are periodic at both boundaries in y-direction. These where introduced in section 3.1. The initial conditions for the potential and the viscosity are set to zero, $\phi(x, y, 0) = \Omega(x, y, 0) = 0$ and the density profile is initialized as a Gaussian perturbation of the form

$$\frac{n(x, y, t)}{N} = 1 + \frac{\Delta n}{N} \exp\left(-\frac{(\mathbf{x} - \mathbf{x}_0)^2}{2l^2}\right) \tag{4.3}$$

where Δn is the blob amplitude, N is the constant background density which will be identically equal to 1 for all simulations and $\mathbf{x}_0$ is the starting position of the blob defined as $(50\rho_s, 50\rho_s)$.

In order to evaluate blob center of mass motions, one has to be able to track the blob structures throughout the motion. There are several ways this can be accomplished, but here a threshold value on the density has been set to estimate the blob size. This can be defined using a set, given as

$$n_{blob} = \{n(x.y, t) \mid n(x, y, t) > \text{ threshold}\} \tag{4.4}$$

where the threshold value is set to 1×10^{-9}, the rest of the values are set to 0. Thus only density values above this threshold will contribute to determine the center of mass diagnostics of the various blob structures simulated. In the contour figures showing the density, the background density has been subtracted to only consider the blob structures. This is done in the processing part, and not in the simulation part. There the background density is present as a constant value of $N = 1$.

4.2 Energy Integrals

In chapter 3, an analytical expression for the kinetic- and effective gravitational potential energy was obtained utilizing a simplified model. Much of the motivation for obtaining invariants for systems, are the information they can provide on restrictions of the dynamics of a given system. And the use of invariants in numerical simulations, to verify their validity. In this thesis, the latter serves as the primary motivation for the use of the invariants. The restrictions on dynamics approach has been utilized in several previous publications, such as in ref. [27] where they use a relaxation of the Boussinesq approximation but neglect the particle loss and sheath dissipation terms among other simplifications used to simplify the complexity of the analytical expressions. Or in ref. [20] where the Boussinesq approximations is retained and sheath dissipation and particle loss terms are neglected, but the diffusion terms are retained.

To obtain an analytical expression for the invariants in chapter 3, a very simplified model where used. The model equations where obtained by linearize the particle loss and sheath dissipation terms, relaxing the Bouessinesq approximation and neglecting diamagnetic drift given by

$$\frac{\partial n}{\partial t} + \{\phi, n\} - g\frac{\partial \phi}{\partial y} = -\sigma_n n \tag{4.5}$$

$$\nabla \cdot \left(n \frac{d\nabla_\perp \phi}{dt} \right) + g\frac{\partial n}{\partial y} = \sigma_\Omega n \phi \tag{4.6}$$

and the derivation yielded the invariants

$$\frac{dK}{dt} + \frac{dG}{dt} = -2g\int_D d\mathbf{x}\, n\frac{\partial \phi}{\partial y} - \sigma_\Omega \int_D d\mathbf{x}\, n\phi^2 - \sigma_n K - \sigma_n G \tag{4.7}$$

and if we imposing no particle loss and sheath dissipation parameter $\sigma_n = \sigma_\Omega = 0$, combined with subtracting the time derivatives of the energy integrals gives

$$\frac{dK}{dt} - \frac{dG}{dt} = 0 \tag{4.8}$$

which reveals that the difference in the time derivative of the energy integrals is zero. However, in the simulations of the blob structures we will not linearize the particle loss and sheath dissipation terms. So the simulated model equations are given by

$$\frac{\partial n}{\partial t}\{\phi, n\} - g\frac{\partial \phi}{\partial y} = D_n \nabla_\perp^2 n - \sigma_n n \exp(-\phi) \tag{4.9}$$

$$\nabla \cdot \left(n \frac{d\nabla_\perp \phi}{dt} \right) + g\frac{\partial n}{\partial y} = D_\Omega \nabla_\perp^2 \Omega + \sigma_\Omega n[1 - \exp(-\phi)] \tag{4.10}$$

where diffusion are added for stability. This model equations leads to a modification in the particle loss term and the sheath dissipation term, yielding the invariant equation

$$\begin{aligned}\frac{dK}{dt} + \frac{dG}{dt} = -2g\int_D d\mathbf{x}\, n\frac{\partial \phi}{\partial y} - \sigma_\Omega \int_D d\mathbf{x}\, n[1 - \exp(-\phi)] \\ - \frac{\sigma_n}{2}\int_D d\mathbf{x}\, n(\nabla_\perp \phi)^2 \exp(-\phi) - \sigma_n \int_D d\mathbf{x}\, xn \exp(-\phi)\end{aligned} \tag{4.11}$$

where the terms are now no longer linearized. In the case of no particle loss and no sheath dissipation, this gives the invariant stated in equation 4.8. And so the invariants which will be studied through simulations in this section in the case of particle loss and sheath dissipation terms, given in equation 4.11. In order to simulate blob structures we utilize the parameter values $g = 0.01$, $l = 6$, neglecting diamagnetic drift compression in the particle density equation and relaxing the Boussinesq approximation. To ensure the stability of the simulations, the diffusion terms will be reintroduced into the simulated model equations. The diffusion terms will act as sink terms in the energy equations, and thus a difference in the results from the simulations and the analytical expressions found is to be expected.

In the simulations where particle loss and sheath dissipation is retained, the values used are $\sigma_n = \sigma_\Omega = 10^{-4}$. Further the blob structure are initialized as a symmetric blob with initial perturbed amplitude of $\Delta n/N = 1$ and the background density are set to $N = 1$ as is the case for all simulations done in this thesis.

4.2.1 Simulations Results

The following subsection contains the results from the energy integrals simulations and contains a description of the results.

Particle loss and sheath dissipation included

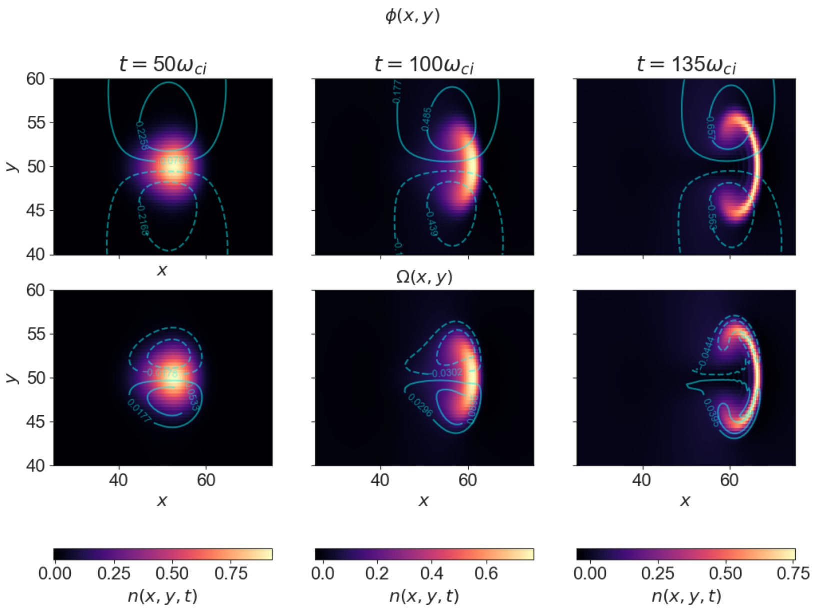

Figure 4.2: Density shown as colored contour in all plots. The potential shown as blue curves on the top, and the vorticity as blue curves on the lower row. Dotted lines corresponds to negative values, and lines to positive values. The blob structure is observed to moves radially in the positive x-direction.

Figure 4.2 shows the evolution of an initial symmetric blob structure with perturbed amplitude $\Delta n/N = 1$ over three different time steps, along with the electrostatic potential and the vorticity for each of the time steps. Density is shown as colored contours in all the plots, further the potential is shown as blue curves along with the density on the top row and the vorticity is shown as blue curves on the bottom row. Dotted lines corresponds to negative values and the lines corresponds to positive values. The blob is initially a symmetric structure, but through the formation of a electrostatic potential and a vorticity field the blob is accelerated radially in the positive x-direction [3, 12]. The blob structure develops a steeping front and a trailing wake, resembling the effect of Burgers' equation in one-dimensional problem, which was discussed in section 4.1. The particle dissipation and diffusion combined with stretching due to convective flow, leads to a decreasing perturbation amplitude as the blob moves radially outwards [12, 13]. This leads to the creation of the two observed lobes on either side of the main structure, leading to the formation of a mushroom shape, this is referred to as Kelvin-Helmholtz vortices and vortex shedding [2].

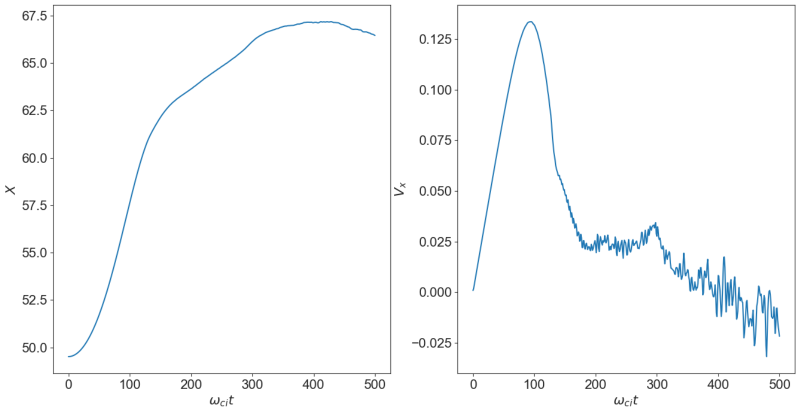

Figure 4.3: Left shows the center of mass radial position of the blob structure observed in figure 4.2. Right shows the computed center of mass radial velocity for the same structure. All axis are dimensionless, but time axis emphasized for readability.

The disjoint lobe structures have a net different vorticity polarity [3, 11–13]. Figure 4.3 shows the computed center of mass radial position and velocity of the blob structure shown in the contour plot in figure 4.2. The center of mass diagnostics are computed numerically using the definitions specified in section 2.2 combined with using the numerical approximation methods defined in A.1 and A.2 respectively. The blob structure are initially at rest, but quickly reach an advection phase where it starts to accelerate outwards radially. It reaches a maximum after approximately 100 time steps for which it has traveled a distance of several ion Larmor radius ρ_s. Due to the diffusion and dissipation of density, the structures front vanishes, and the blob decelerates and the motion stops somewhat. The further dissipation and diffusion leads to the vanishing of the blob density into making it indistinguishable from the background density, which leads to the noisy pattern reach after approximately $300\omega_{ci}$. This effect explains the behavior seen in the radial position figure, where the blob appears to move in the negative radial direction.

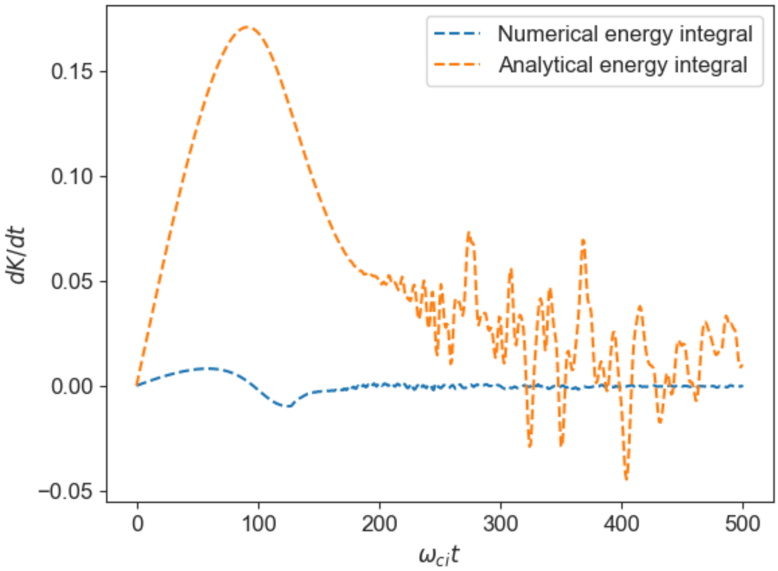

Figure 4.4: Shows the time derivative of the kinetic energy integrals. The blue line corresponds to the numerical solution and the orange line corresponds to the analytical solution.

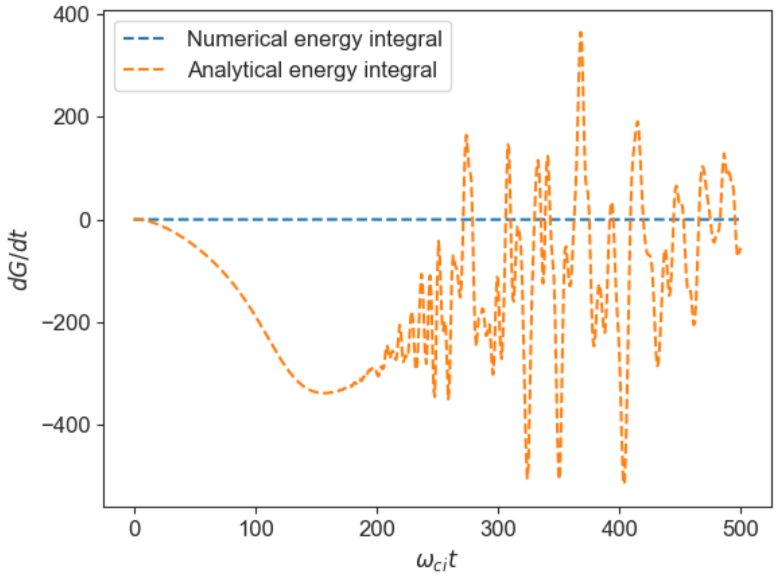

Figure 4.5: Shows the time derivative for the effective gravitational potential energy. Blue line corresponds to numerical solution and the orange line corresponds to the analytical solution.

Figure 4.4 shows the time derivative of the kinetic energy integral, both the estimated numerical solution and the found analytical solution defined in chapter 3. Figure 4.5 shows the time evolution of the derivative of the effective gravitational potential energy, also here both the numerical and the analytical solutions. To compute both solutions require numerical integrations and derivatives, which are solved utilizing the numerical methods defined in A.1 and A.2 respectively. From the figure showing the time derivative of the kinetic energy integral, considering the analytical solution computed using we observe a sharp increase in the derivative of the kinetic energy of the blob as the formation of the electrostatic potential and vorticity field accelerates the structure radially outwards. After about 100 time steps, we observe a decreasing derivative of the kinetic energy which slows down as the curve approaches zero value. Considering the curve for the numerical computation of the derivative of the kinetic energy integral, we observe a slight increase as the blob is accelerated. However the value for the numerical computation increases very slow and reach a much lower value before it decreases to zero value. We observe a large difference in the analytical solution and the numerical value, but this difference in value can be a result of the neglection of diffusion in the analytical solutions. They would act as sinks, leading to a decrease in the derivative of the kinetic energy integral. After between 200 − 300 time steps, the solution appears to retain close to zero. However, the analytical curve becomes noisy and fluctuating around the same region which could be due to numerical error.

From the figure showing the time evolution of the derivative of the effective gravitational potential energy, we see that the numerical curve appears to stay close to or be zero throughout the simulation. The analytical curve decrease as the blob is accelerated, before it rises up towards zero value. We have again not considered the diffusion part, which is present due to the stability of the simulations. Thus a difference in the curves could be as a result of the neglection of the terms in the analytical solution.

Figure 4.6 show the computed energy integrals for the kinetic energy and the effective gravitational potential energy. Both are computed using composite trapezoid method for numerical integration, this method is shown in section A.2 in the appendix. From the kinetic energy figure, 4.6a we observe the increase in kinetic energy as the radial velocity of the blob increases. After reaching a maximum when the blob reaches a maximum radial COM velocity, the kinetic energy is observed to decrease with increasing time slowly approaching a zero value as the blobs velocity approaches zero. Figure 4.6b shows the effective gravitational potential energy which starts at a high value, and is observed to decrease with increasing time and decreasing blob density. As the density of the blob stricture dissipates and diffuses, the resulting effect is a decrease in the potential energy. The decrease in potential energy is observed to be more or less linear over time.

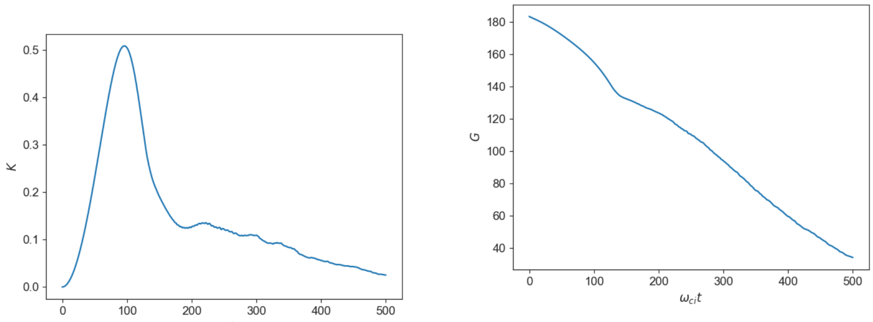

(a) Shows the time evolution of the computed kinetic energy integral.

(b) Shows the time evolution of the computed effective gravitational potential energy integral.

Figure 4.6: Time evolution of the computed energy integrals.

No sheath dissipation and no particle loss terms

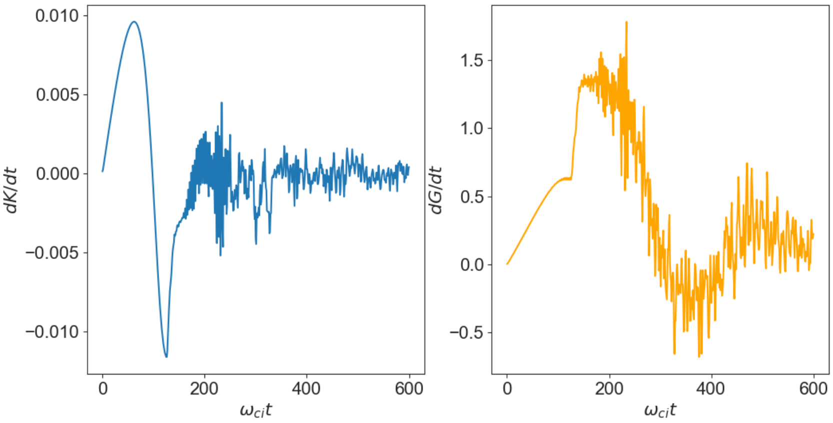

Figure 4.7: Left shows the time derivative of the kinetic energy integral. Right shows the time derivative of the effective gravitational potential energy integral.

Figure 4.7 shows the time derivative of the kinetic- and effective potential energy integrals. This is computed from a simulation a blob structure relaxing the Boussinesq approximation combined with neglecting the particle loss and sheath dissipation terms. The derivative of the kinetic energy integral starts at a value of zero, and increases with the increasing radial center of mass velocity of the blob structure. After reaching a maximum, it decreases with the decreasing radial velocity. The derivative of the effective gravitational potential energy increases from a starting value of zero, before reacting a maximum and further decreasing when the blob structure diffuses into the background density. It finally settles around a value of roughly zero.

Figure 4.8 shows the difference in the changes of the kinetic- and potential energy integrals. It starts out decreasing from an initial values of zero, before reaching a minimum and further increasing to a value around zero. The results will be further discussed in the next subsection.

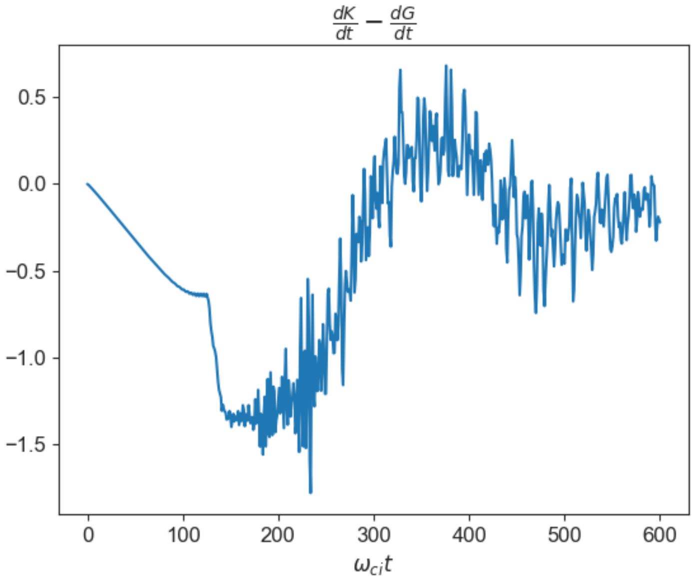

Figure 4.8: Difference of the time derivatives of the kinetic- and the potential energy integrals.

4.2.2 Discussion

In the case of sheath dissipation and particle loss terms added to the simulations, we obtained a difference between the derived invariants and the numerically computed invariants. However, in the derivation of the invariants we neglected the impact of diffusion which would appear as a sink in the energy integrals equations. From the figures, we observe a difference in the numerical computed derivative and the analytical solutions. This indicates that the may not converge well when particle loss and sheath dissipation are involved. In terms of the kinetic energy, the difference is small and could be due to numerical approximations. In the case of the effective potential energy, the difference appears to be large in value and only after about 300 time steps they appear to be close to similar. However, the analytical solution seems unstable at that point and experience fluctuations.

When the particle loss and sheath dissipation terms are neglected, then the invariants takes the form as found in ref [27]. In figure 4.8 we see that the difference between the derivative of the kinetic energy integral and the effective gravitational potential energy are small and mostly around a value of zero. However, the value are not exactly zero, showing some error which could come from numerical approximations. But the value seems to stay close to zero, which is roughly approximate to the analytical invariant solution found in chapter 3, and the same found in ref. [27].

4.3 Initial Amplitude Variations

Many previous publication focuses on the impact made from the initial perturbed amplitude of the blob structures on the radial center of mass motion, which also is the focus on the simulations in this section [12, 13, 18, 20, 21, 27].

The evolution of plasma filaments in magnetized plasmas, can also be described through the plasma vorticity equation given as [11, 21]

$$\mathbf{b} \cdot \nabla \times \left(\rho \frac{d\mathbf{V}}{dt} \right) = B\mathbf{B} \cdot \left(\frac{J_{\parallel}}{B} \right) + 2\mathbf{b} \cdot \kappa \times \nabla P \tag{4.12}$$

where P is the plasma pressure, ρ is the mass density, $\mathbf{V}$ is the fluid velocity of the plasma, $\mathbf{b}$ is the unit vector in the direction of the magnetic field lines and $\kappa = (\mathbf{b} \cdot \nabla)\mathbf{b}$ is known as the magnetic curvature vector. Under the assumption that parallel currents can be neglected, and utilizing an order of magnitude approach implying $\nabla_{\perp} \sim 1/l$, $d/dt \sim V/l$, $\kappa \sim 1/R$. That is, the perpendicular gradient scales inversely with the characteristic blob size, the material derivative scales as velocity divided by blob size and magnetic curvature vector scales inversely with magnetic field radius of curvature [21]. Finally using $\nabla P/\rho \sim c_s^2 \Delta n / l(N + \Delta n)$, which combined gives the inertial velocity scaling regime. In the case of small perturbed amplitudes $\Delta n/N \ll 1$, the scaling of the radial velocity of the filaments can be expressed as $V \sim (\Delta n/N)^{1/2}$ [11, 12, 18–21]. Showing a square-root dependence on the initial amplitude in the inertial scaling regime. In the limit of large initial perturbed amplitude $\Delta n/N \gg 1$, a saturation occur and the radial velocity of the filaments becomes independent of the initial amplitude $\Delta n/N$ [19, 21].

Utilizing the same arguments and approach as in the inertial scaling regime, but retaining the parallel effects closed as sheath dissipation, leads to the sheath dissipation scaling regime. Here velocity $V \sim \phi/Bl$ which balances the effect of parallel currents and interchange terms, which for small perturbed amplitudes $\Delta n/N \ll 1$ a scaling of $V \sim \Delta n/N$ [19, 21]. So in the case of retained sheath dissipation, the radial filament velocity scales linearly with the initial amplitudes. In the limit of large initial amplitude $\Delta n/N \gg 1$, the contributions from the parallel currents becomes vanishing compared to the other terms and consequently this leads to the same scaling as in the case of no parallel currents. Which again leads to the case of saturation, and the radial filament velocity becomes independent of initial amplitude. Much of the described literature neglects the influence of the particle loss term in the described scaling. In the section, the combined effect of the particle loss parameter and the sheath dissipation parameter will be considered.

The model equations used for the simulations, are the full model equations derived in chapter 2 where the Boussinesq approximation are invoked. These are given by

$$\frac{\partial n}{\partial t} + \{\phi, n\} - gn\frac{\partial \phi}{\partial y} + g\frac{\partial n}{\partial y} = D_n \nabla_\perp^2 n - \sigma_n n \exp(-\phi) \tag{4.13}$$

$$\frac{\partial \Omega}{\partial t} + \{\phi, \Omega\} + \frac{g}{n}\frac{\partial n}{\partial y} = D_\Omega \nabla_\perp^2 \Omega + \sigma_\Omega [1 - \exp(-\phi)] \tag{4.14}$$

The density is initialized as symmetric blob following a Gaussian shape, which is described in the setup section. The potential and vorticity are set to initial value of zero. Parameters are set to $g = 0.01$, $D_n = D_\Omega = \sigma_n = \sigma_\Omega = 10^{-4}$. In the simulations where particle loss and sheath dissipation are neglected, the parameters are set to $\sigma_n = \sigma_\Omega = 0$ and the rest of the parameters retains their values. If they are retained, their value are set to $\sigma_n = \sigma_\Omega = 10^{-4}$. The center of mass position and velocity are computed using the definition combined with the numerical methods defined in the sections A.1 and A.2.

4.3.1 Simulations Results

This subsection contains the results from the parameter scan in the initial perturbation amplitude, along with a short description.

No sheath dissipation and no particle loss term

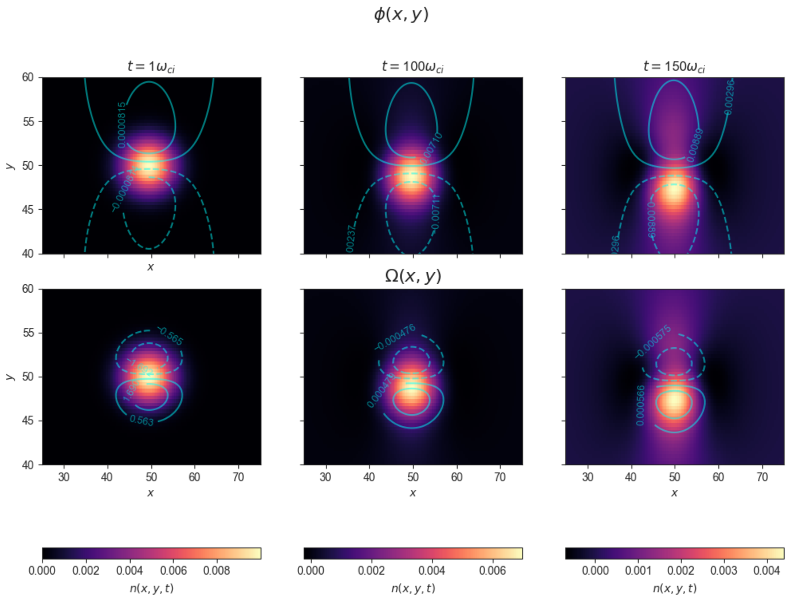

Figure 4.9: Contour plots with initial density perturbation $\Delta n/N = 0.01$. The top row shows the density along with the potential, and the density along with the vorticity on the lower row. The blob structures moves radially in the positive x-direction.

Figure 4.9 shows a blob structure with initial density perturbed amplitude $\Delta n/N = 0.01$ along with the electrostatic potential in and the vorticity curves. The blob is simulated neglecting particle loss and sheath dissipation terms. The blob is initialized as a symmetric structure, but due to the formation of the electrostatic potential and vorticity field the blob accelerates radially outwards. Due to the small potential and the constant effect of the diffusion term, the blob diffuses before the appearance of the steeping front and the trailing wake seen for larger blobs [3, 12, 13]. At the last time step we observe a large asymmetry in the blob structure, where the density appears to accumulate on the lower side of the initial blob structure. Due to the diamagnetic drift compression term in the density equation, the time evolution of the density is dependent on the spatial variation of the density in the y-direction. So in the case of small initial amplitudes, only a small variation in the derivative of the density would create the large asymmetry observed in the vertical direction. The blob are not influenced by particle loss or sheath dissipation, and thus the density are not subjected to dissipation along the magnetic field lines.

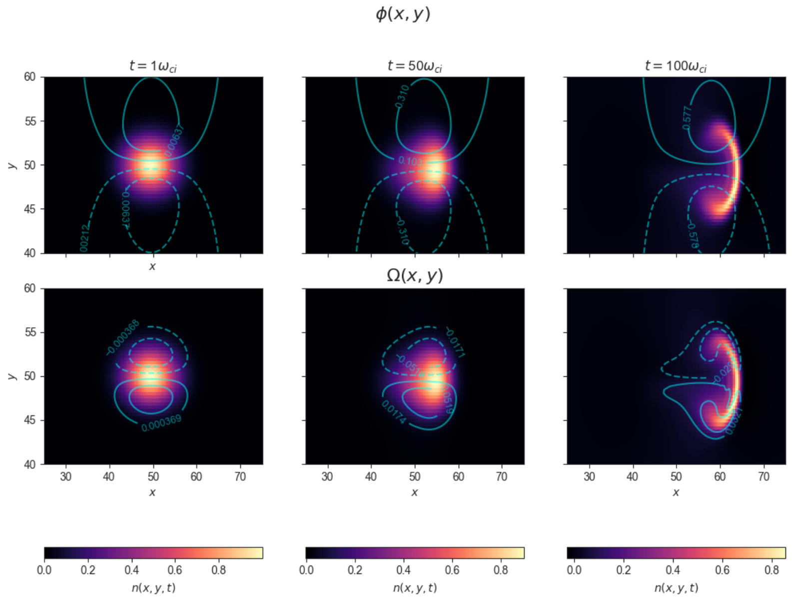

Figure 4.10: Contour plots with initial density perturbation $\Delta n/N = 1$. The top row shows the density along with the potential, and the density along with the vorticity on the lower row. The blob structures moves radially in the positive x-direction.

Figure 4.10 shows an initial symmetric blob structure with perturbed amplitude $\Delta n/N = 1$ along with the electrostatic potential and the vorticity for three different time steps. As for the previous blobs seen, due to the formation of an electrostatic potential and a vorticity field the blob accelerates radially in the positive x-direction. At the second time steps, we observe the formation of a steeping front and a trailing wake due to the interaction of the blob density with the background plasma density. The interaction creates a sheared flow pattern due to weaker force resulting in weaker flow at large values of $|y|$ [5]. The emergence of the steeping front and trailing wake are more visible in this figure compare to the figures for lower initial perturbed amplitude. The last time step in the figure, shows the emergence of the mushroom shape with lobes on either side of the steeping front which is known as Kelvin-Helmholtz vorticies and vortex shedding [2]. Due to diffusion, the amplitude are seen to decrease although that is not very visible in the figure. The diffusion are several orders of magnitude lower than the density, and will effect will take longer to be noticeable.

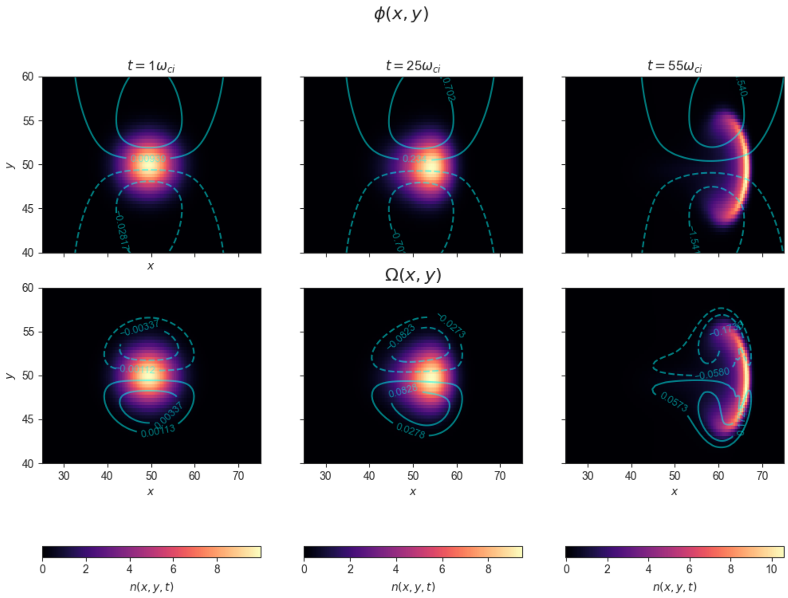

Figure 4.11: Contour plots with initial density perturbation $\Delta n/N = 10$. The top row shows the density along with the potential, and the density along with the vorticity on the lower row. The blob structures moves radially in the positive x-direction.

Figures 4.11 shows an initial symmetric structure with perturbed amplitude $\Delta n/N = 10$, along with the electrostatic potential and vorticity. The same dynamics observed in previous figures for lower initial amplitudes are observed. The structures initially accelerates due to the formation of an electrostatic potential and a vorticity field. The subsequent formation of a mushroom shape is observed in these figure, but for the larger amplitude blobs the shape seems to appear comparable to those formed from shocks; shock fronts.

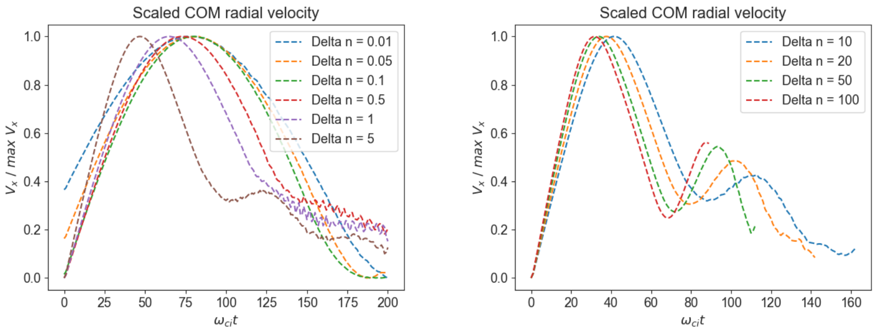

(a) The scaled center of mass radial velocity for blob structures with initial perturbed amplitude ranging from $\Delta n/N = 0.01$ to $\Delta n/N = 5$. They are scaled to be between 0 and 1, and so the difference in magnitude are not shown here.

(b) The scaled center of mass radial velocity for blob structures with initial perturbed amplitude ranging from $\Delta n/N = 10$ to $\Delta n/N = 100$. They are scaled to be between 0 and 1, and so the difference in magnitude are not shown here.

Figure 4.12: This figure shows the scaled center of mass radial velocity for different initial perturbed amplitudes.

Figure 4.12 shows the scaled radial center of mass velocity as ti evolves over time for a range of initial perturbed amplitudes from 10^{-2} to 10^{2}. Due to the axis for the velocity being scaled, the difference in magnitude are lost, but the shapes are retained. Observed from the figures, is that the acceleration phase of the blob structures with low initial amplitudes, appear longer. Observations from the figure shows that for smaller initial amplitudes, the time until the blob reaches its maximum velocity appears to be approximately equal and as a consequence the time to reach maximum radial center of mass velocity are independent of initial amplitude. This is in agreement with previous numerical simulations and studies on center of mass radial velocity as a function of initial amplitude [20]. In the case of larger perturbed amplitudes, the velocity curves are observed to be similar but time to reach maximum radial velocity are dependent on initial perturbed amplitude. Also in agreement with previous studies [19, 20].

Figure 4.13 shows the maximum radial center of mass velocity as a function of the initial perturbed amplitude in logarithmic scale. The initial amplitude spans from 10^{-2} to 10^{2}, and the dotted lines corresponds to a least squares estimate to fit a power law scaling. The span of line are the points used to estimate the coefficients using a straight line in log-log space. Also observed in the figure, are what appears to be an interesting behavior on the points corresponding to initial amplitude perturbation of 10^{-2} and 2×10^{-2} which seems not to follow the same scaling as the other points in the lower regime. They do not fit with the simulations results found in previous works [12, 19, 20], where the maximum radial velocity points appear to follow the same line scaling as the rest. However, the points in this case appears to have higher maximum velocities than in the previous publications, leading to the possibility that they must be outliers. By considering the figure showing the radial velocity over time, the possibility of finding a local maximum or a maximum for which the function are nonphysical, seems not to explain the behavior of the outliers. Another possible explanation of the outliers, can be the computations of the center of mass velocity. Since the methods using to estimate the blob structure, center of mass position and velocity relies on utilizing numerical approximations. Then there is a possibility that due to the low initial density, the numerical error due to either truncation or approximation are to large. And as a consequence, describing the center of mass diagnostics for these points are not feasible with the used estimates. And thus the points should be disregarded in the determining the scaling in the lower regime.

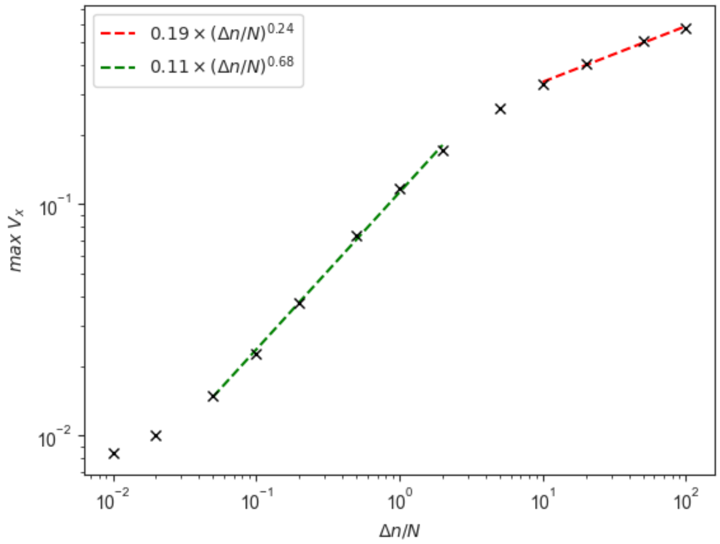

Figure 4.13: Shows the maximum radial velocity for each of the different structures with initial perturbed amplitude ranging from 10^{-2} to 10^{2}. The axis are in logarithmic from, and a least square estimate for scaling laws are shown as dotted lines.

Sheath dissipation and particle loss terms retained

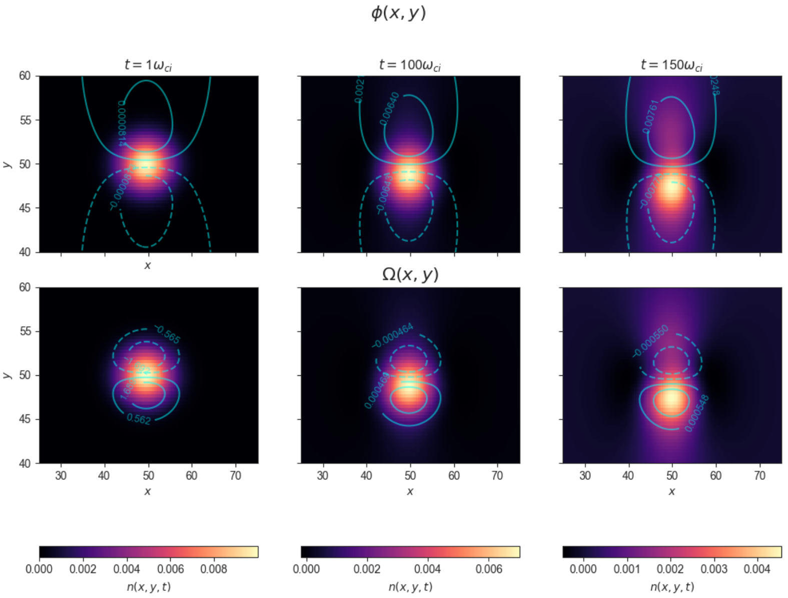

Figure 4.14: Contour plots with initial density perturbation $\Delta n/N = 0.01$. The top row shows the density along with the potential, and the density along with the vorticity on the lower row. The density is shown as colored contours, and the potential and vorticity is shown as blue curves where dotted lines corresponds to negative values and lines correspond to positive values. The blob structures moves radially in the positive x-direction. Blob influenced by sheath dissipation.

Figures 4.14 - 4.15 shows initial symmetric blob structures subjected to particle loss and sheath dissipation with initial perturbed amplitudes from along with the electrostatic potential and vorticity for three time steps. The density is shown as colored contour, the potential at the top row as blue curves and the vorticity as blue curves on the bottom row. The dotted lines corresponds to negative values and lines corresponds to positive values. In the previous subsection, figures showing the same span of initial amplitudes but the simulations where run without the addition of sheath dissipation terms. Comparing, we see the same dynamics for both cases. The formation of a electrostatic potential and vorticity field, accelerates the blob radially outwards. Further we observe the creation of a steeping front and trailing wake, and finally the mushroom shape. We also observe the appearance of the lobes on either side of the blob structures with opposite polarity in the vorticity. In the low initial amplitude

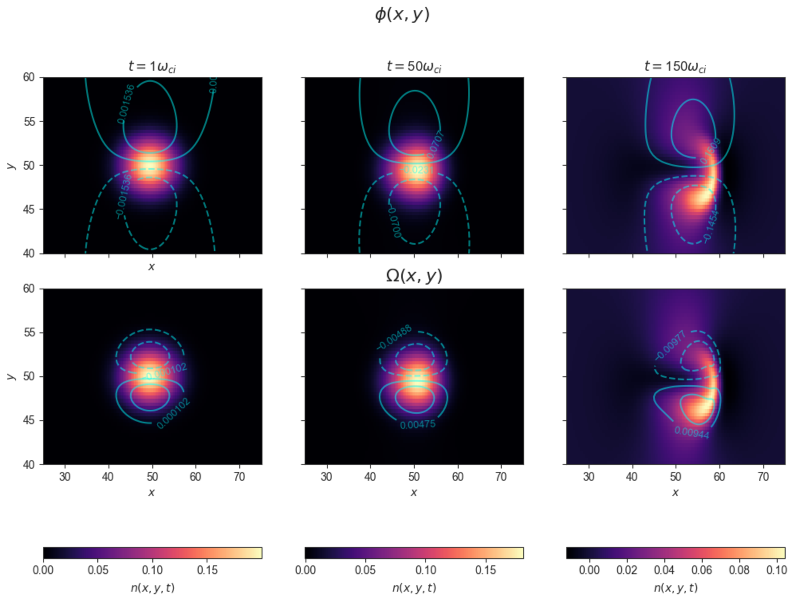

Figure 4.15: Contour plots with initial density perturbation $\Delta n/N = 0.2$. The top row shows the density along with the potential, and the density along with the vorticity on the lower row. The blob structures moves radially in the positive x-direction. Blob influenced by sheath dissipation.

figure, we observe again observe the asymmetric behavior due to the inclusion of diamagnetic drift compression in the density equation. For the lower initial amplitudes, the diffusion and dissipation leads to a sharp decrease in density amplitude. Leading to restricted motion observed in the figures. However, due to the particle loss and sheath dissipation terms, the density dissipates at a higher rate compared to the case with no sheath dissipation and no particle loss.

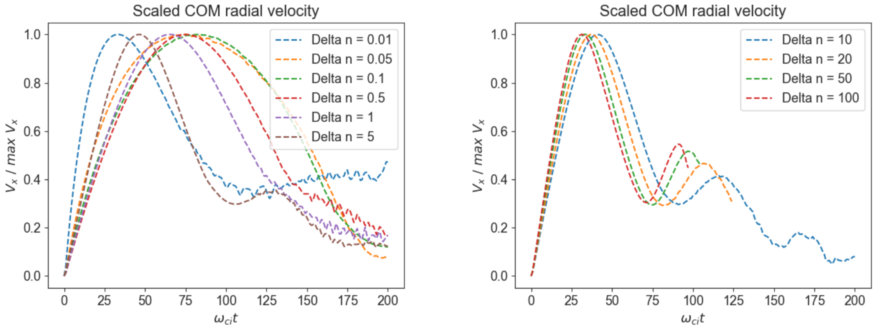

(a) Scaled center of mass velocity for blob structures with initial perturbed amplitude ranging from $\Delta n/N = 0.01$ to $\Delta n/N = 5$. Blobs subjected to sheath dissipation.

(b) Scaled center of mass velocity for blob structures with initial perturbed amplitude ranging from $\Delta n/N = 10$ to $\Delta n/N = 100$. Blobs subjected to sheath dissipation.

Figure 4.16: Scaled center of mass velocity for blobs subjected to sheath dissipation

Figure 4.16 shows the center of mass velocity for a range of different initial perturbed amplitudes for blob structures subjected to particle loss and sheath dissipation. It shows that in limit of larger initial perturbed amplitudes. the radial center of mass velocity remains seemingly unchanged. In the case for the lower initial amplitudes, we observe a big change in terms of the shape and accelerations phase. For the lowest initial amplitude, it quickly rises to maximum values meaning it accelerates quickly in the initial phase. Before the diffusion and dissipation decrease the amplitude and the blob decelerates to a much lower value. For larger amplitude blobs, the inertial term takes over and the acceleration becomes slower, until we observe somewhat the same as we did in the case of no sheath dissipation.

Figure 4.17 shows the maximum radial center of mass velocity as a function of the initial perturbed amplitude for the blob structures subjected to particle loss and sheath dissipation. The axis are given in logarithmic scale, and the dotted line again corresponds to the least squares estimate the parameter for scaling laws. In the region of small initial amplitudes, the values follows a quite steep line with a rate of increase ≈ 1. Before there is a transition region over to a more flat increase for the remaining points. As we observer, in the region of larger initial amplitudes the scaling transition to the same as for the case when sheath dissipation was neglected.

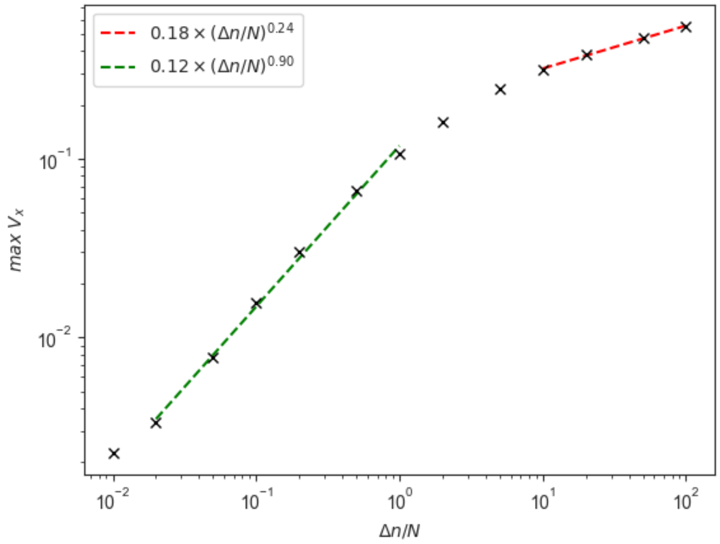

Figure 4.17: Maximum radial velocity for initial perturbed amplitude ranging from 10^{-2} to 10^{2}. Blob structures subjected to sheath dissipation and the axis are given in logarithmic scale. Dotted lines are the least squares estimate for power scaling laws.

4.3.2 Discussion

Comparing the maximum velocity as function of the initial perturbed amplitude $\Delta n/N$ in the case of no sheath dissipation and no particle loss terms shown in figure 4.13 and in the case of retaining the sheath dissipation $\sigma_{\grave{o}mega}$ and particle loss σ_n terms shown in figure 4.17, both predicts similar scaling for the largest initial amplitudes. In this region, the simulations results predicts that radial COM velocity scales as $V_x \sim (\Delta n/N)^{0.24}$. From previous publications and results, for larger perturbed amplitude the radial velocity becomes independent of the initial amplitude[19, 21]. Further for smaller amplitudes in the case of no sheath dissipation and no particle loss, the radial COM velocity scales as $V_x \sim (\Delta n/N)^{1/2}$ and retaining sheath dissipation gives the sheath dissipative regime for which the radial COM velocity scales as $V_x \sim \Delta n/N$. The results obtained in here are $V_x \sim (\Delta n/N)^{0.90}$, which differ slightly from the previous values obtained for the scaling. However, in the large amplitude scaling region, the effect of parallel currents becomes very small compared to the perturbation of the blob density and the sheath dissipation term and the particle loss term are only a small correction to to a quantity which are orders of magnitude larger, which leads to the same scaling factor in the larger region. Since there is a region of transition between the scaling in the lower amplitudes and the independent region. A possible explanation for the lower observed value for the scaling, is that the points used for the lease squares estimates are located in the transition between the lower scaling and the independent region. In previous publications neglects the effect of particle loss, which could effect the motion of the blob structures in the lower amplitude region. This can explain the difference obtain in the results for the sheath dissipation scaling regime.

From the figure showing the radial COM velocity scaling for neglected sheath dissipation, figure 4.13, we obtained that COM radial velocity scales as $V_x \sim (\Delta n/N)^{0.68}$. From the least squares estimate process, it became clear that the number of used points greatly effects the value of the scaling factor, and on point added was in some cases enough to alter the value of factor of almost 0.1. So there is a high uncertainty in the value of the scaling factor. This can be a possible cause in the difference in the observed scaling factor of 0.68 and the scaling factor obtained from a order of magnitude approach combined with simulations results in previous publications [11, 12, 19, 21].

4.4 Particle Loss

Previous works into the effect of the sheath dissipation on the radial center of mass velocity of filament structures, focuses on the vorticity equation. More specifically the non-dimensional sheath dissipation parameter σ_Ω, while the effect due to particle loss parameter σ_n are neglected [12, 19]. Implementing the particle loss term in the density equation is not the easiest thing to consider, due to the exponential decaying effect this term has on the background density. This will be discussed in more detail in subsection 4.4.1, where a possible solution will be described. However, these solutions have limitations and another possible approach will be mentioned in the summary of this thesis.

The thesis will focus on the effects of σ_n and further neglect the contributions from the sheath dissipation term σ_Ω. The reason for the interest in σ_n, comes from results obtained from stochastic modeling of filaments as density pulses recorded at a fixed probe over time [23].

By considering super-position of K uncorrelated pulses which moves radially along the x-axis described by [21–23]

$$\Phi_K(x,t) = \sum_{k=1}^{K} \phi_k(x, t - s_{0k}) \tag{4.15}$$

Pulse $\phi(x, t - s_{0k})$ is located at a reference point $x = 0$ at arrival time s_{0k}. The time evolution of each single pulse is assumed to follow [21–23]

$$\frac{\partial \phi}{\partial t} + V\frac{\partial \phi}{\partial x} + \sigma_n \phi = 0 \tag{4.16}$$

where the subscription are dropped for readability. V denotes the pulse velocity and σ_n a constant linear damping due to the sheath dissipation parameter in the density equation. The radial position of a pulse at any time t can be described through [23]

$$X(t) = \int_0^t dt'\, V(t') \tag{4.17}$$

The velocity can be considered to be time dependent, given by a power law dependent of the instantaneous pulse amplitude [23]

$$\frac{V(t)}{\langle v_0 \rangle} = c_v \left(\frac{A(t)}{\langle a_0 \rangle} \right)^{\alpha} \tag{4.18}$$

where $\langle a_0 \rangle$ is the average of the initial random variable of the amplitude at the reference point $x = 0$, $a_0 = A(0)$ initial amplitude and $\langle v_0 \rangle$ is the average velocity at the reference point, $v_0 = V(0)$ velocity random variable at the reference point [23]. c_v are the proportionality coefficients. $\alpha \longrightarrow 0$ describes radial velocity independent of the pulse amplitude and $\alpha = 1$ describes a linear relationship between the quantities [23]. When there is a dependence on the radial velocity of the instantaneous pulse amplitude and utilizing equation 4.17, integration gives the pulse radial position as a function of time [23]

$$X(t) = X_{\text{max}} \left[1 - \exp\left(-\alpha \sigma_n t \right) \right] \tag{4.19}$$

where the maximum radial position are defined as [23]

$$X_{\text{max}} = \frac{c_v \langle v_0 \rangle}{\sigma_n \alpha} \tag{4.20}$$

In the limit of $\sigma_n t \longrightarrow \infty$, the radial position $X(t) \longrightarrow X_{\text{max}}$. So as time evolves the pulse radial position will approach the maximum radial position and stagnates at X_{max}, while the pulse amplitude exponentially decays as the pulse moves closer to this position [23]. This predicted pulse or blob stagnation, are the main motivation for examining the effect from the σ_n term on the blob dynamics in numerical simulations.

The model equations used for simulations in this section retaining the Boussinesq approximation, are given by

$$\frac{\partial n}{\partial t} + \{\phi, n\} - gn\frac{\partial \phi}{\partial y} + g\frac{\partial n}{\partial y} = D_n \nabla_\perp^2 \phi - \sigma_n n \exp\left(-\phi \right) \tag{4.21}$$

$$\frac{\partial \Omega}{\partial t} + \{\phi, \Omega\} + \frac{g}{n}\frac{\partial n}{\partial y} = D_\Omega \nabla_\perp^2 \Omega \tag{4.22}$$

where sheath dissipation $\sigma_\Omega = 0$ and will so for all simulations done in this section. Further $g = 0.01$, $l = 6$, $D_n = D_\Omega = 10^{-4}$, and the blob is initialized using a symmetric Gaussian blob with initial amplitude $\Delta n/N = 0.1, 1, 2$. Background density set to $N = 1$, potential and vorticity initialized as zero.

4.4.1 Exponential decay in the background

When considering model equations retaining the effect of particle loss σ_n in the density equation, it has some unkind affects on the background density which needs to be addressed before simulations on the parameter scan in the particle loss term. Only considering the background density N when there is no blob structure present in the simulation, inserted into the density equation specified in equation 4.21, neglecting all other terms except for the particle loss term yields

$$\frac{\partial N}{\partial t} = -\sigma_n N \exp(-\phi) \tag{4.23}$$

where the right hand side can be linearized $\exp(-\phi) \approx 1$ and is straight forward to solve. Solving gives

$$N(t) = N_0 \exp(-\sigma_n t) \tag{4.24}$$

and so clearly, to the lowest order the particle loss term gives exponential decay in the background density. This is an unfortunate effect leading to problems when we want to study the evolution of blob structures. The code has been updated with a added term in order to mitigate this effect, however this is not used in these simulations. This is because that computation does not work when changing the particle loss parameter σ_n, and when the parameter is of the order 10^{-2} the simulations appears to break down.

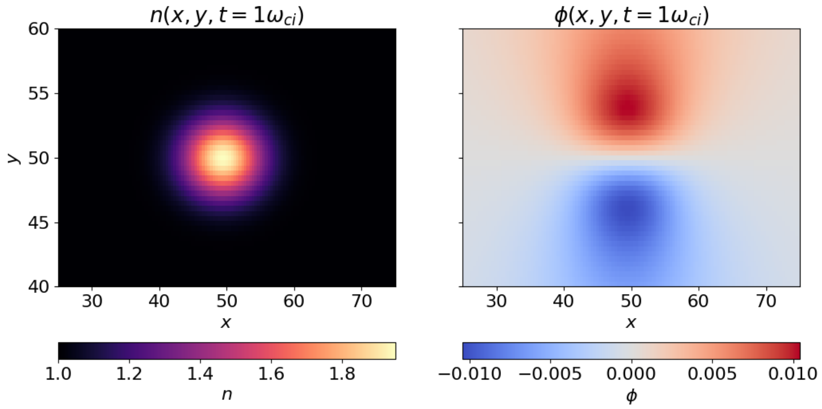

Figure 4.18: Contour plots for the density on the left and the potential for the blob structure at right side. In order for the potential to be non-zero, one unit of time has elapsed. Both plots shows a isolated blob structure, and a small electrostatic potential.

Figure 4.18 shows a symmetric blob structure with initial perturbed amplitude $\Delta n/N = 1$ simulated using the model equations shown in equation 4.21 and 4.22 with a particle loss parameter $\sigma_n = 0.05$. The left plot in the figure shows the density and the associated potential is shown on the right, and there appears to be a normal simulation. Figure 4.19 show the same simulation of an initially symmetric blob structure after 200 time steps. Clearly this is not right, and needs to be addressed. From the figure we observe a wave-like pattern which has emerged in the density and in the potential, which creates an interesting behavior.

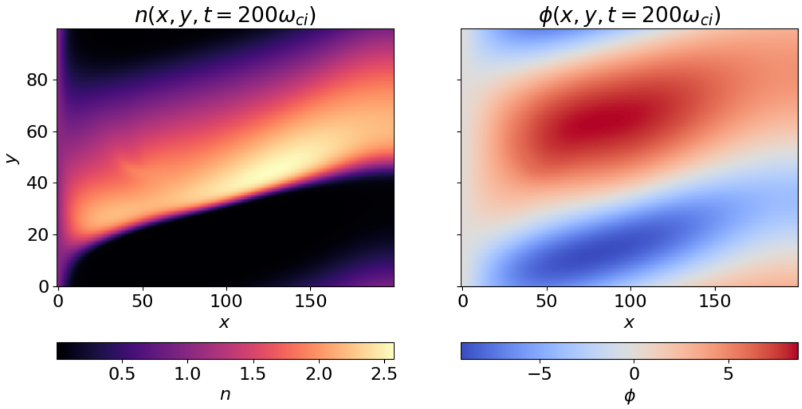

Figure 4.19: Contour plots for the density on the left and the potential for the blob structure at right side. The density and potential are shown for 200 elapsed time steps. The non-physicality are shown in both plots, and a wave-like behavior emerges in both the density and the potential.

To try to give an explanation of this somewhat peculiar and nonphysical behavior, we must focus on the method implemented to mitigate the exponential decay in the background density. The idea behind the implemented method, is to add back the same amount that was subtracted due to decay in the background density N. By defining a constant potential $\phi_{\mathrm{bg}} = 0$, and computing the particle loss decay in the background density by given by $\sigma_n N \exp(-\phi_{\mathrm{bg}})$ and add this back to the total density n. But the model equations are coupled through the particle loss term in the density equation and the partial derivative of n term in the vorticity equation. So the evolution of the density and the potential effect each other, and creates a coupling between them. The particle loss term can be linearized using a Taylor expansion of the exponential function, which gives

$$\frac{\partial N}{\partial t} \sim \sigma_n N(1 - \phi) \tag{4.25}$$

and shows that N is now proportional to the potential ϕ. Since the background potential $\phi_{bg} = 0$, we add back $\sigma_n N$ to the background density which implies canceling the first term in 4.25, leaving

$$\frac{\partial N}{\partial t} \sim \sigma_n N\phi \tag{4.26}$$

which implies a linear coupling to ϕ. If there is a difference in ϕ and ϕ_{bg} due to numerical approximations and errors, the expression does not decay to zero value. It becomes negative and due to the partial derivative term in the vorticity equation, the density again influences the potential. Does a runaway effect happens, where it appears that the potential and the background density becomes essentially the same quantity. And the resulting effect, are the wave-like pattern both in the background density and the potential, shown in figure 4.19. To remove the unwanted nonphysical effect, a modification to the discussed approach is to use the potential ϕ and not the constant value ϕ_{bg} which should cancel out the difference causing the decaying effect of the background density N. This is the implementation used to simulate the blobs with initial perturbed amplitude $\Delta n/N = 1$ and $\Delta n/N = 2$ in this section.

However, although the implementation used above appears to work well in the two mentioned cases. When we consider $\Delta n/N = 0.1$, then again some interesting behavior emerges. Lets for now use the approach mentioned above to consider simulations of model equations 4.21 and 4.22 with $\Delta n/N = 0.1$. Figure 4.20 shows the computed center of mass radial position and velocity for the simulated blob structure with particle loss parameter $\sigma_n = 0.01, 0.02, 0.05$ respectively. Figure 4.21 shows the maximum radial velocity as a function of particle loss parameter for values of the parameter ranging from 10^{-4} to 0.05. We can observe that the maximum radial COM velocity starts to decrease of larger particle loss terms, but for some reason appears to increase after a particle loss parameter of $\sigma_n = 0.01$ and becomes much a larger value for $\sigma_n = 0.05$. This is clearly visible in the figure showing the radial velocity, where for $\sigma_n = 0.05$ the acceleration of the blob appears to increases in after about 25 time steps peaking at almost twice the maximal radial velocities for $\sigma_n = 0.01, 0.02$ respectively. Thus we must conclude that the implemented method for mitigate the decaying effect on the background density has its limitations and at this point one could speculate on what causes this nonphysical behavior in results. One explanation could be instabilities due to higher order terms in the Taylor expansion of the exponential function combined with numerical error. But this is speculation of the author, and should be a topic for further analysis.

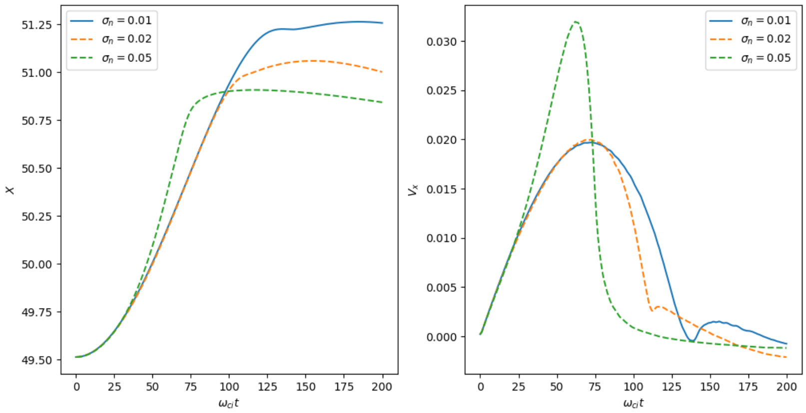

Figure 4.20: Radial COM diagnostics for $\sigma_n = 0.01, 0.02, 0.05$ showing the nonphysical effects for the larger σ_n values. Initial amplitude is $\Delta n/N = 0.1$.

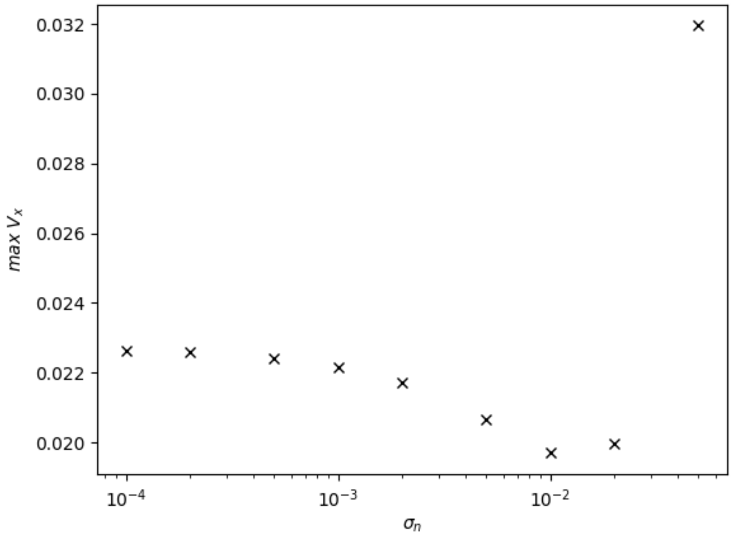

Figure 4.21: Maximum radial COM velocity as a function of σ_n for $\Delta n/N = 0.1$. Shows the nonphysical behavior for larger σ_n values.

Since the method implemented for $\Delta n/N = 1$ and $\Delta n/N = 2$ appears to yield problems when simulated for lower initial amplitudes, then we will introduce a simplified model. This will only be used in the case when $\Delta n/N = 0.1$, for the two other cases when $\Delta n/N = 1, 2$ respectively we will use the model equations 4.21 and 4.22.

New model for small amplitudes

When considering small blob perturbed amplitudes, we can make the assumption that the formed electrostatic potential $\phi \ll 1$. Under that assumption, the exponential term appearing in the particle loss term in equation 4.21 can be approximated using a Taylor expansion. Using the first term in the expansion, simplifies $\exp(-\phi) \approx 1$. To consider the blob, and not the background density, the density in the particle loss term can be written as $n - n_{bg} = n - 1$. Here the constant value of the background density has been used. Combining the approximated terms with the particle loss parameter, gives $\sigma_n(n-1)$ as the simplified particle loss term in the model equations. Further simplifications can be made by neglecting the diamagnetic compression drift and the electric compression drift terms in the particle density equation. Thus the simplified model takes the form

$$\frac{\partial n}{\partial t} + \{\phi, n\} = D_n \nabla_\perp^2 n - \sigma_n (n-1) \tag{4.27}$$

$$\frac{\partial \Omega}{\partial t} + \{\phi, \Omega\} + \frac{g}{n}\frac{\partial n}{\partial y} = D_\Omega \nabla_\perp^2 \Omega \tag{4.28}$$

The parameters will remain unchanged from the previous model, only the equations made to simulate the blobs are changed when considering $\Delta n/N = 0.1$.

4.4.2 Simulations Results

The subsection contains the results from the parameter scan in the particle loss parameter σ_n, while the sheath dissipation parameter is set to $\sigma_\Omega = 0$ for all simulations.

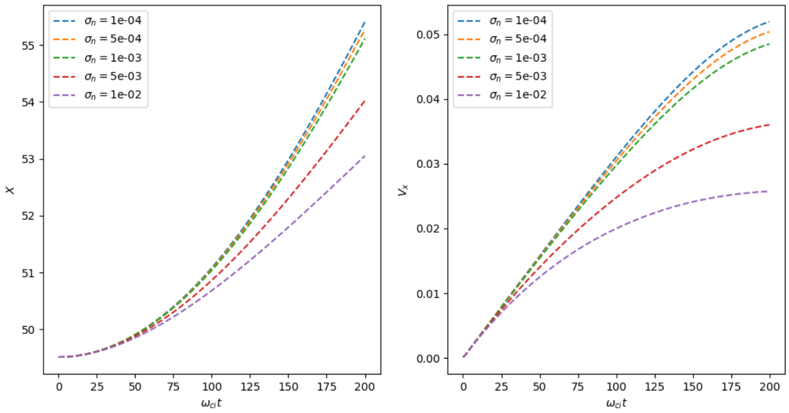

Figure 4.22: Shows the center of mass radial diagnostics for blobs with $\Delta n/N = 0.1$ with varying σ_n parameter from 10^{-4} to 0.01. Position is shown to the left and velocity is shown on the right.

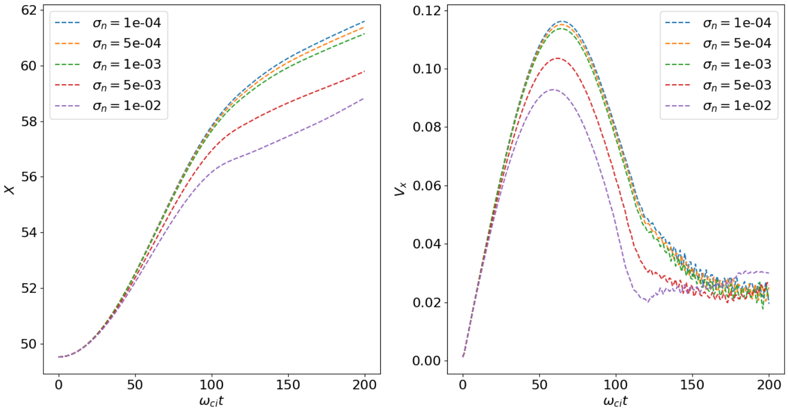

Figure 4.23: Shows the center of mass radial diagnostics for blobs with $\Delta n/N = 1$ with varying σ_n parameter from 10^{-4} to 0.01. Position is shown to the left and velocity is shown on the right.

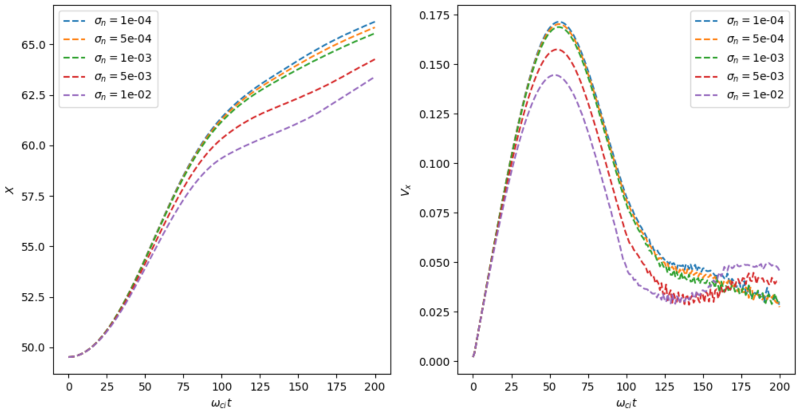

Figure 4.24: Shows the center of mass radial diagnostics for blobs with $\Delta n/N = 2$ with varying σ_n parameter from 10^{-4} to 0.01. Position is shown to the left and velocity is shown on the right.

Figures 4.22, 4.23 and 4.24 shows the radial center of mass position and velocity for a blob with initial amplitude $\Delta n/N = 0.1, 1, 2$ respectively, for σ_n-values ranging from 10^{-4} to 0.01. For $\Delta n/N = 1, 2$, the blobs have been simulated using the Boussinesq approximated model equations 4.21 and 4.22. And for $\Delta n/N = 0.1$, the blobs have been simulated using hte Boussinesq approximated model equations 4.27 and 4.28. The blobs is initially at rest before the formation of electrostatic potential and a vorticity field accelerates the blobs radially outwards. The blob with smaller σ_n-values is observed to have a longer acceleration phases and appear to have a higher COM radial velocity. In the case of perturbed amplitude $\Delta n/N = 1$ and $\Delta n/N = 2$, the velocity curves has distinct peaks before they decelerate down to a low value as the blob structures dissipates due to dissipation and diffusion.

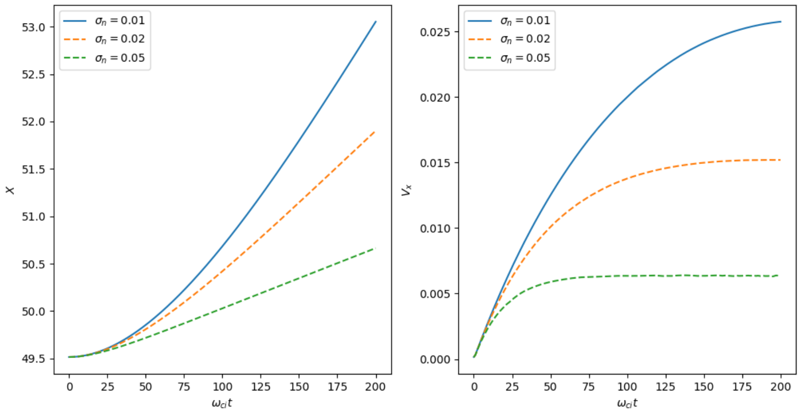

Figure 4.25: Shows the center of mass radial diagnostics for blobs with $\Delta n/N = 0.1$ with varying σ_n parameter from 0.01 to 0.05. Position is shown to the left and velocity is shown on the right.

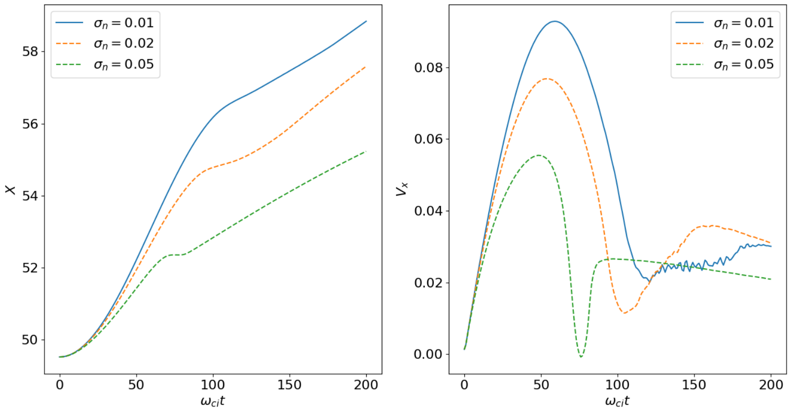

Figure 4.26: Shows the center of mass radial diagnostics for blobs with $\Delta n/N = 1$ with varying σ_n parameter from 0.01 to 0.05. Position is shown to the left and velocity is shown on the right.

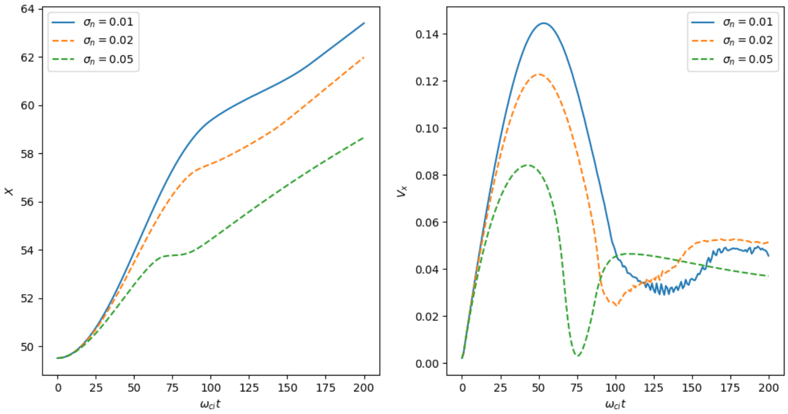

Figure 4.27: Shows the center of mass radial diagnostics for blobs with $\Delta n/N = 2$ with varying σ_n parameter from 0.01 to 0.05. Position is shown to the left and velocity is shown on the right.

Figures 4.25, 4.26 and 4.27 shows the radial COM position and velocity as the blob structures evolves over time for $\Delta n/N = 0.1, 1, 2$ respectively, with σ_n-values from 0.01 to 0.05. For the case of $\Delta n/N = 1$ and $\Delta n/N = 1$ the velocity curves accelerates before they reach a peak velocity, and further the velocity decreases. The blobs velocity is observed to decrease with increasing σ_n-values. Observed from the largest value of σ_n in the case of initial perturbed amplitude of 0.1, is that the velocity curves appears to reach a constant value as the blob travels with constant velocity radially outward. For the two other cases, they seems to have a small decrease after $100\omega_{ci}$ but appears to have some of the same dynamics as in the lower amplitude case. The figure showing the computed center of mass diagnostics for $\Delta n/N = 0.1$ only contains data for 200 time steps, and thus do not show the peak in the same way as for the two other cases. These simulations was only run for 200 time steps, but should be verified further for confirmation of the maximum radial values. However, they show the same trend as observed for the two other initial perturbed amplitudes.

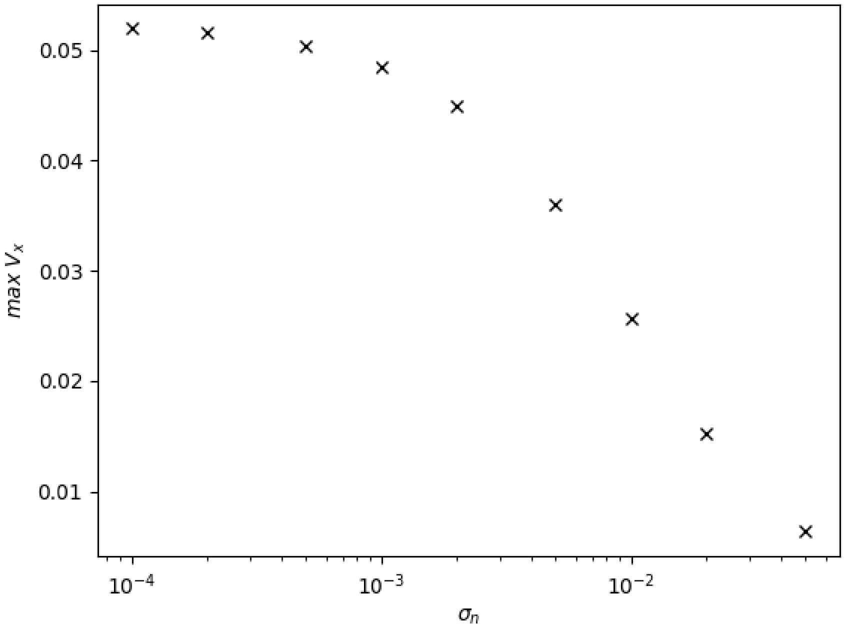

Figure 4.28: Maximum center of mass radial velocity are shown as a function of σ_n for blobs with $\Delta n/N = 0.1$. The σ_n-axis are shown in logarithmic scale and the maximum V_x-axis are shown in linear scale.

Figure 4.28 shows the computed maximum radial COM velocity as a function of the particle loss parameter σ_n. Theσ_n-axis are show in a logarithmic scale and the maximum radial velocity axis is shown in linear scale. In the region of lower particle loss parameters, the maximum velocity appears to only slightly decrease with increasing parameter value. At approximately $\sigma_n \approx 10^{-3}$ we observe a transition region where the maximum radial COM velocity is seen to decrease with increasing particle loss parameter value. After a short transition region, the maximum velocity has a sharp decrease with increasing parameter value.

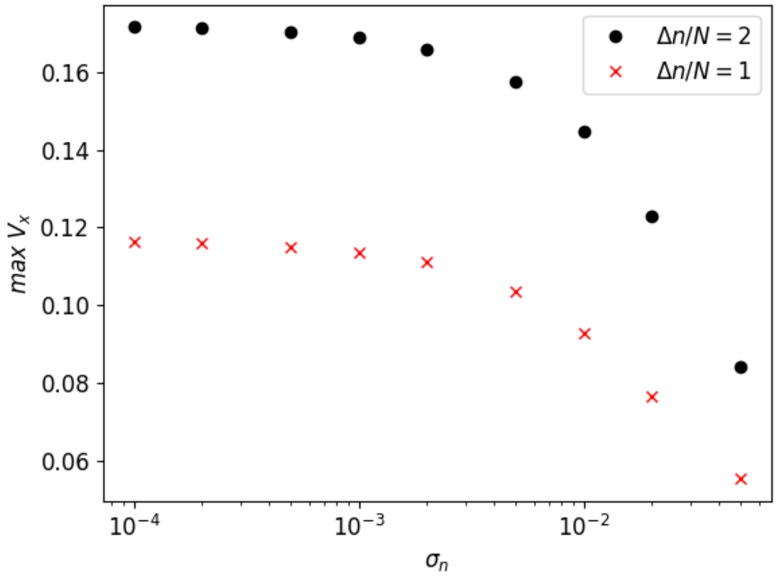

Figure 4.29: Shows a maximum radial COM velocity as a function of the particle loss parameter σ_n for blobs with $\Delta n/N = 1$ shown as red crosses and $\Delta n/N = 2$ shown as black dots. σ_n-axis are shown in logarithmic scale and the maximum radial COM velocity are shown in linear scale.

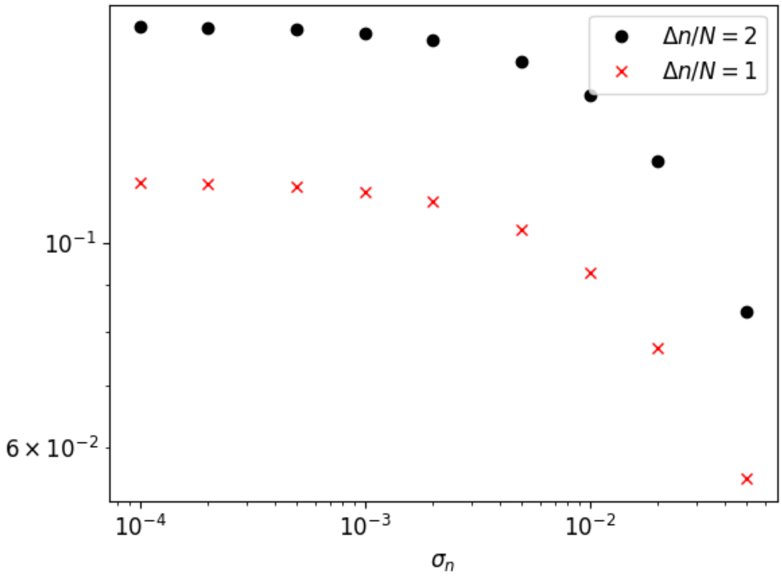

Figure 4.30: Shows a maximum radial COM velocity as a function of the particle loss parameter σ_n for blobs with $\Delta n/N = 1$ shown as red crosses and $\Delta n/N = 2$ shown as black dots. Both axis are shown in logarithmic scale.

Figure 4.29 show the maximum radial COM velocity for initial amplitudes $\Delta n/N = 1, 2$ respectively. Black dots corresponds to blob structure with $\Delta n/N = 2$ and the red crosses show the blob structure with $\Delta n/N = 1$. The maximum velocity axis is given in linear scale and the particle loss parameter axis is given in logarithmic scale. In the lower particle loss parameter region, radial COM velocity for both blobs appears to follow a almost straight line with a small decrease in maximum velocity with increasing particle loss parameter. We can also observe a transition region where maximum velocity for both blobs appears to decrease at an increasing rate with a small change in particle loss parameter, before they transition to a large decrease with increasing σ_n. But the decrease in maximum velocity appears to be greatest for the blob structure with initial perturbed amplitude $\Delta n/N = 2$. Figure 4.30 show the same situation but here the both axis are given in logarithmic scale. In the lower particle parameter region, it appears that both for $\Delta n/N = 1$ and $\Delta n/N = 2$ the maximum radial velocity is independent of the particle loss parameter. When $\sigma_n \approx 10^{-2}$, we have a transition region where the maximum radial velocity has a small decrease with increasing σ_n, before they appear to transition into a region where the maximum radial velocities follows a line down.

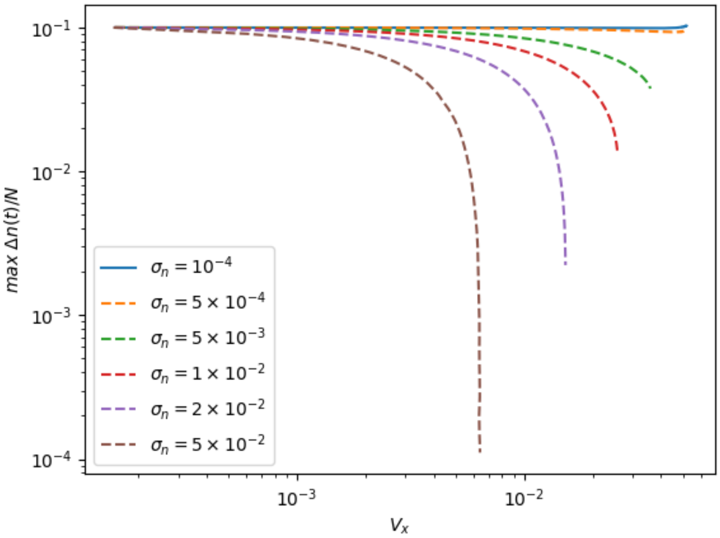

Figure 4.31: Maximum instantaneous density amplitude as a function of radial COM velocity for several σ_n-values. Both axis are shown in logarithmic scale. Initial density of blobs $\Delta n/N = 0.1$.

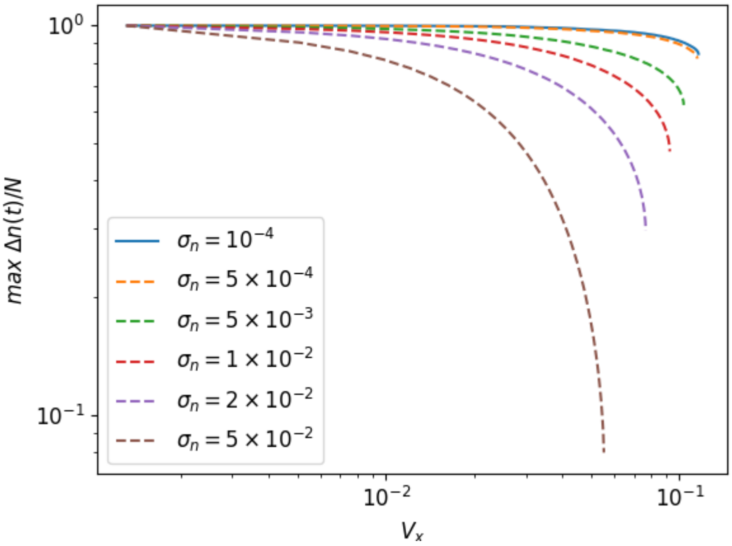

Figure 4.32: Maximum instantaneous density amplitude as a function of radial COM velocity for several σ_n-values. Both axis are shown in logarithmic scale. Initial density of blobs $\Delta n/N = 1$.

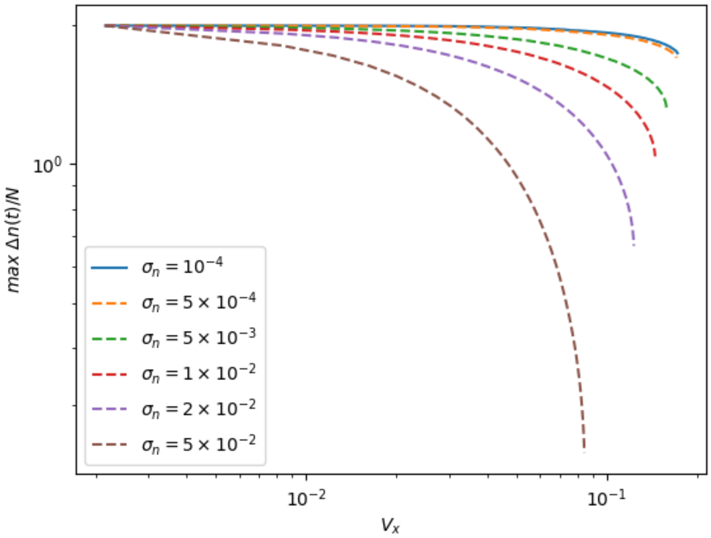

Figure 4.33: Maximum instantaneous density amplitude as a function of radial COM velocity for several σ_n-values. Both axis are shown in logarithmic scale. Initial density of blobs $\Delta n/N = 2$.

Figures 4.31, 4.32, 4.33 shows the maximum instantaneous amplitude as a function of the blobs radial COM velocity for $\Delta n/N = 0.1, 1, 2$ respectively. In the case when $\sigma_n \lesssim 10^{-3}$, the lines are approximately linear in the logarithmic sense indicating that the blobs retain most of their density with increasing radial COM velocity. For the blobs with $\sigma_n > 10^{-3}$, the lines starts to curve with increasing velocity. The curvature of the lines are observed to increase with increasing particle loss parameter, and the start of the curving appears to be dependent on the particle loss parameter. When the blobs accelerates, they seems to retain most of their density for the lower velocities. But as the radial velocity increases, we observe that the maximum density amplitude decreases with an increasing rate towards the maximum radial velocity. For $\sigma_n = 0.05$, the blobs is observed to dissipate density at a significant rate in the region of lower radial COM velocities. The rate of dissipation is observed to increase concurrently with the increase in radial velocity. As the blob approaches the maximum radial velocity, the rate of decreasing maximum density amplitude increases until the blobs reaches the maximum radial velocity where the density amplitude are seen to decrease at a very high rate.

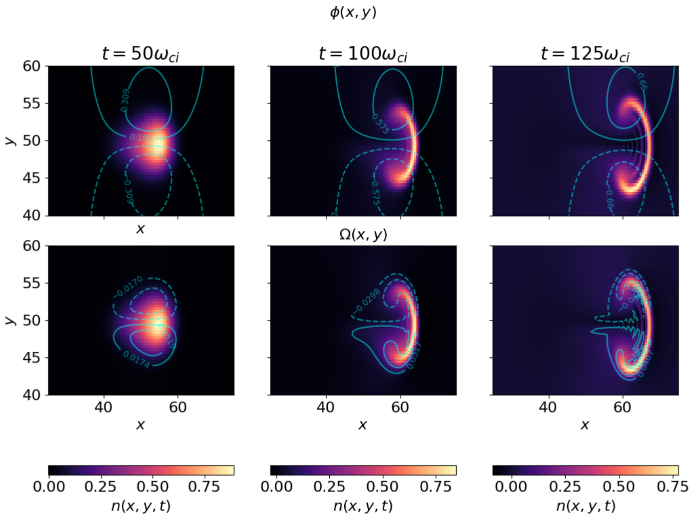

Figure 4.34: Contour plot showing the density, potential and vorticity curves for $\Delta n/N = 1$ blob structure with $\sigma_n = 1 \times 10^{-4}$. The blob are shown for three different time steps.

Figure 4.34 shows the density as colored contour, while electrostatic potential and vorticity are given as blue contour curves for a blob structure with initial perturbed amplitude $\Delta n/N = 1$ and particle loss parameter $\sigma_n = 10^{-4}$. The top row shows the electrostatic potential along with the density and the bottom row shows the vorticity curves along with the density. Here we observe the induced radial motion due to the electrostatic potential and the vorticity field, and the formation of leading steeping front and trailing wake due to interactions between the blob density and the background density.We also observe the formation of the previously seen mushroom shape and the formation of side lobes with opposite polarity of the vorticity.

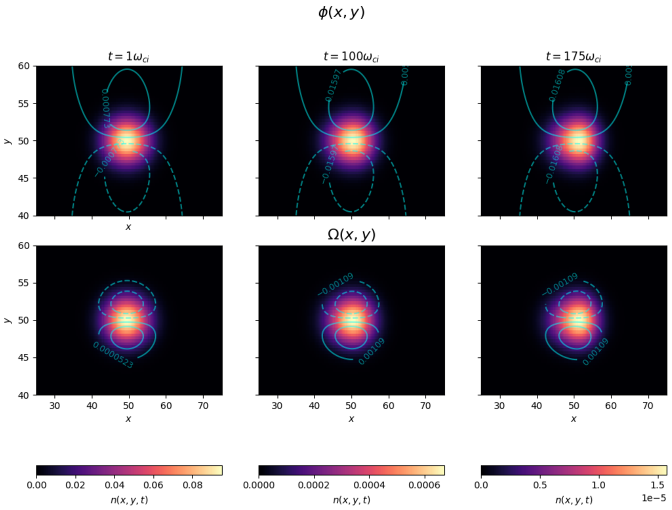

Figure 4.35: Contour plot showing the density, potential and vorticity curves for $\Delta n/N = 0.1$ blob structure with $\sigma_n = 0.05$. The blob are shown for three different time steps

Figure 4.35 shows the density as colored contours, the electrostatic potential and the vorticity for a blob with initial perturbed amplitude $\Delta n/N = 0.1$ and particle loss parameter $\sigma_n = 0.05$. The potential is shown as blue lines on the top row and the vorticity are show on the bottom row as blue lines. The dotted lines corresponds to negative values and the lines corresponds to positive values of the quantity. The initially symmetric shape is observed to retain as the blob is accelerated radially, although the distance traveled by the blob appears to be very small in comparison with previous results for lower particle loss parameter.

4.4.3 Discussion

The results showing the radial COM velocity of the blobs as it evolves over time and the figures showing the maximum radial velocity for the various particle loss parameters shows a decreasing maximum radial velocity with increasing sheath dissipation. This is in agreement with prediction using stochastic modeling, showing in the limit of large $\sigma_n t$ the blobs stagnate [23]. In the case of the larger particle loss parameter region, it appears as if the maximum radial COM velocity follows some form of scaling law which appears to also be dependent on the initial amplitude. In both cases as we increased the particle loss parameter, we observe the points from the maximum radial appears to follow a line in loglog space. The followed line appears to be different for the initial perturbed amplitudes. From the figures showing the maximum instantaneous amplitude, it shows that the for the lower particle loss parameter the maximal amplitude decreases slow or not at all. Indicating little change in the amplitude over the motion, and the radial velocity appears undetermined by the instantaneous amplitude or only weakly dependent. For larger values of the particle loss parameter, the blobs appears to dissipate density at a higher rate as they reach the maximum velocity. This effect is very visible in the case of $\sigma_n = 0.05$.

For $\Delta n/N = 0.1$ where the simplified model was utilized, in the case of $\sigma_n = 0.05$ the results shows a blob structure that accelerates rapidly to maximum velocity and retains the same velocity while it dissipates density at a high rate. The blob is also observed to retain its symmetric shape and we do not see a distinct steeping front and trailing wake. These results are the same as found in ref. [19], where the effect of the sheath dissipation was investigated. We show here the same behavior for the particle loss parameter, as for the sheath dissipation parameter. This result indicates that by utilizing the simplified model, σ_n appears to yield the same results as σ_Ω which is an interesting result and requires further research to verify the behavior.

The simplified model used for simulating $\Delta n/N = 0.1$ seems to give good results in this case, but the validity of the model and the simplifications used have not been considered. In order to gain insight into the models limitations and predictions, further studies must be completed with varying initial amplitude.

An approach which could have been utilized in order to mitigate the exponential decay in the background density, is to linearize the particle loss term. Utilizing this approach would leave the original code unchanged, and the problematic nonphysical behavior will then not be a problem. This approach will work well for all initial amplitudes, and could be used to verify the results obtained in this thesis.

4.5 Non-Boussinesq

Many previous works simplifies the complex dynamics of the vorticity equation by neglecting the added inertial term due to the density gradient, this is the Boussinesq approximation or also called the thin-layer approximation [20]. Studies into the dynamics of this approximation has shown that this approximation is valid in when the perturbed density amplitude is relatively small with respect to the background density, $|\Delta n|/N \ll 1$ [20]. As far as this author is aware, there does not seem to exist publications which relaxes the Boussinesq approximation combined with retaining the sheath dissipation and particle loss terms. And so a study combining these could prove useful in determining blob motion and are part of the main focus in the simulations in the following section.

Earlier works into the relaxation of the Boussinesq approximation and neglection of the sheath dissipation and particle loss, predicts and has shown a dependence on the acceleration in the case of $|\Delta n/N| < 1$, where $A/g \sim \Delta n/N$ [27]. And for the larger amplitudes $A \sim g$, thus predicting that the acceleration of the blobs should stay constant above a transition region [27]. In the case of no sheath dissipation and particle loss, a scaling analysis made in ref. [27] shows in the limit of small amplitudes, the radial COM velocity scales as $V_x \sim (\Delta n/N)^{1/2}$ which is the inertial scaling result [11, 19, 20]. When retaining the sheath dissipation and particle loss terms, no scaling analysis appears to have been done. But in the case of small amplitudes, the gradient of the density should be small compared to the other terms. Neglecting the gradient term in the vorticity equation, leads to the linear scaling found in previous works [19]. So in the limit of small perturbed amplitudes, we should see a linear scaling if our logic holds.

Simulation of the blob structures relaxing the Boussinesq approximation, is obtained by utilizing the model equations presented in section 2.1.6. The model is given by

$$\frac{\partial n}{\partial t} + \{\phi, n\} - gn\frac{\partial \phi}{\partial y} + g\frac{\partial n}{\partial y} = D_n \nabla_\perp^2 n - \sigma_n n \exp(-\phi) \tag{4.29}$$

$$\frac{\nabla_\perp n}{n} \cdot \frac{d\Omega}{dt} + \frac{\partial \Omega}{\partial t} + \{\phi, \Omega\} + \frac{g}{n}\frac{\partial n}{\partial y} = D_\Omega \nabla_\perp^2 \Omega + \sigma_\Omega [1 - \exp(-\phi)] \tag{4.30}$$

or expressed in a more compact form

$$\frac{\partial n}{\partial t} + \{\phi, n\} - gn\frac{\partial \phi}{\partial y} + g\frac{\partial n}{\partial y} = D_n \nabla_\perp^2 n - \sigma_n n \exp(-\phi) \tag{4.31}$$

$$\nabla \cdot \left(n\frac{d\Omega}{dt} \right) + g\frac{\partial n}{\partial y} = D_\Omega n \nabla_\perp^2 \Omega + \sigma_\Omega n [1 - \exp(-\phi)] \tag{4.32}$$

We will use parameter values $g = 0.01$, $l = 6$, $D_n = D_\Omega = 10^{-4}$ and the blobs is initialized as a symmetric Gaussian blob with varying initial perturbed amplitude $\Delta n/N$ where the background density $N = 1$. In the simulations where sheath dissipation and particle loss terms are retained, parameter values is $\sigma_n = \sigma_\Omega = 10^{-4}$. Figures and results where particle loss and sheath dissipation is neglected, are specified in the figure description. The data from simulations retaining the Boussinesq approximation and added sheath dissipation and particle loss comes from the simulations made in section 4.3.

4.5.1 Simulation Results

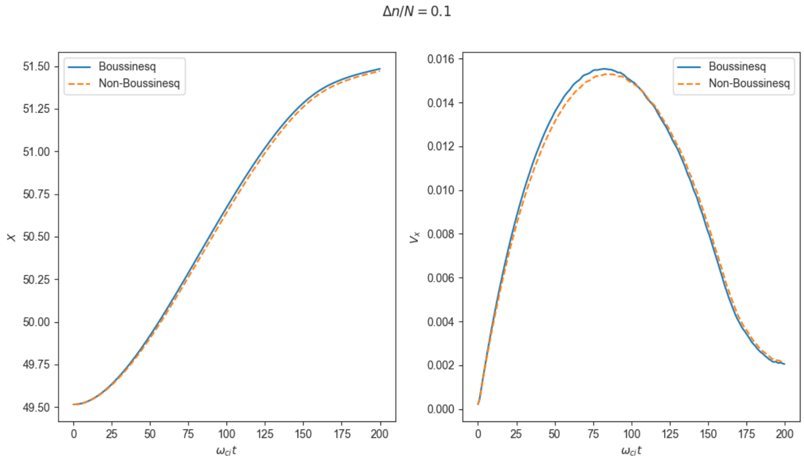

Figure 4.36: Center of mass radial diagnostics comparing blob subjected to Boussinesq approximation and not subjected to Boussinesq approximation for initial amplitude $\Delta n/N = 0.1$. The blue full line corresponds to Boussinesq simulation and orange dotted line corresponds to non-Boussinesq simulation. Position is shown on the right and velocity are shown on the left.

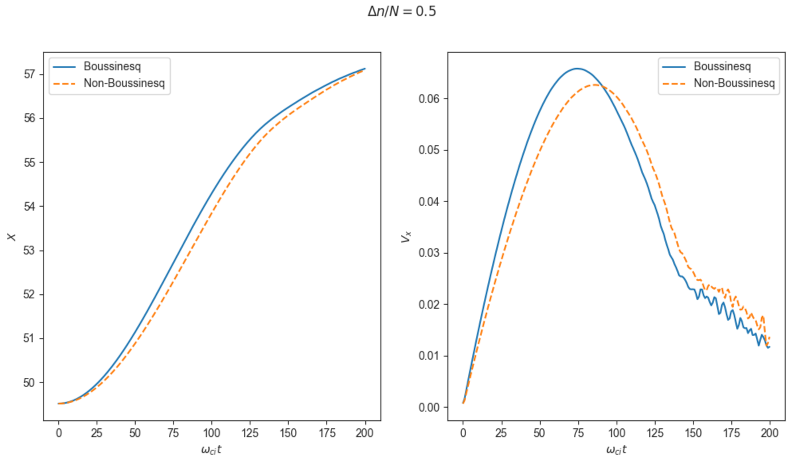

Figure 4.37: Center of mass radial diagnostics comparing blob subjected to Boussinesq approximation and not subjected to Boussinesq approximation for initial amplitude $\Delta n/N = 0.5$. The blue full line corresponds to Boussinesq simulation and orange dotted line corresponds to non-Boussinesq simulation. Position is shown on the right and velocity are shown on the left.

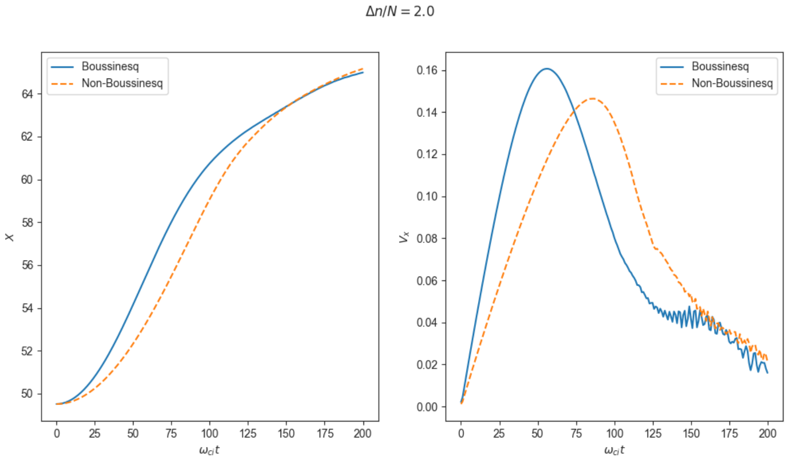

Figure 4.38: Center of mass radial diagnostics comparing blob subjected to Boussinesq approximation and not subjected to Boussinesq approximation for initial amplitude $\Delta n/N = 2$. The blue full line corresponds to Boussinesq simulation and orange dotted line corresponds to non-Boussinesq simulation. Position is shown on the right and velocity are shown on the left.

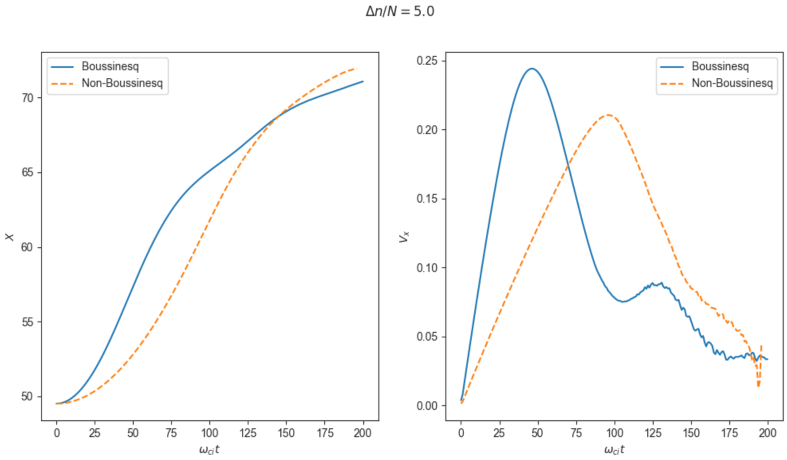

Figure 4.39: Center of mass radial diagnostics comparing blob subjected to Boussinesq approximation and not subjected to Boussinesq approximation for initial amplitude $\Delta n/N = 5$. The blue full line corresponds to Boussinesq simulation and orange dotted line corresponds to non-Boussinesq simulation. Position is shown on the right and velocity are shown on the left.

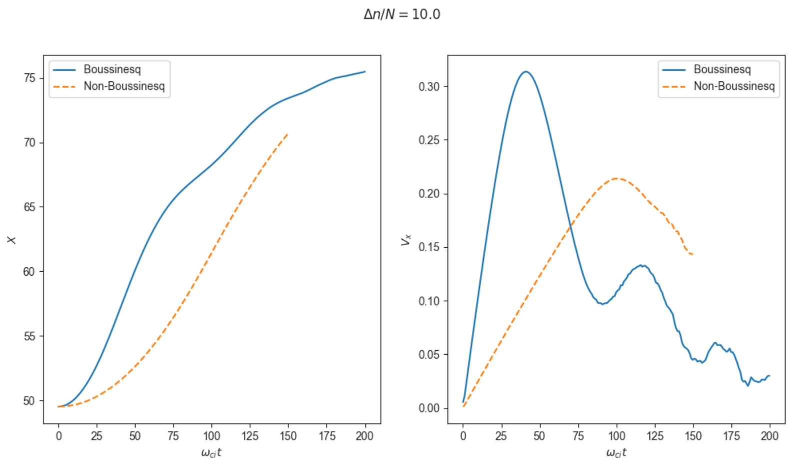

Figure 4.40: Center of mass radial diagnostics comparing blob subjected to Boussinesq approximation and not subjected to Boussinesq approximation for initial amplitude $\Delta n/N = 10$. The blue full line corresponds to Boussinesq simulation and orange dotted line corresponds to non-Boussinesq simulation. Position is shown on the right and velocity are shown on the left.

Figures 4.36 - 4.40 shows the center of mass radial position and velocity for blobs with initial perturbed amplitude $\Delta n/N$ ranging from $0,1$ to 10. The blue line shows the evolution of a blob simulated retaining the Boussinesq approximation, and the orange dotted line shows the evolution of a blob simulated with model equations where the Boussinesq approximation are relaxed. We observe from figure 4.36 showing a perturbed amplitude of $\Delta n/N = 0.1$, that the curves for the position and velocity are very similar. They appear to show the same dynamics with overlapping lines for most of the blobs motion, with only small deviations. Further considering the blobs with perturbed initial amplitude $\Delta n/N = 0.5$, shown in figure 4.37. We don now see a more clear deviation between the two curves as the blobs move radially outwards. The Boussinesq simulation show a blob a slight increase in acceleration and a maximum velocity which is seen to be greater than for the non-Boussinesq case. The shape of the individual curves is observed to be quite similar, however the slope of the velocity curves differ slightly up to maximum radial velocity. From figures 4.38, 4.39 and 4.40, which shows blobs with initial perturbed amplitude $\Delta n/N = 2, 5, 10$ respectively, the difference in acceleration is quite visible. It appears that the acceleration decreases with increasing initial perturbed amplitude, although seen from the two last figures it appears that the maximum radial velocity of the blob structures in these two cases are approximately the same. Figure 4.41 shows the root-mean-square error between the radial COM velocity computed in the case of Boussinesq and non-Boussinesq simulations. Observed from the figure, in the lower initial amplitude region there is a very small rms error between the curves. As the amplitude is increased to unity, we observe a slight error which is $\ll 0.02$. As the amplitude is increased further, the error increases fast and at a initial amplitude of 10 the corresponding rms error is approximately 10%.

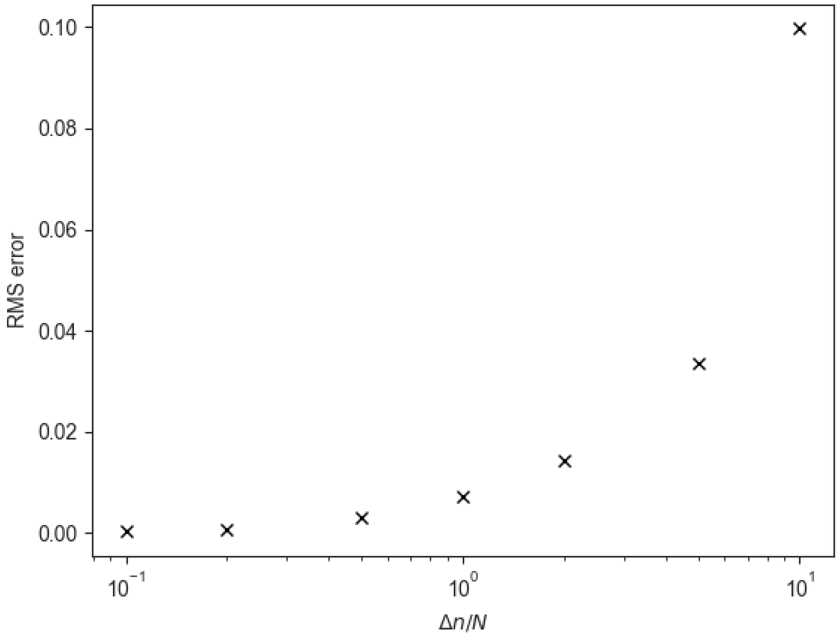

Figure 4.41: The root-mean-squared error computed between the radial COM velocity curves for each initial perturbed amplitude $\Delta n/N$ from 0.1 to 10. Figure are given in logarithmical scale for the initial amplitude and linear scale for the error.

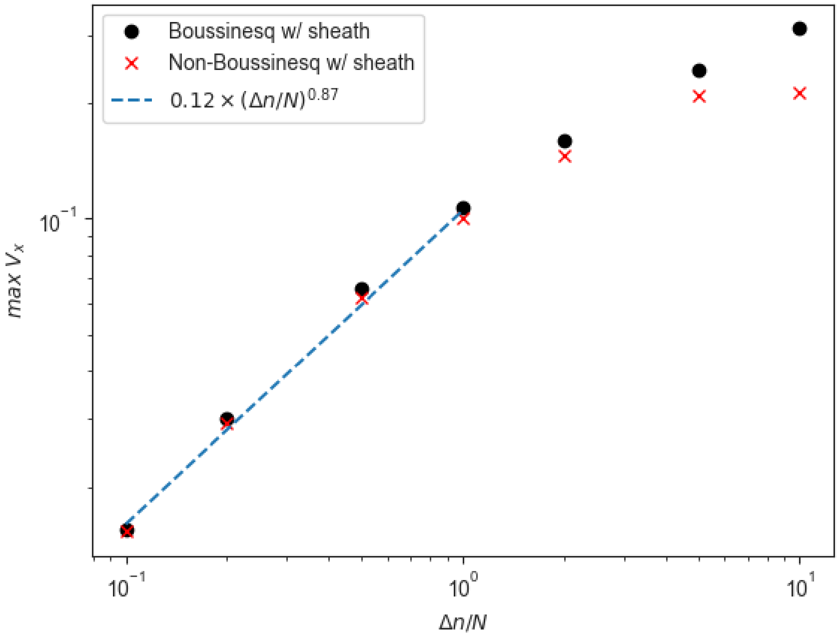

Figure 4.42: Maximum radial COM velocity as a function of initial amplitude for Boussinesq and non-Boussinesq simulations. The black dots shows the Boussinesq approximation and the red crosses shows the non-Boussinesq. The blue dotted line shows a least squares estiamte for a scaling law using non-Boussinesq points.

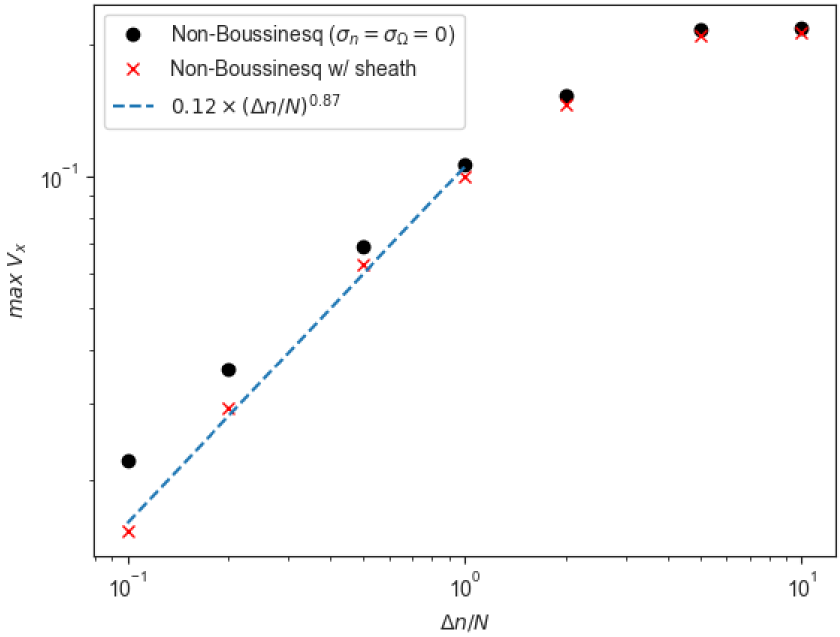

Figure 4.43: Maximum radial COM velocity as a function of initial amplitude for non-Boussinesq simulations with and without the effect of sheath dissipation. Black dots corresponds to simulations where sheath dissipation and particle loss has been neglected, and red crosses corresponds top simulations where sheath dissipation are retained.

Figure 4.42 shows maximum radial COM velocity as a funciton of initial perturubed amplitude in the case of retaining Boussinesq approximation and relaxing the Boussinesq approximation, combined with sheath dissipation and particle loss in both cases. The black dots shows the Boussinesq simulations and the red crosses shows the non-Boussinesq simulations. In the lower amplitudes region when $\Delta n/N < 1$, the maximum velocity appears to be the same with small to no difference in the values. Using a least-squares estimates for $\Delta n/N \lesssim 1$ yields a scaling for the radial velocity in the lower amplitude region by $V_x \sim (\Delta n/N)^{0.87}$. In the region of larger perturbed amplitudes $\Delta n/N > 1$, we start to observe a difference in the estimated values fast. Already at $\Delta n/N = 2$ there seems to be a noticeable difference in the values. For the two points corresponding to $\Delta n/N = 5$ and $\Delta n/N = 10$, we observe that the points are the same and the radial velocity appears to be independent of initial amplitude in the larger amplitude region. Figure 4.43 shows the maximum radial COM velocity for simulations where the Boussinesq approximation are relaxed with and without sheath dissipation terms. In the larger amplitude region, they appear to yield the same maximum velocity which appears to be unchanged by initial amplitude. In the middle and lower amplitude region, they appear to deviate. In the lower region they appear to follow different scaling, the values differ at an increasing rate for decreasing initial amplitudes.

Figures 4.44, 4.45 and 4.46 shows the maximum instantaneous amplitude scales as a function of the radial COM velocity of the blob structures, for initial perturbed amplitudes 0.1, 1, 10 respectively. The blue lines corresponds to simulations retaining the Boussinesq approximation and sheath dissipation, the orange dotted line corresponds to simulations relaxing the Boussinesq approximation while retaining sheath dissipation and particle loss. And the green dotted line corresponds to simulations relaxing the Boussinesq approximation and neglecting the sheath dissipation and particle loss terms. From the figure showing $\Delta n/N = 0.1$, We observe that the lines corresponding to the Boussinesq approximation retaining sheath dissipation and the simulation relaxing the Boussinesq approximation but retaining sheath dissipation, follows exactly the same curve. They appear to remain unchanged, dissipating little density for the lower radial velocities. The simulations retaining the sheath dissipation and particle loss appear to dissipate density at a lower radial velocities compared to the case of the simulation where the sheath dissipation and particle loss are neglected. For $\Delta n/N = 1$, the curves show similar characteristics and appears to dissipate density at a similar rate for all radial velocities. We observe some deviation in the case of non-Boussinesq and Boussinesq with sheath dissipation, and the non-Boussinesq simulated blob without sheath dissipation and particle loss dissipates density at a rate comparable to the Boussinesq simulated blob. The deviation between the simulation using the Boussinesq approximation and the simulated blob relaxing the Boussuinesq approximation are most visible deviated in figure 4.46 which shows the simulations for initial perturbed amplitude $\Delta n/N = 10$. We observe that the non-Boussinesq simulations dissipates density at a higher rate for lower radial COM velocities compared to the case with Boussinesq approximated simulations. For the larger amplitudes, the effect of the sheath dissipation and particle loss is not clearly visible as the curves retaining the sheath dissipation and particle loss terms and neglecting the terms show similar characteristics.

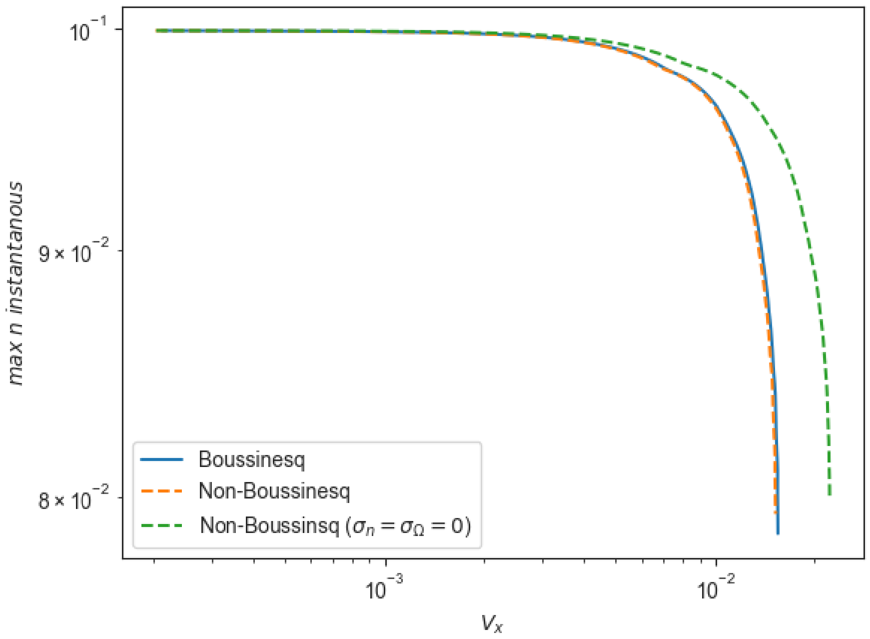

Figure 4.44: Maximum instantaneous amplitude as a function of radial COM velocity, with initial perturbed amplitude $\Delta n/N = 0.1$. Blue line corresponds to Boussinesq approximation, orange and green dotted lines corresponds to non-Boussinesq with and without sheath dissipation terms respectively.

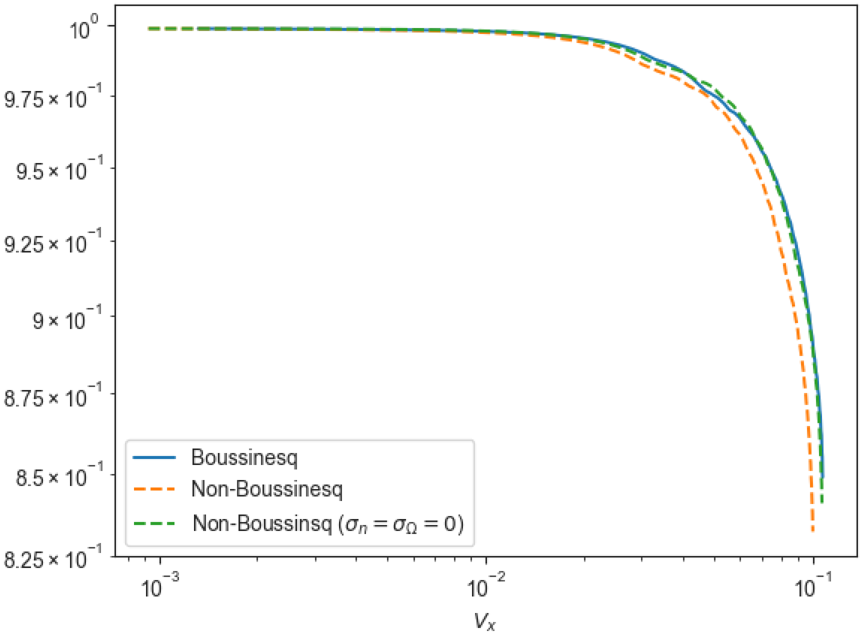

Figure 4.45: Maximum instantaneous amplitude as a function of radial COM velocity, with initial perturbed amplitude $\Delta n/N = 1$. Blue line corresponds to Boussinesq approximation, orange and green dotted lines corresponds to non-Boussinesq with and without sheath dissipation and particle loss terms respectively.

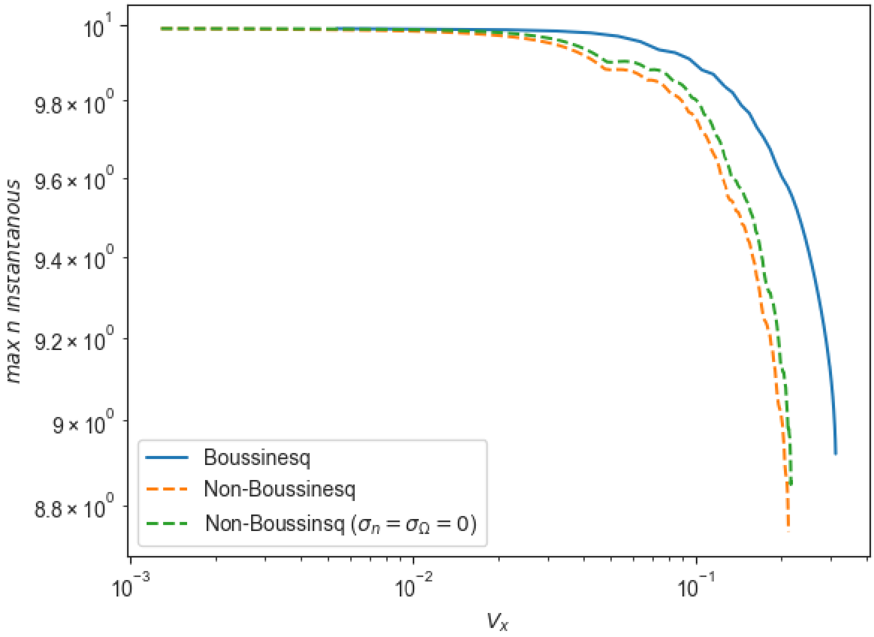

Figure 4.46: Maximum instantaneous amplitude as a function of radial COM velocity, with initial perturbed amplitude $\Delta n/N = 10$. Blue line corresponds to Boussinesq approximation, orange and green dotted lines corresponds to non-Boussinesq with and without sheath dissipation and particle loss terms respectively.

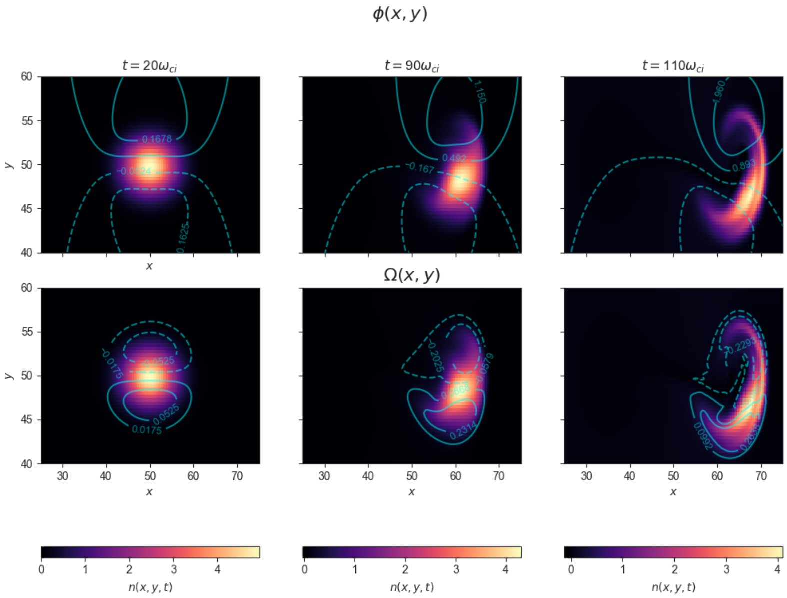

Figure 4.47: Shows the density, potential and vorticity curves for initial perturbed amplitude $\Delta n/N = 5$. Simulation made using non-Boussinesq model neglected sheath dissipation and particle loss, shown for three distinct time steps.

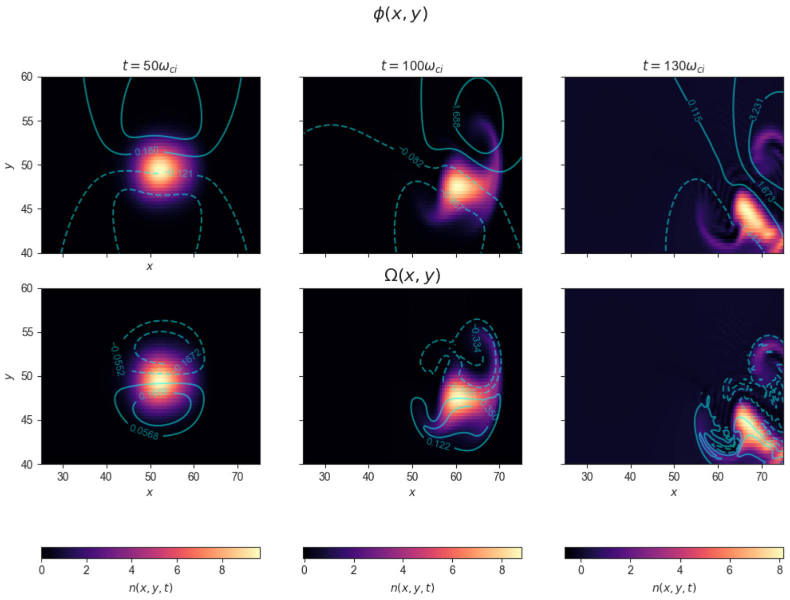

Figure 4.48: Shows the density, potential and vorticity curves for initial perturbed amplitude $\Delta n/N = 10$. Simulation made using non-Boussinesq model neglected sheath dissipation and particle loss, shown for three distinct time steps.

Figure 4.47 shows a blob structure simulated using the model relaxing the Boussinesq approximation and neglecting the particle loss and sheath dissipation for a initial perturbed amplitude $\Delta n/N = 5$. The figure shows the density as colored contour. The potential as blue lines on the top row and the vorticity as blue lines on the lower row. The dotted lines corresponds to negative values and the lines corresponds to positive values. We observe initially the same dynamics as observed for the lower perturbed amplitudes. The blob is initially accelerated due to formation of electrostatic potential and vorticity field, but when the steeping front and trailing wake forms, the blob appears rotated. For the two last time steps, the blob appears to have asymmetric motion in the y-direction and appears to accelerate downwards as the blob moves radially. It appears the introduction of an added inertia term in the form the gradient of the density, greatly impacts the symmetric motion of the blob structures. This dynamic is also visible for the case when $\Delta n/N = 10$, shown in figure 4.48. The blob structures almost appears to rotate due to the effect of the gradient of the density, decelerating the density in the direction of the largest density gradient.

4.5.2 Discussion

From the center of mass radial position and velocity of the blobs simulated using Boussinesq approximation and relaxing the Boussinesq approximation but both retaining sheath dissipation σ_Ω and particle loss σ_n, shows clearly when the approximation is valid. For the lower initial perturbed amplitudes, $|\Delta n/N| \ll 1$, shows that the computed position and velocity curves for the blobs are essentially the same. This is supported by the estimated root-mean-squared error, which is essentially zero for the lower initial amplitudes. As the initial amplitude increases to unity, we observe a increasing difference in the curves and this is accompanied by an increases in root-mean-squared error value for the associated curves. In the amplitude region $\Delta n/N \gtrapprox 1$, the curves deviate quite clearly and we can see that the acceleration of the blobs decreases in the region $1 < \Delta n/N \lesssim 10$. It appears that the acceleration of the blobs is dependent on the initial amplitude, where a increase in perturbed amplitude is followed by a decrease in acceleration. This could indicate a inverse relationship between the quantities and should be considered more carefully. When the initial amplitudes is $\Delta n/N \geq 5$, the shape of the curves is observed to be very different and deviates extremely. This is supported by the large root-mean-squared error, which in the case of $\Delta n/N = 10$ is approximately 10%. The results appear to show a linear relationship with initial amplitude for $\Delta n/N \ll 1$, which is consistent with previous work [27].

Further results from these simulations relaxing the Boussiensq approximation but retaining the sheath dissipation and particle loss terms, show a scaling of the maximum radial COM velocity in the lower perturbed amplitude $\Delta n/N \lesssim 1$ region which is approximately linear with the initial amplitude. The results show a scaling of the form $V_x \sim (\Delta n/N)^{0.87}$ which was essentially the same scaling as found in the simulation retaining Boussinesq approximation combined with the inclusion of the sheath dissipation and particle loss terms. So it appears that in the region of lower amplitude retaining sheath dissipation and particle loss combined with relaxing the Boussinesq approximation, the radial velocity approaches the same scaling with initial amplitude as was obtained in the simulations run with the Buessinesq approximation. This is in agreement with the results obtained in ref. [27], however they neglect the impact of sheath dissipation and particle loss, thus obtaining a square-root dependence of the maximum radial velocity in the lower amplitude region, that is inertial scaling. But they show that in the lower amplitude region, the maximum velocity scaling obtained from simulations relaxing Boussinesq approximation approaches the maximum radial velocity scaling obtained from simulations retaining the Boussinesq approximation. We here obtain sheath dissipation scaling in the limit of lower initial amplitudes due to the added sheath dissipation and particle loss terms. In the larger amplitude perturbations for blobs simulated relaxing Boussinesq approximation combined with retaining sheath dissipation σ_Ω and particle loss σ_n, the results show a detachment in the larger amplitude region. For $\Delta n/N \geq 5$, the maximum radial velocity appears to stay unchanged. This behavior is observed both when sheath dissipation and particle loss is retained and when sheath dissipation and particle loss are neglected, while Boussinesq approximation is relaxed. Thus indicating that maximum radial velocity quickly becomes independent of initial amplitude when Boussineseq approximation is relaxed.

5

Summary and Outlook

The main topic of this thesis are simulations of isolated blob structures in the scrape-off layers of fusion plasma. By considering the center of mass motion of the blobs, we compare the impact of the initial perturbed density amplitude with and without the effect of particle loss and sheath dissipation terms. When the particle loss term and the sheath dissipation terms is neglected, we obtain almost the same maximum radial velocity scaling shown in previous publications of square-root dependence on the initial amplitude in the inertial scaling limit [11, 13, 19, 21]. The difference comes most likely from numerical error. In the higher limit, we show a scaling in the intermediate region between square-root and complete detachment of 0.24. The estimated scaling done by least-squares method after repeated computations, was concluded to have a large uncertainty in the estimated value. For the case when we included particle loss term and the sheath dissipation term, we obtained the almost linear scaling found in previous publications up to a uncertainty in the estimated values [19–21].

We found through the introduction of a simplified model, a set of energy integrals which was shown to reduce to the same results obtained in ref. [27] when neglecting the particle loss and the sheath dissipation terms. These where shown to deviate from the numerical estimates, however the energy integrals neglected the diffusion terms to reduce complexity. They are retained in the simulations and could cause the difference in solutions. When the particle loss term and sheath dissipation are neglected, we show solutions which yield approximately the as predicted from the derived energy invariants.

Stochastic modeling have shown the presence of blob stagnation in the limit of larger values of the particle loss parameter [23]. Using three different initial perturbed amplitudes we show a decreasing maximum radial velocity with increasing particle loss parameter, indicating an eventual stagnation of the blobs in the limit of increasing particle loss parameter. For the lower initial amplitude simulations where we implemented a new model different from the larger amplitude cases, we obtain similar behavior shown for the larger values of the sheath dissipation parameter. The blob appears to retain the initial symmetric shape as it accelerates to a low value, which is retained as it dissipates density at a high rate [19].

One of the main topics of this thesis, is the limitations of the Boussinesq approximation or the thin-layer approximation combined with particle loss and sheath dissipation parameters. Using center of mass diagnostics we show the same apparent behavior found for the acceleration of the blobs in the lower amplitude region when the initial amplitude is $\Delta n/N \ll 1$, where the acceleration appears to scale linearly with initial amplitude [27]. In the intermediate region, when $1 < \Delta n/N \lesssim 10$ the results show an decreasing acceleration with increasing initial amplitude. This could indicate a relationship between the acceleration and the initial amplitude, and should be considered more carefully. In the higher region, the maximum radial velocity is shown to become independent of initial amplitude around $\Delta n/N \approx 5$ showing no difference in maximum value for larger initial amplitudes. In the lower region, we show the transition into a sheath dissipation scaling equal to the one found when Boussinesq approximation is retained. The results in this thesis is as far as this author is aware, the first to show this. The conclusion is that the Boussinesq approximation appears to have little impact on the maximum radial velocity in the region where particle loss and sheath dissipation parameter has an impact on the maximum radial velocity. In the larger amplitude region, the Boussinesq approximation appears to impact the maximum radial velocity and sheath dissipation and particle loss appears to have little impact in this region when they are set to a value of 10^{-4}. In general the Boussinesq approximation is confirmed to be accurate for small initial amplitudes $\Delta n/N \ll 1$.

The impact of the particle loss parameter σ_n should be considered more in terms of a model with linearized particle loss term and neglected sheath dissipation term. Such a model would mitigate the exponential decaying effect on the background density, and would retain most of the complexity of the model which was neglected in the simplified model introduced in section 4.4.1. The behavior from the results in this thesis appears to predict blob stagnation in the limit of larger values of the particle loss parameter. However, the introduction of two different models to study the particle loss term, is less than fortunate. Thus requiring further studies using a rigid model to make conclusion on the dynamics of the system and the predictions of blob stagnation.

A

Numerical Schemes and Diagnotsical Tools

A.1 Finite Difference

The finite difference method is a numerical scheme in which a continuous domain is discretized into a set of grid points. The derivatives are approximated by evaluating the function at these grid points, using expressions which are derived by a truncated Taylor series expansion. For the approximation of a first-order derivative in one variable, the truncated Taylor series expansion gives three approximations; forward difference, backward difference and central difference.

Let the discretized grid be denoted by the set of points $t_0, \ldots, t_n$ where $t_i = t_0 + i\Delta t$ and Δt are the uniform spacing between the points. The *forward difference approximation* of the first order derivative at a point t_i are given by

$$V(t_i) = \frac{dX(t_i)}{dt} \approx \frac{X_{i+1} - X_i}{\Delta t} + \mathcal{O}(\Delta t) \tag{A.1}$$

The approximation utilizes the function value at t_i and t_{i+1} to approximate the derivative and the associated error are of order $\mathcal{O}(\Delta t)$ which indicates that the method has an accuracy of first order.

Similar the *backward difference approximation* of a first order derivative at a point t_i, are given by

$$V(t_i) = \frac{dX(t_i)}{dt} \approx \frac{X_i - X_{i-1}}{\Delta t} + O(\Delta t) \tag{A.2}$$

This approximation utilizes the function values at t_i and t_{i-1} to approximate the derivative, and the associated error are of order $O(\Delta t)$ which indicates that also this method has an accuracy of first order.

Finally the *central difference approximation* of a derivative of first order at a pointt_i are given by

$$V(t_i) = \frac{dX(t_i)}{dt} \approx \frac{X_{t+1} - X_{i-1}}{2\Delta t} + O((\Delta t)^2) \tag{A.3}$$

The central difference method uses values of the function values at t_{t+1} and t_{i-1} to approximate the derivative at point t_i, and the associated error are of order $O((\Delta t)^2)$ which indicates that this method is second order accurate.

A.2 Composite Trapezoid

The *composite trapezoid method* is a numerical integration method, used to approximate a given integral of a function over some domain. For a two-dimensional integral it divide the domain into a grid of sub-rectangles and approximate the integral as a weighted sum of the function values at the respective grid points.

For a function $f(x, y)$, integrated over the two-dimensional domain by

$$I = \int_a^b \int_c^d dxdyf(x, y) \tag{A.4}$$

can be approximated by introducing a grid through dividing the interval $[a, b]$ into m subintervals each of width $h_x = \frac{b-a}{m}$ and the interval $[c, d]$ into n subintervals, each of width $h_y = \frac{d-c}{n}$. The grid points (x_i, y_j) becomes

$$x_i = a + ih_x, \quad y_j = c + jh_y, \quad i = 0, ..., m, j = 0, ..., n \tag{A.5}$$

The integral can be approximated by the weighted sum

$$I \approx \sum_{i=0}^{m} \sum_{j=0}^{n} w_i w_j f(x_i, x_j) h_x h_y \tag{A.6}$$

By using the weights $w = 1$ for interior points in the grid, $w = \frac{1}{2}$ for the edge points and $w = \frac{1}{4}$ for the corner points, the integral over a two-dimensional domain can be approximated by

$$I \approx h_x h_y \left(\sum_{interior} f(x_i, y_j) + \frac{1}{2} \sum_{edges} f(x_i, y_j) + \frac{1}{4} \sum_{corners} f(x_i, y_j) \right) \tag{A.7}$$

Since the domain considered in this thesis are a rectangular domain, this method is quite effective. The error of this method is second order accurate with error of order $O(h_x^2 + h_y^2)$.

Bibliography

[1] D. E. Antonsen. "Blob structures at the boundary of magnetically confined plasmas." Project paper (FYS-3740), Department of Physics and Technology, Faculty of Science and Technology, 06-2024.

[2] A. Y. Aydemir. "Convective transport in the scrape-off layer of tokamaks." In: *PHYSICS OF PLASMAS 12, 062503* (2005).

[3] N. Bian et al. "Blobs and front propagation in the scrape-off layer of magnetic confinement devices." In: *PHYSICS OF PLASMAS, volume 10, number 3* (2003).

[4] D. A. D'Ippolito, J. R. Myra, and S. I. Krasheninnikov. "Cross-field blob transport in tokamak scrape-off-layer plasmas." In: *PHYSICS OF PLASMAS, volume 9, number 1* (2002).

[5] D. A. D'Ippolito, J. R. Myra, and S. J. Zweben. "Convective transport by intermittent blob-filaments: Comparison of theory and experiment." In: *PHYSICS OF PLASMAS 18, 060501* (2011).

[6] D. A. D'Ippolito et al. "Blob Transport in the Tokamak Scrape-off-Layer." In: *COntrib. Plasma Phys. 44, No. 1-3, 205 - 216* (2004).

[7] Gregor Decristoforo. "Numerical simulations and stochastic modeling of intermittent fluctuations in magnetized plasmas." In: *A dissertation for the degree of Philosophiae Doctor, UiT Arctic Unniveristy of Norway* (March 2021).

[8] DIFFER. "PLASMA MATERIAL INTERACTIONS." https://www.differ.nl/research/plasma-material-interactions, accesed: 15.12.2024.

[9] B. D. Dudson et al. "BOUT++: A framework for parallel plasma fluid simulations." In: *Computer Physics Communications, 180(9):1467 - 1480* (2009).

[10] Jeffrey P. Freidberg. *Plasma Physics And Fusion Energy*. Cambridge University Press, 2007.

[11] O. E. Garcia. "Blob Transport in the Plasma Edge: a Review." In: *Plasma and Fusion Research: Review Arcticles, volume 4, 019* (2009).

[12] O. E. Garcia, N. H. Bian, and W. Fundamenski. "Radial interchange motions of plasma filaments." In: *PHYSICS OF PLASMAS 13, 082309* (2006).

[13] O. E. Garcia et al. “Mechanism and scaling for cevection of isolated structures in nonuniformly magnetized plasmas.” In: *PHYSICS OF PLASMAS 12, 090701* (2005).

[14] O. E. Garcia et al. “Turbulence and intermittent transport ath tbe boundary of magnetized plasmas.” In: *PHYSICS OF PLASMAS 23, 122302* (2005).

[15] searching for the perfect shape ITER. “https://www.iter.org/node/20687/searching-perfect-shape.” Acessed: 15.12.2024.

[16] Henrik Jäntti. “Numerical Simulations of Turbulence at the Boundary of Fusion Plasma.” MA thesis. UiT The Arctic University of Norway, 2022.

[17] S. I. Krasheninnikov, D. A. D’Ippolito, and J. R. Myra. “Recent theoretical progress in understanding coherent structures in the edge and SOL turbulence.” In: *J. Plasma Physics 73, 5: 679 - 717* (2008).

[18] R. Kube and O. E. Garcia. “Effect on dynamical friction on interchange motion of plasma filaments.” In: *PHYSICS OF PLASMAS 19, 042305* (2012).

[19] R. Kube and O. E. Garcia. “Velocity scaling for filament motion in scrape-off layer plasmas.” In: *PHYSICS OF PLASMAS 18, 102314* (2011).

[20] R. Kube, O. E. Garcia, and M. Weisenberger. “Amplitude and size scaling for interchange motions of plasma filametns.” In: *PHYSICS OF PLASMAS 23, 122302* (2016).

[21] J. M. Losada, O. Paikina, and O. E. Garcia. “Stochastic modeling of blob-like plasma filaments in the scrape-off layer: Correlated amplitudes and velocities.” In: *PHYSICS OF PLASMAS 31, 042514* (2024).

[22] J. M. Losada, A. Theodorsen, and O. E. Garcia. “Stochastical modeling of blob-like plasma filaments in the scrape-off layer: Theoretical foundation.” In: *PHYSICS OF PLASMAS 30, 042518* (2023).

[23] O. Paikina et al. “Stochastic modeling of blob-like plasma filaments in the scrape-off layer: Time-dependent velocities and pulse stagantion.” In: *In reviw; obtain from https://doi.org/10.48550/arXiv.2412.04966* (2024).

[24] Peter C. Stangeby. *The Plasma Boundary of Magnetic Fusion Devices*. Institute of Physics Publishing, 2000.

[25] C. Theiler et al. “Blob motion and control in simple magnetized plasmas.” In: *PHYSICS OF PLASMAS 18, 055901* (2011).

[26] C. Theiler et al. “Cross-Field Motion of Plasma Blobs in an Opne Magnetic Field Line COnfiguration.” In: *PHYSICAL REVIEW LETTERS 103, 065001* (2009).

[27] M. Wiesenberger et al. “Unified transport scaling laws for plasma blobs and depletions.” In: *PHYSICS OF PLASMAS 24, 064502* (2017).